Investigation of atmospheric-pressure plasma discharges for thin film deposition

by

Frédéric Bless

UNIVERSITY OF LIVERPOOL

Department of Electrical Engineering and Electronics

Thesis submitted in accordance with the requirements of the University of Liverpool for the degree of Doctor of Philosophy

September 2015

Declaration

I hereby declare that this thesis is my own work and no further sources of information have been used other than the references cited. Neither this thesis nor any part of it have been submitted to any other university or institution for the application of another degree or qualification.

Signed: _____(Frédéric Bless)

Date: _____

Abstract

Gas-phase polymerisation of different monomers has been studied for an atmospheric plasma jet predominantly using quadrupole mass spectrometry. Thin film depositions were made and analysed using XPS and TOF-SIMS. Time-resolved and time-averaged measurements were performed to understand more deeply the paths of plasma polymerisation at atmospheric pressure and in ambient air. Continuous wave and pulse DC jets were both investigated. Results show the importance of positive ions in polymerisation and support the step growth formation for the creation of heavy oligomers. Negative ions are also important and depend far more on the signal frequency, more precisely on the off-time duration, than the positive ions. Another study was performed on an adaptable plasma system for atomic layer deposition allowing deposition of oxides at room temperature. Results show a high quality of Al_2O_3 films realised at room temperature with air as an oxygen-rich gas with the use of a custom-built surface discharge plasma reactor.

Publications

Research performed during the period of this study has resulted in a journal publication, a conference proceeding, and two posters:

- **F. Moix**, K. McKay, J.L. Walsh, and J.W. Bradley, "Atmospheric-Pressure Plasma Polymerization of Acrylic Acid: Gas-Phase Ion Chemistry," *Plasma Processes and Polymers*, (published online, 14 July 2015)
- **F. Moix**, K. McKay, J.L. Walsh, and J.W. Bradley, "Tailoring atmospheric pressure polymerization of functional thin films," Oral presentation given at the *SVC 57th Annual Technical Conference,* Chicago, U.S.A., 3rd-8th May 2014
- J.W. Bradley, **F. Moix**, K. McKay, and J.S. Oh, "Plasma polymerisation of thin functional films at atmospheric pressure using capillary jets," Poster presented at the *5th International Conference on Plasma Surface Engineering*, Garmisch, Germany, 15th-19th Sept. 2014
- K. McKay, **F. Moix**, J.S. Oh, and J.W. Bradley, "Routes to tailoring plasma jet polymerization of functional thin films," Poster presented at the *8th International Conference on Reactive Plasmas*, Fukuoka, Japan, 3rd-7th Feb. 2014

Contents

List of Figures

List of Tables

Acknowledgements

I wish to thank, first and foremost, my PhD supervisor, Prof. James W. Bradley for providing me with the opportunity to do a PhD at the Univeristy of Liverpool. I wish also to thank the University of Liverpool, the people in the Department of Electrical Engineering and Electronics, the plasma group (Mike, Steve, TJ, Mohammad, Kirsty, Jun-Seok, Andy, Peter, Ed, James, Mark, Tom, Ni, Zaenab, MJ, Carl) for the good times and the help, Dr J. Walsh for his help in the creation of power supplies, Dr. Ian Brunell for his help using the ALD machine, and Sebastiaan van Nuffel of the University of Nottingham for the XPS and TOF-SIMS measurements. The technicians (Alan, Jill) and everybody who made my stay in Liverpool very enjoyable. I was lucky to be able to know Alan during his last years in Liverpool, his vast experience was always welcome. Big cheers for TJ who became a great friend and corrected my terrible english during my time in Liverpool and even after that. *Un immense merci à ma femme Corinne, pour m'avoir attendu en Suisse pendant ma thèse, pour son support et sa motivation pendant tous les durs moments et pour avoir cru en moi quand je doutais.* Lastly, my thanks goes to the University of Liverpool for funding my PhD.

Chapter 1

Introduction

In the plasma state, molecules of a gas state are excited (by external forces) and are ionised, freeing some of their electrons. A plasma is an ionised gas which is characterised by a collective behaviour [1]. A plasma, contrary to a gas, reacts strongly to electromagnetic forces due to consisting of ions and electrons. Plasma is thus a matter that has the three following properties:

(i) it is an ensemble of unbound charged particles,
(ii) the charge is globally neutral, and
(iii) it exhibits collective behaviour.

The plasma state is the most abundant state in the universe as stars and nebulae are made of plasma, however, on Earth, natural occurring examples of plasma are rare and consist mainly of the flash of a lightning bolt and the aurora borealis. The reason for the rarity of plasma occurring naturally is the low temperature of the planet.

Since the 19th century mankind has been producing and manipulating plasmas in laboratories. Man-made plasmas are being used in research laboratories and industries for several purposes: for fundamental understanding of plasmas [2–9], for energy production in the sector of fusion research [1, 10–12], deposition and etching of thin films mostly in the semiconductor section [13–16], lighting [17–22], and recently in medical applications for sterilisation [23–26]. The reasons of using plasma technologies are functional, economical, and environmental. They tend to replace conventional systems which use hazardous chemicals.

Even when numerous companies use plasmas to deposit thin films with great reliability, full understanding of all the species behaviour is far from being a

reality. Fortunately such an understanding is not necessary to create and operate a plasma system.

Most industrial plasmas operate under vacuum. Low-pressure plasma industrial devices have a wide range of applications and have proved their worth in terms of quality and reliability. However, vacuum technologies are expensive, require complex installations, and regular maintenance. Atmospheric-pressure plasma technology is slowly entering the market and solves some drawbacks of low-pressure plasma systems.

For a long time plasmas were solely studied under vacuum where their stability is higher. Atmospheric-pressure plasmas have a so-called collisional behaviour, due to their high density of molecules and atoms, and, therefore, differ from low-pressure plasmas performed in vacuum vessels. The most common technique to create an atmospheric-pressure plasma discharge in a laboratory is to use a gas which is easy to ionise (for example argon or neon) and to use a dielectric barrier discharge with a high voltage of the order of tens of kilovolts for a gap in the range of centimetres. Atmospheric-pressure plasma dielectric barrier discharges can be designed using various geometries (using cylindrical electrodes, parallel plates, or surface discharge designs).

Although atmospheric-pressure plasmas behave differently from low-pressure ones, their simplicity in terms of installation is a great advantage for industrial purposes. These plasmas are also compatible with roll-to-roll technology and do not require pumping stages.

An example of plasma application is plasma polymerisation which can deposit polymeric films. Low-pressure plasma polymerisation is a common process and atmospheric-pressure devices will start soon to become available in the market [27]. Polymers are large molecules which are composed of two or more similar subunits called monomers. Synthetic polymers such as most plastics have a backbone made of carbon atoms. Polymerisation is the process which links monomers to each other to form polymers.

In this thesis acrylic acid and heptylamine have been studied, these two monomers have been already well analysed in the literature, however, mostly with low-pressure plasma, and therefore results can be compared with previous studies. Acrylic acid is an organic molecule containing a functional carboxylic group. Acrylic acid is mainly used in polymer form as an adhesive. Heptylamine

is used in pharmaceutical drugs for different puproses: anti-infective agents and enzyme inhibitors. It is also used to promote tissue adhesion to a surface [28–30].

Plasma deposition is a common technique used worldwide. However, some thin films require a quality of deposition that plasmas cannot achieve, atomic layer deposition (ALD) on the other hand is a very precise technique used when a very homogeneous and thin deposition is needed. ALD is a deposition technique with the highest surface conformality and deposition thickness control on the market [31]. The ALD technique consists of a high number, typically hundreds, of successive deposition cycles. Each cycle corresponds to a successive injection of gases into the deposition chamber.

The particular benefit of ALD is that the deposition rate is one atomic layer per cycle. To achieve this, the gases (called precursors) are specifically chosen to interact only with the surface of the film. The interaction modifies the chemical composition of the surface and can only be altered by a different gas.

To avoid chemical vapour deposition or gaseous interaction and to restrict the chemical reaction only to the gas-surface interface, an inert purge gas (typically argon) is used before the injection of a different precursor. Hence a cycle of ALD normally results in a homogeneous deposition of one film layer. By changing the gases and the conditions, ALD can deposit a diverse range of films with different compositions.

Plasma-enhanced atomic layer deposition (PEALD), also called plasma-assisted ALD, is an improvement of the conventional ALD technique. The addition of a plasma generator during the use of one of the precursors can ionise that particular gas into a plasma, enhancing greatly its effect on the surface. PEALD can thus decrease the temperature process of certain ALDs and can also allow the use of precursors which are normally not reactive in pure gaseous form.

1.1 Aims

The deposition of thin films plays an important role in today's industrial world: coatings are used in so many of our technological devices. Thin film deposition is nowadays a necessary tool to produce goods in a large range of domains from building engineering to semiconductors and including medicine, and many more.

Most of the depositions are created using high-vacuum technique which are costly and require frequent maintenance. Plasma deposition has gained interest due to its versatility and quality. This thesis is looking at a particular atmospheric-pressure plasma deposition: polymerisation.

The aims of this thesis is to show that through the use of atmospheric-pressure mass spectrometry, a better understanding of polymerisation of monomers using a dielectric barrier discharge at atmospheric pressure can be achieved. It is also aimed to demonstrate that polymerisation of monomers can be made and optimised using atmospheric-pressure mass spectrometry.

Plasma polymerisation has already been studied in the literature, however, for most cases, the analyses were made only on the film deposited. This present research is mainly focused on the plasma behaviour. Polymeric films were also developed to observe the relation between the plasma and the film quality.

Furthermore, this thesis also presents work on a PEALD machine. The description and the use of this simple plasma generator, working under different pressures and having the benefit of being able to be added to existing ALD reactors, are reported. The aim of this PEALD project is the reduction of the process temperatures of a common ALD process by adding a plasma generated during the oxidation phase. The particular benefit of the plasma reactor is that it can work under different pressures from $\sim$1 Torr up to atmospheric pressure. Atmospheric-pressure PEALD is at its early stage[1] and this thesis could pave the way for a fully functioning atmospheric-pressure PEALD system.

On an engineering aspect, another objective of this thesis is in developing state of the art methods using simple and low-cost apparatus whilst achieving high quality deposition. By helping to understand polymerisation processes of an atmospheric-pressure plasma jet, this will aid in the comprehension of atmospheric plasmas and participate in its increase of utilisation in several industrial sectors. Furthermore, by showing that a surface discharge plasma reactor can produce good films by PEALD, this will help in the design of efficient atmospheric-pressure PEALD systems.

[1]The first article of a functioning system dates from 2011 [32].

1.2 Motivation and Outline

The motivations for this thesis are a mix of a pure physics understanding of plasma and polymerisation in general and a hope to show that simple designs can be highly efficient for a domain as complex as atmospheric polymerisation and atomic layer deposition of oxide films. The University of Liverpool laboratories have the perfect equipment and the people there have the knowledge to perform state of the art experiments. Throughout the period of the research, help was provided, especially when the plans and thesis project were modified. However, the motivation of using the simplest device for both the polymerisation and the ALD parts of this research remained throughout the duration of the time spent in Liverpool.

Outline

The next chapter goes into more detail to develop the subjects addressed and the techniques used in this thesis. The experiment setup chapter describes precisely all the apparatus used to collect the data. The following chapter, named methods and description of analysis techniques, describes and justifies the data gathering method used. It also outlines the way data were analysed. Chapter 5, on spectrometry of the plasma polymerisation is the heart of this thesis, presenting the original results performed in this thesis on plasma polymerisation using atmospheric plasma jets. The work presented in the first section of chapter 5 has generated to date the following publication:

- **F. Moix**, K. McKay, J.L. Walsh, and J.B. Bradley, "Atmospheric-Pressure Plasma Polymerization of Acrylic Acid: Gas-Phase Ion Chemistry," *Plasma Processes and Polymers*, (published online 14 July 2015)

Chapter 6, analysis of deposited thin films, shows the surface measurements made on thin polymeric films. Chapter 7 presents the results of the thin films made on an atomic layer deposition device modified with a surface plasma reactor. Finally the conclusions chapter summarises the original results found in this thesis, discussing their implications in the relevant fields, and potential future work is suggested.

Chapter 2

Literature Review

Atmospheric-pressure polymerisation depositing acrylic acid and other polymers as well as plasma-enhanced atomic layer deposition have been reported in recent years. A summary of articles are presented in this section. However, before going into details of these precise subjects, a review on plasma discharges, atomic layer deposition, as well as on analysis techniques, are presented to better understand the contributions of this thesis.

2.1 Plasma

Plasmas consist of ionised gases, they are a collection of freely moving charged particles. Averaged over all the particles, plasmas are electrically neutral; positive and negative particle densities formed of ions and electrons, respectively, are equal and cancel each other out. Plasmas can also contain a high density of neutral species, the degree of ionisation of a plasma is the density of ions over the density of ions and neutrals ($n_\mathrm{i}/(n_\mathrm{i}+n_\mathrm{n})$). Although the properties of a plasma are mainly governed by the charged particles, the neutrals play an important role in ionisation and diffusion processes in discharges [34]. One way to categorise plasmas is to separate them by their operating pressure, thus plasmas are called low-pressure plasmas when operated under vacuum and atmospheric-pressure plasmas when operated at atmospheric pressure. Another way of categorising plasmas is to compare their temperatures. Hot plasmas are characterised by really high ion and electron temperatures, up to 20 000 K, and are close to a degree of ionisation of 100 %. Hot plasmas are also called near equilibrium plasmas due to the

species having similar temperatures. Cold plasmas have ion temperatures which are from ∼1 000 K down to room temperature, cold plasmas are also referred to as non-equilibrium or non-thermal plasmas. The ionised molecules and electrons have significantly different temperatures, this is due to the energy loss of the ions through collisions [35]. It can be noted that in plasma physics the temperature is often given in electron volts using the following equation for converting units:

$$T(\mathrm{eV}) = \frac{kT(\mathrm{K})}{e} \tag{2.1}$$

where k is the Boltzmann constant = 1.38×10^{-23} J/K. Thus when speaking about temperature 1 eV is equivalent to ∼11 600 K.

The particles in the plasma are subject to different phenomenons: ionisation for the neutrals, recombination for the charged particles, elastic collision, and excitation [7]. A plasma is in a steady state when both processes have the same rate, i.e. the same number of charged species are created as neutralised. Ionisation also need to account for surface losses. The ionisation process is either due to the impact of neutral atoms with electrons, penning process, or with photons like shown in the four reactions below,

i) $e^- + A \rightarrow A^+ + 2e^-$,

ii) $\gamma + A \rightarrow A^+ + e^-$,

iii) $e^- + A \rightarrow A^-$,

iv) $e^- + AB \rightarrow A^- + B$,

where A and B are atoms, e^- are electrons, and γ are photons. The possible recombination reactions of positively and negatively charged species in a plasma are listed as follows:

v) $e^- + A^+ \rightarrow A + \gamma$,

vi) $e^- + A^- \rightarrow A + 2e^-$,

vii) $A^- + B^+ \rightarrow AB$,

viii) $e^- + AB^+ \rightarrow A + B$,

ix) $e^- + AB^- \rightarrow A + B + 2e^-$,

x) $2e^- + A^+ \rightarrow A + e^-$.

A common definition of a plasma is "a quasi-neutral gas of charged and neutral particles which exhibits collective behaviour" [1]. Although plasmas are globally neutral, the charged particles react to electromagnetic fields, showing a collective response. The charged particles are screening each other out at a small scale. Thus, local charge perturbations are confined to a small volume. These interactions between particles, leading to screening of charges, happen in a sphere of radius λ_D, where λ_D is called the Debye length. Derivation of the Debye length is presented in appendix A.1.

The plasma sheath

The Debye screening is a reaction of the plasma, mainly the slow electrons, to counter any electric potential. When a plasma is in contact with a surface, a screening will happen near this new electric potential area. The electrons situated close to the surface will quickly move towards it, leaving a region with lower electron density [36]. This positively charged thin region between the plasma bulk and the surface, called a plasma sheath, is illustrated in figure 2.1. The difference of density between electrons and ions in the region near the surface creates an electric field. This electric field accelerates the positives ions towards the surface and the electrons away from it [37].

Pressure

The pressure affects the structure of the plasma but not the mechanisms of ionisation and recombination. For example, in order to generate a stable discharge between two flat electrodes at high pressure (as the one represented in figure 2.3), the distance between the electrodes must be reduced [34]. Changing the distance between the electrodes to maintain a stable plasma under different pressures has been known about since the work of Friedrich Paschen around 1890 [38]. The curve of the voltage fed to the electrode to create a stable plasma as a function of the pressure multiplied by the inter-electrodes spacing (pd) is called a Paschen curve. Paschen curves of different gas compositions are shown in figure 2.2.

Figure 2.3a presents the different regions of a noble gas plasma in a vacuum tube with a cathode and an anode at each end of the cylinder. The different

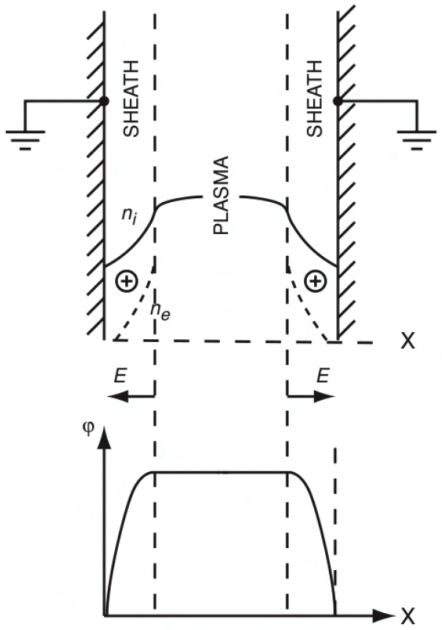

Figure 2.1: The top figure illustrates the charge density distribution, with a plasma present between two surfaces at zero potential. In the plasma region the density of ions and and electrons are about equal. The bottom figure illustrates the resulting potential distribution and the direction of the electric field. Where n_{i} = ion density, n_{e} = electron density, and $\oplus$ indicates the positively charged sheath region. Illustration taken from [7].

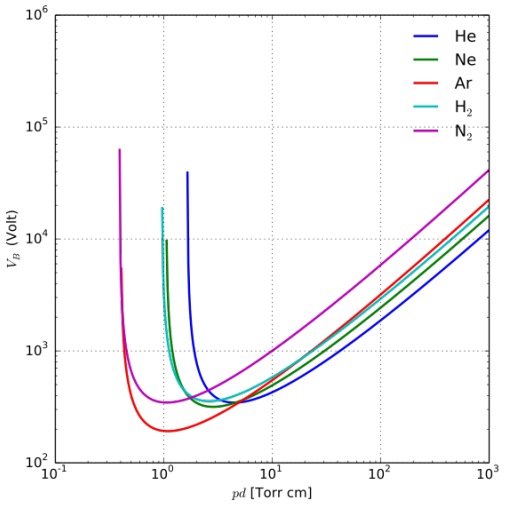

Figure 2.2: Paschen curves for different gas compositions. Taken from [34].

physical parameters are shown in figure 2.3b-g, and explains the effect seen in figure 2.3a.

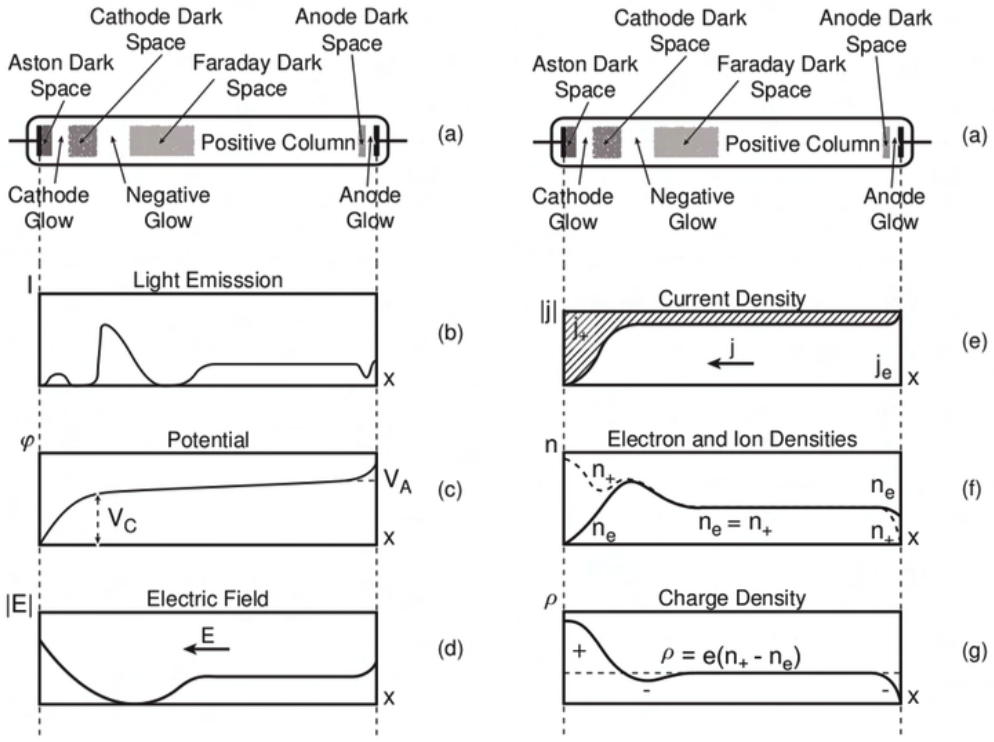

Figure 2.3: Schematic of different physical parameters of regions in a plasma. Taken from [39].

2.2 Dielectric Barrier Discharge

A dielectric barrier discharge (DBD) is a plasma discharge created between two metallic electrodes separated by a dielectric. There are many possible configurations of the arrangement of the electrodes. In the nomenclature, two basic types of DBD are categorised: the volume discharge (VD) and the surface discharge (SD), which can also be subdivided into other DBDs [40]. As far as VDs are concerned, the discharge appears in the gap between the two conductor plates (or cylinders) filled with gas, with one or both of the plates covered by a dielectric [41].

Figure 2.4 shows the different kinds of VD arrangements: (figure 2.4a) the symmetric one, where both electrodes are covered by a dielectric, and (figure 2.4b-c) the asymmetric one, where the dielectric layer is either on one of the electrodes or between them. The SD occurs, as its name indicates, on a surface of a dielectric layer whose sides are covered by electrode strips or plates, depending on the arrangement. Four different SDs can be defined. Schemes of the configurations

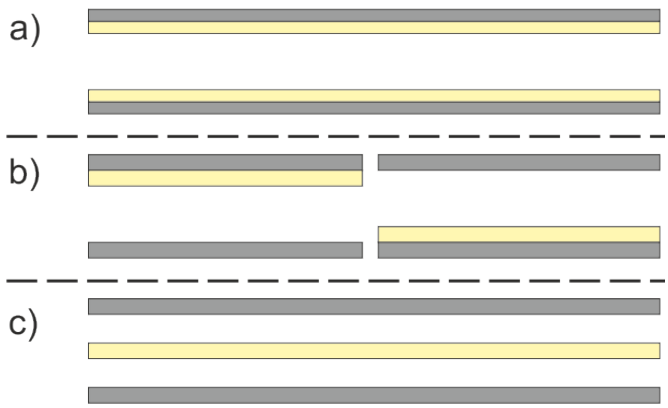

Figure 2.4: Three different volume dielectric barrier discharge designs: a) symmetric, and b) and c) asymmetric. Insulating material is represented in yellow, and electrodes in grey.

which create the four different discharges are shown in figure 2.5a for the classical surface discharge arrangement, figure 2.5b for the actuator, figure 2.5c for the insulated surface discharge arrangement (ISD), and figure 2.5d for the coplanar discharge arrangement (CD) [42, 43].

The classic SD arrangement is simply two electrodes strips on each side of a thin dielectric layer. The actuator is similar to the classic arrangement but the lower electrode (often grounded) is a larger strip or a plate. The ISD arrangement is simply a classic SD arrangement where the top has been covered by a thin isolating film. In the CD arrangement, the electrodes are embedded into the dielectric, close to the surface.

A DBD is a non-equilibrium plasma discharge formed from highly energetic electrons suitable for generating radicals at various ranges of pressures [40, 44]. In a DBD, discharge channels are created along the direction of the electric field. The direction of these channels is the main difference between VDs and SDs. The discharge channels in VDs occur perpendicularly to the electrode plates and the ones in SDs are created along and on/above the dielectric between each pair of electrodes [45]. This difference can be crucial when the DBD is used to treat fragile components, in a VD the electrons are crossing the substrate, which can effectively cause local overheating or even lead to surface damage. Furthermore, in SDs the gap between the channels and the treated material can be varied [46–48].

According to Tefecka *et al.*, the applications of the symmetric VD, the CD, and the ISD are advantageous because no metal conductors are in direct contact

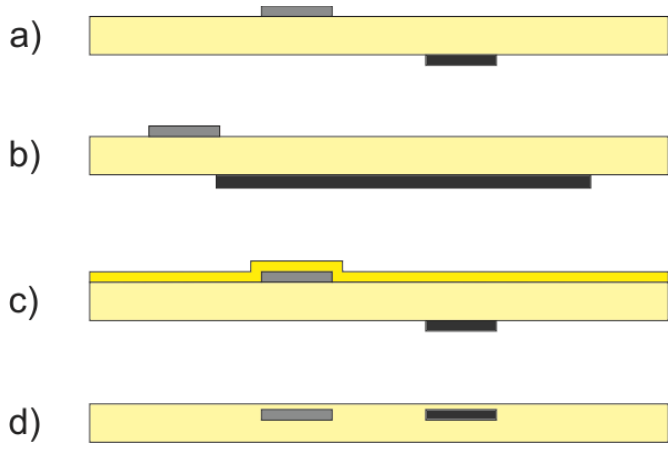

Figure 2.5: Four different surface dielectric barrier discharge designs: a) classic SD, b) actuator, c) ISD, and d) CD. Insulating material is represented in yellow, driven electrodes in light grey, and grounded electrodes in dark grey.

with the discharge and so the lifetime of metastable excited radicals should be longer, which should lead to a more homogeneous and denser plasma at atmospheric pressure [47]. Due to its symmetric geometry, CD arrangement is exposed to easy ignition of an unwanted discharge at the backside of the configuration. The actuator does not have this problem because the grounded electrode on the backside of the discharge system is screening the electric field of the driven electrode [42].

According to Korzec *et al.*, the first industrial application of a DBD is the synthesis of ozone [5]. Due to the growing demand of this gas involved in the decontamination of water, this process is still in development [49]. The field of applications of this technique is large, for example, treatment of surfaces [50], flat plasma displays [21], pollution control [51], elimination of hazardous compounds [52], film deposition [53, 54] and the synthesis of organic compounds [40, 41, 47, 55]. The applications of DBD are effectively wide and varied, and one of the main advantages of this non-thermal plasma source is that they can operate at high pressures (typically atmospheric pressure) and at low gas temperatures. Moreover, in many cases, when the configuration and all the parameters have been optimised in small research lab devices, the change of scale to larger dimensions does not normally raise a problem [55].

Some applications require a particular DBD arrangement. As written above, the VD can cause damage to fragile substrates and thus the SD is needed for

the treatment of certain materials. CDs have been extensively studied and used to generate ozone with a high efficiency by Murata *et al.* [56]. Although CDs are also suitable to modify woven and non-woven textiles [47] and have been used to generate thin layers of TiO_2 [57], the principal application for CDs is in plasma display panel (PDP) cells, which are used for large area flat panel displays also called plasma screens. A PDP cell consists of a small CD arrangement where the discharge is confined to a volume typically of 0.1 mm^3 approximately at atmospheric pressure; the ultraviolet light emitted by the glow discharge of the excited species (normally noble gases) is converted into visible light (red, green, or blue) using phosphor [17, 22]. Research is ongoing to improve the efficiency of this configuration to be able to stay competitive with LCD, LED, and OLED technologies [17–19, 22], it is worth noting that a lot of LCD screens use plasma as backlighting.

Another DBD configuration running at atmospheric pressure highly studied nowadays is the actuator. It is expected to control aerodynamic flow over airfoils and backward facing steps with advantages over conventional flow devices, the main one being the absence of moving parts [43, 58]. The possibility of using a plasma source at atmospheric pressure is a great advantage from an industrial point of view, unfortunately the main problem of processing that occurs at the high-pressure process is the inhomogeneity of the plasma due to the formation of filamentary microdischarges [59].

2.2.1 Atmospheric-Pressure Discharge

The materials used for the dielectric barriers are mainly glass, quartz, and ceramic but plastic foils, teflon, and other insulating materials can be used too [60]. DBDs are driven by either a pulsed DC voltage or an AC voltage with a typical frequency between 0.01-10 kHz and a typical voltage between 0.1-10 kV depending on the parameters (gas, pressure, configuration, etc.) [61]. When the voltage is high enough an electrical breakdown occurs between the electrodes.

At atmospheric pressure, DBDs usually appear in the form of a so-called filamentary plasma which consists of many short-lived filamentary microdischarges (MDs) separated by a distance similar to the inter-electrode gap [21]. The MDs are created simultaneously and develop spatially independent of their neighbours. Generally, the new MDs develop in the same place due to the charges deposited on

the dielectric by the preceding MDs, this maintains the non-uniformity through time. Due to MDs always developing at the same place between the electrodes, filaments of plasma can be observed. These thin filamentary discharges are also called microchannels.

This non-uniformity, being a problem for industrial purposes, has increased the research to produce an atmospheric-pressure glow discharge (APGD) [41]. The difficulty of studying the dynamics of these MDs is the need to investigate experimentally at a sub-ns and sub-mm resolution [55]. Although the knowledge of this filamentary aspect was scarce for a long time, considerable progress has been made using cross-correlation spectroscopy [62].

Despite DBDs being generally non-uniform, as non-thermal plasmas, the energy of their electrons can be transmitted to heavy particles effectively, which leads to the creation of many radicals and metastable species [40].

Each parameter (gas, pressure, voltage, dielectric material, temperature) and configuration of DBD leads to a different behaviour of discharge. It is the reason why every new specific DBD device needs to be built and characterised before being sure of the intended application [45].

Korzec *et al.* showed that time-resolved measurements of discharge electrode current and voltage is an efficient method of characterising a DBD [46] . These measurements provide the lifetime of metastable radicals and evaluate the efficiency of the discharge. Diode laser atomic absorption spectroscopy (DLAAS) has been used by the same team in another paper to measure the concentration of metastable excited species of a helium plasma [5]. Knowing this concentration is, according to some researchers, a key to understanding how to operate and sustain a homogeneous APGD in DBD [63].

2.2.2 Plasma Jet

DBDs can be created using a wide variety of arrangements. At atmospheric pressure, cylindrical electrodes arrangements and variable gas flows are used in laboratories and industries. They are called plasma torches, plasma sprays, or plasma jets depending on their power, size, and utilisation.

Non-thermal atmospheric-pressure jets are recently gaining in interest in the academic and industrial sector. It is a promising technology that is simple to set-up, easy and economical to operate, and does not require vacuum equipments [64].

Plasma jets using a DBD configuration stand out as a particular technological achievement. Atmospheric-pressure DBD jets produce a stable yet highly reactive plasma plume, which extends beyond the confines of the device. This makes them suited to applications demanding the remote processing of non-uniform, thermally liable substrates [65].

According to Kong *et al.*, atmospheric-pressure plasma jets (APPJs) offer good plasma stability in the upstream electrode region while allowing a rich variety of chemical reactions to take place mostly in the downstream electrode region [66]. The spatial separation of the generation region from the application region seems to provide a wider range of chemical reactions than atmospheric-pressure plasmas created between parallel-plate electrodes.

A typical APPJ involves a plasma produced inside a small tube (inside diameter of mm range) and being ejected into the surrounding atmosphere. The plasma outside the tube is called the plasma plume and is the active region of the plasma which is brought into contact with samples. APPJs are used for several applications: etching [67], surface modification [68], adhesion enhancement [69], chemical and biological decontamination [70], biomedical applications [71], diverse medical therapies [72], and antimicrobial [73]. Different gases can be used to generate the plasma, the most commonly used are helium, argon, nitrogen, air, and a mixture thereof.

In [74], Shao *et al.* have analysed two similar jets using different gases: helium and argon. They showed that the discharges are created by different mechanisms: via the corona effect for helium discharges, whereas argon discharges are ignited with the help of a DBD process between the electrodes. It can be noted that by keeping all the other parameters constant and changing only the gas, the effects are significant on the APPJs. Shao *et al.*'s study shows that the change in gas considerably modifies the behaviour of the plasma. The discovery from this recent paper (2012) shows that all the mechanisms of atmospheric plasma jets are still not entirely understood.

A large variety of APPJ configurations are possible, figure 2.6 shows some examples of electrode setups (the setup used in this thesis is represented by figure 2.6b). One major difference amongst the designs is the direction of the electrical field igniting the discharge, it can be parallel to the gas flow (linear-field jet) or perpendicular to it (cross-field jet).

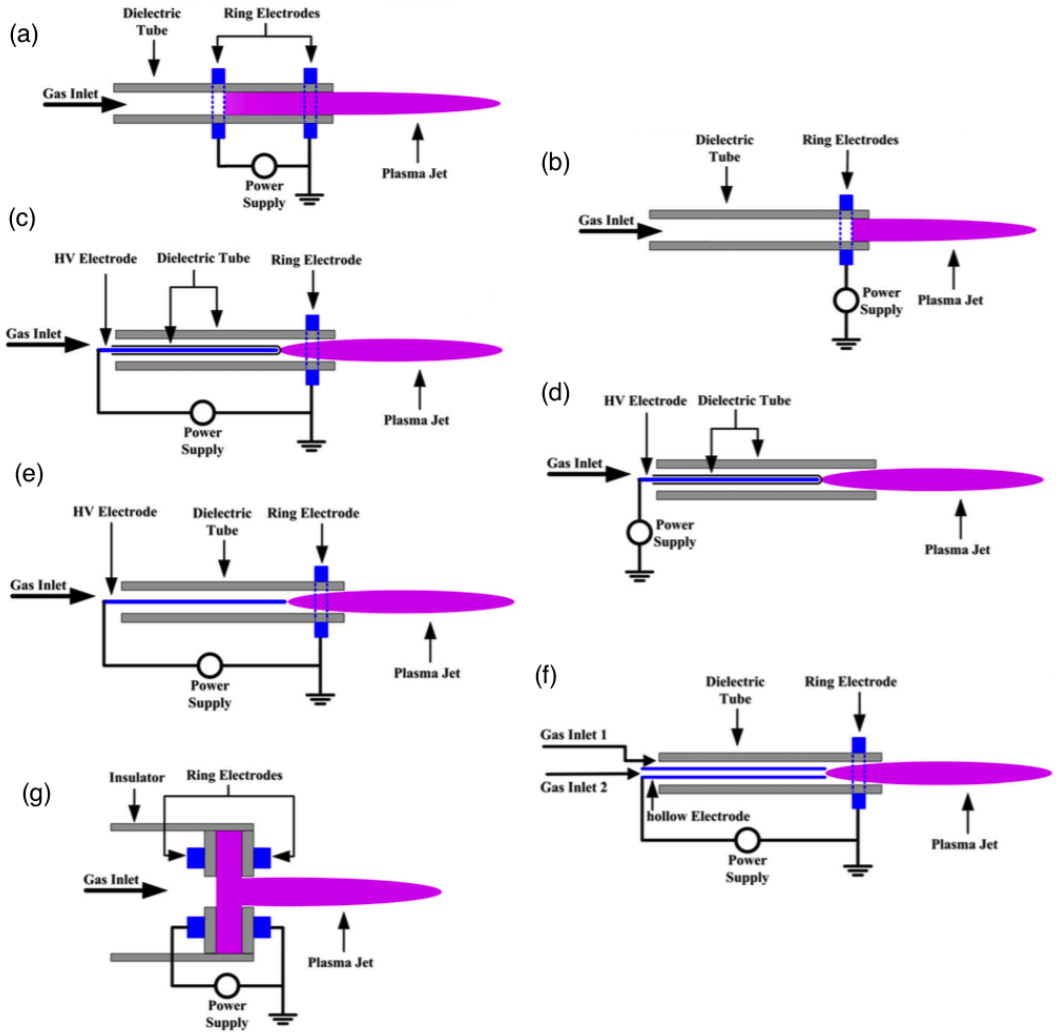

Figure 2.6: Possible configurations of atmospheric-pressure plasma jets. Taken from [75].

Walsh *et al.* described the difference of the cross-field and linear-field jets [76]. They found that the plume is longer in linear-field jets and that the plasmas from cross-field jets contain species having lower temperatures. Related to this temperature difference, Walsh *et al.*, using optical emission spectroscopy, observed that plasma plumes from linear-field jets react more with ambient surrounding molecules than plumes from cross-field jets.

Walsh *et al.* observed and detailed three states of atmospheric-pressure plasma jets [77]. For a linear-field jet, operating with a sinusoidal input signal at a fixed frequency, an increase in the driving voltage has been observed to modify the

plasma behaviour, three types of responses have been found: the chaotic mode, the bullet mode, and the continuous mode. When the voltage is further increased, arcing appears.

In the bullet mode, APPJs were investigated using nanosecond time-scale photography using an intensified charge-coupled device (ICCD) camera. Fast moving clusters of high density plasma, which are known as plasma bullets were observed. Two bullets are created during each period, one when the driven voltage is positive and the other when it is negative. Different explanations of the plasma bullets creation and displacement have been proposed. The Dawson's theory proposes that the ionised front of the bullet propagates due to the photo-ionisation process as shown in figure 2.7. Walsh *et al.* have been able to provide support for Dawson's photo-ionisation theory in [77]. In the article, four single-shots with two nanoseconds exposure time of a bullet were taken successively. The bullet seems to blink, showing alternatively bright and dark light intensity. That corroborates Dawson's photo-ionisation theory. In figure 2.7, a cycle of period when photons are emitted (figure 2.7a-b) followed by a period of ionisation neutralisation without any light emission (figure 2.7c-d) is schematically represented.

The chaotic mode is a regime where the voltage is not high enough to produce stable discharges at every period, resulting in a weak unstable plasma jet. The chaotic mode is therefore not often investigated due to its lack of stability and its weak creation of active species.

In the continuous mode, no bullets are observed in small time-scale photography, and no spatial inhomogeneity in the plasma density is observed between the two electrodes. Walsh *et al.* noted, however, that plasma bullets may still be present as a plasma wave but are hidden by the plasma emission in the continuous mode [77].

Measuring the current of the driven electrode can also give an indication of the mode behaviour of an APPJ as shown in figure 2.8. The currents of bullets in a linear-field APPJ of helium were measured and analysed using a voltage monitor. Oh *et al.* have calculated that bullets contain net charges of 10^{-9} C and charge densities between 10^{10} and 10^{11} cm^{-3} [78]. Xiong *et al.* recorded an electron density of 10^{15} cm^{-3} in the center of the bullet and 10^{14} cm^{-3} at the edge region [79]. It has been observed that the negative bullet charge density, created

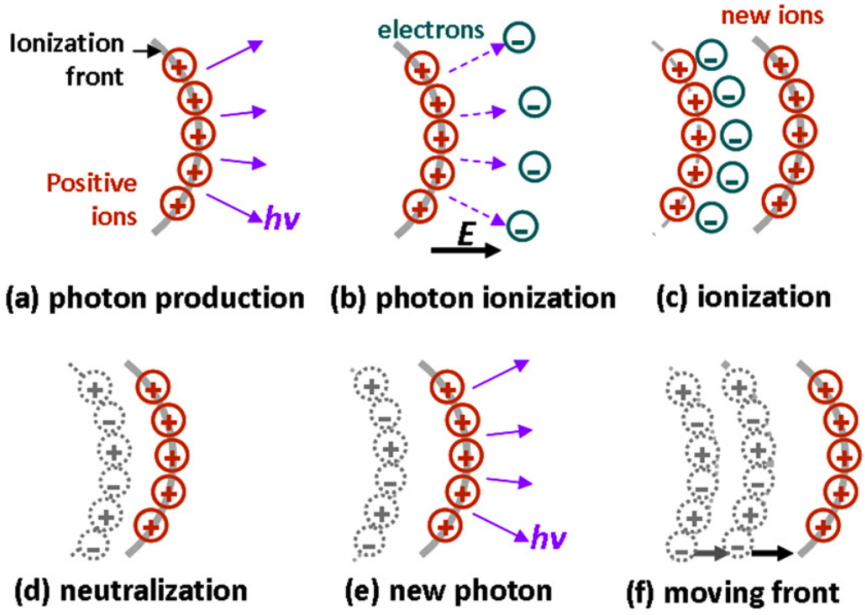

Figure 2.7: Dawson's photon-ionisation theory illustrated, assuming complete neutralisation of positive ions by photoelectrons. The instantaneous cathode is on the right. It starts with (a) a positively charged plasma head emitting photons; (b) new electrons produced by photon ionisation set up a strong electric field; (c) photoelectrons moving to the original plasma head and leaving behind new positive ions to form the new plasma head; (d) ions are completely neutralised; (e) the new plasma head emits photons; (f) this creates a newer plasma head forming a moving plasma head. Image and captions taken from [77].

when the voltage is negative, is generally lower than the positive bullet charge density. The true discharge current is a composition of the displacement current and the bullet current [80]:

$$I_{\text{dis}} = I_{\text{bullet}} + I_{\text{disp}} \tag{2.2}$$

where I_{dis} is the discharge current, I_{bullet} the bullet current, and I_{disp} is displacement current which is an electromagnetic response to any current (more explanation is section 4.1.1). The bullet speed has been measured using an ICCD camera and is in the range 10^4 and $10^6\,\text{ms}^{-1}$ [77, 78, 80, 81].

Frequency plays an important role in APPJs, point-like plasma bullets, having a circular shape have been observed for signals below 50 kHz [82]. Plasma bullets become more and more strip-like as the frequency increases until it reaches continuous mode [77, 82].

Radio-frequency, typically 13.56 MHz, is another frequency commonly used

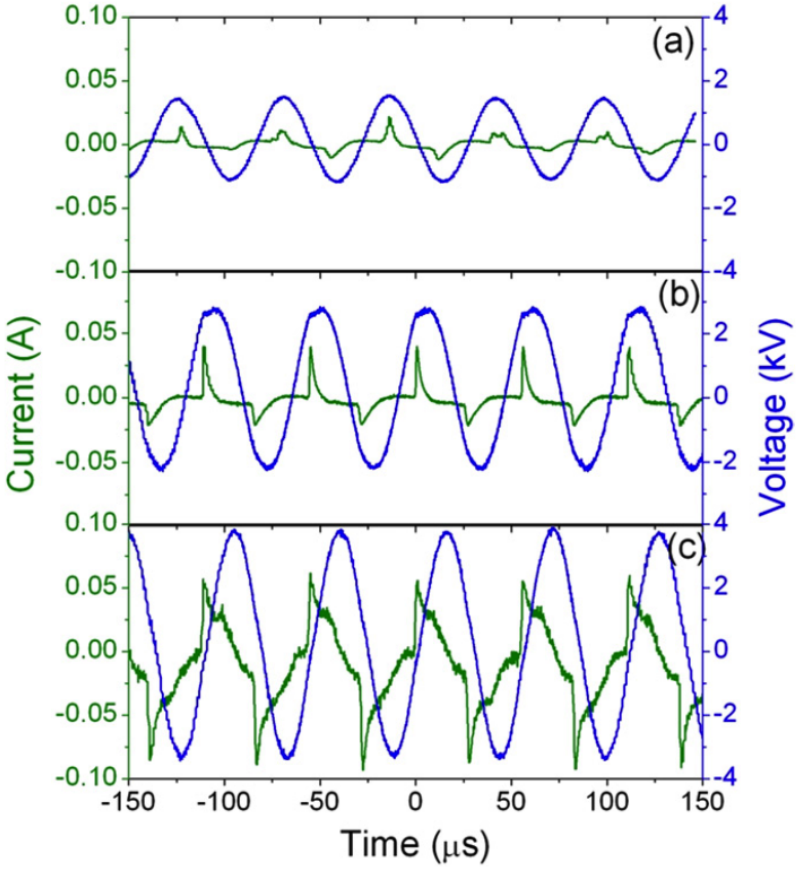

Figure 2.8: Current and voltage of a linear-field atmospheric-pressure plasma jet. In (a) the chaotic mode can be seen, in (b) the bullet mode, and in (c) the continuous mode. Taken from [77].

for driving APPJ [83, 84]. RF plasma jet signals can be pulse-modulated, having an on-time with RF power and an off-time without signal. Changing the duty cycle modifies the reactive species of the plasma plume, which also modifies the gas temperature [85].

Maletić *et al.* have measured the different behaviours of the plasma propagation of the plasmas in APPJs with different tube lengths [86]. Similar electrodes have been created with the same distance between them on four glass tubes with different lengths. An ICCD camera was used to visually measure the difference between the plasmas. It has been observed that by varying the tuble length, the distance travelled by the plasma bullets can be increased.

2.3 Surface Engineering of Polymeric Material

Plasma devices are used for many applications. One of them is the deposition of polymeric film through plasma polymerisation using low or high-pressure plasmas. This section describes the plasma polymerisation, the different growth mechanisms, and provides information on the two monomers used in this thesis: acrylic acid and heptylamine.

2.3.1 Polymerisation

Plasma polymerisation is a technique using plasmas to induce or create polymers in gas, liquid, or solid phase. The first models of plasma polymerisation and its use in food packaging industries begin in the '60s [87–90]. Yasuda describes in [91] that there are two different ways that plasmas can produce polymerisation: plasma-state and plasma-induced polymerisation. The former is the creation of polymers directly in the plasma, whereas the latter is the production of polymers at the interface of the plasma and the surface of the deposited substrate. Although it is recognised that plasma-state polymerisation is the main route of polymerisation [92], both phenomenons appear in most plasma deposition [93].

Figure 2.9 illustrates the competition between ablation due to plasma etching and polymerisation coming from either plasma-state polymerisation, polymer deposition, or plasma-induced polymerisation.

Plasma polymerisation has been defined by Andy Brooks *et al.* as "the formation of polymeric materials under the influence of plasma conditions" [94]. Plasmas provide enough energy to fragment and recombine gaseous monomers and thus are able to produce polymerised deposition.

Plasma polymerisation differs from traditional polymerisation in many several aspects. First of all, polymers formed by plasmas are different from traditional polymers in that they don't have the repeat structure that normally describes a polymer chain. The materials tend to be more cross-linked, and not soluble in solvents. Plasma polymers also tend to deposit as thin, pin-hole-free films [87,95].

Polymers created by plasma have been measured to be highly cross-linked and appear to have random structure [96]. Radicals in the plasma can be trapped in plasma polymer, hence the material produced by plasma polymerisation is very different to film produced from the same monomer using conventional polymeri-

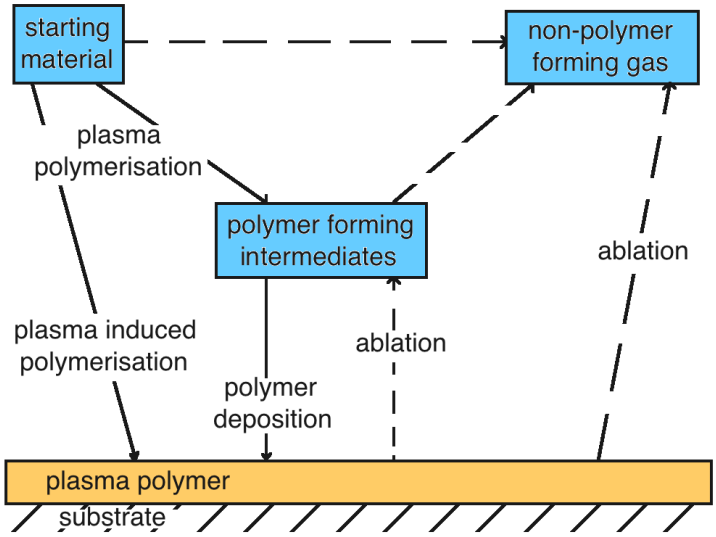

Figure 2.9: Schematic of competitive ablation and polymerisation mechanisms. Adapted from [91].

sation [97, 98], this phenomenon is shown in figure 2.10.

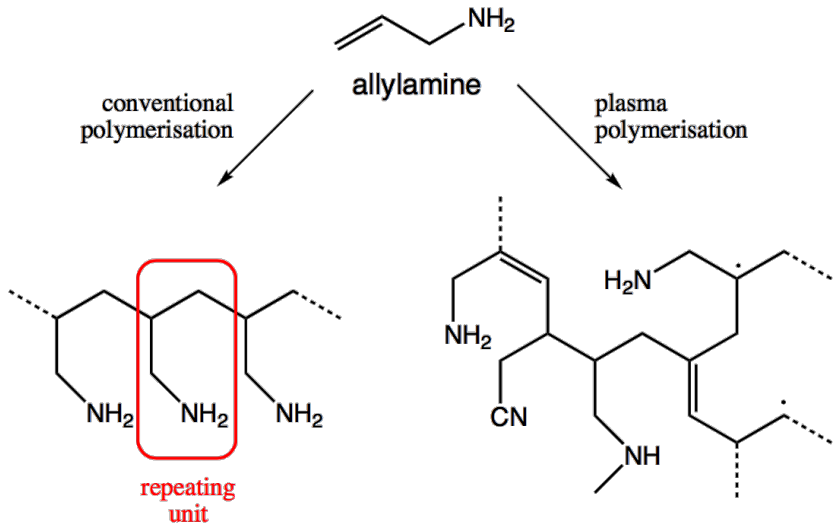

Figure 2.10: Examples of polymers created by conventional polymerisation and plasma polymerisation from allylamine. Taken from [96].

Another difference between plasma polymerisation and conventional polymerisation, is that plasma polymerisation requires very little surface preparation.

Furthermore the possibility of doing plasma pre- or post-treatment, is greatly facilitated as the plasma reactor is already installed on the polymerisation device.

The process is solvent free, does not require an increase in temperature allowing the use of fragile substrates, and can deposit a film over complex geometries, and finally, allows the deposition of very thin films, down to a few nanometres of thickness [99].

Although plasma polymerisation is being studied, and even used in commercial devices for decades, its processes remain poorly understood [100]. This problem leads to difficulties in performing similar depositions from one reactor to another or to scale up a performing reactor [101].

Low-pressure plasmas, typically using RF (13.56 MHz), are often used to deposit polymeric films. Two recent papers analyse the variability and reproducibility of low-pressure plasma polymerisation of 14 different configurations [87, 100]. Some of these low-pressure systems allow the deposition in a large-scale volume, however the cost of the vacuum pumps and equipment required are expensive and complex. Thus simpler atmospheric plasma polymerisation devices have been and still are being studied in laboratories [102–104]. The surrounding ambient air of these systems adds new complex chemistry to an already complex polymerisation process, due to plasma interaction with the molecules contained in air (N_2, O_2, H_2O, Ar, CO_2, etc.). To see the effect of the surrounding atmosphere on the polymerisation some papers have performed their experiment in a modified controlled surrounding [105, 106].

The plasma parameters are numerous (pressure, power, frequency, carrier gas composition, monomer concentration, duty cycle, etc.) all these parameters can be modified and can influence the polymerisation process and hence the quality of the deposition. The high complexity of the plasma polymerisation systems is both an advantage and disadvantage. It is beneficial in that it allows each system to be more flexible, having different ways to be improved by varying the parameters and thus allow a better control on the deposition of polymer films. However, a drawback is that as numerous parameters have to be well chosen to be able to have a decent deposition, this increase the level of possible arising problems and also the variability between two different systems.

Yasuda in [91] analysed many different polymerisations of different monomers whilst varying several different parameters. He defined the parameter $W/(FM)$,

which was later called the Yasuda parameter (Y), where W is the plasma discharge power, F the volume or the flow rate, and M the molecular weight of the monomer. Numerous studies have analysed the characteristics of plasma polymerisation according to this parameter and found that it is often a good scaling parameter enabling the comparison of different plasma polymerisations across various input parameters. [100, 107–114].

2.3.2 Growth in Plasma Polymerisation

Growth in plasma polymerisation process is very complex as it involves a high quantity of different reactions and hence multiple possible paths. *Plasma Polymerisation* written by Yasuda in 1985 describes five possible polymerisation mechanisms for the so-called "step-growth" principle shown in figure 2.11 [91].

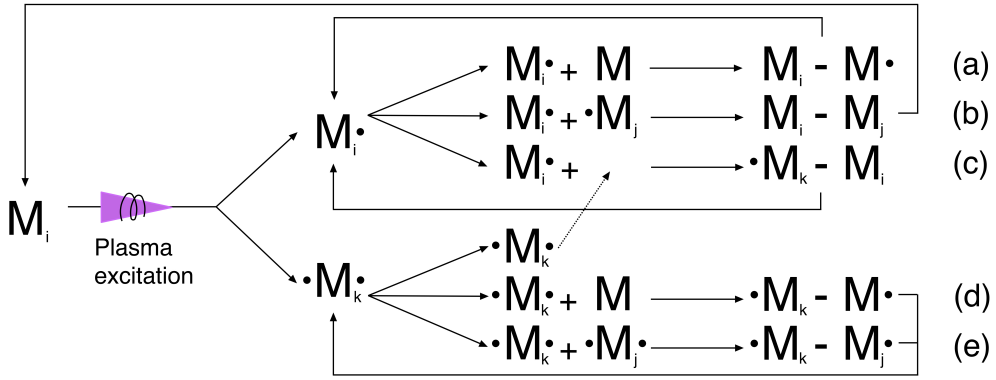

Figure 2.11: Mechanisms of plasma polymerisation: **M** represents a molecule or atom and the · represents the ability of an activated species to create a covalent bond. The letters (a) to (e) show the different possible paths. Redrawn from [91].

The **M**·, In figure 2.11, represents the ability of an activated species to create a covalent bond. An activated molecule can be a free radical or an ion, for example the opening of a double bond by ionisation produces an ion-radical [91]. Yasuda explains that many species in the plasma do not contribute to the polymerisation but rather reduce the production of polymers and that among all the species contained in the plasma, free radicals are probably the most important in terms of contribution to plasma polymerisation. Neutral radicals, like OH·, do not gain energy from an applied electrical filed, however, they are highly reactive as they are ready to form a covalent bond with other radicals (figure 2.11b-c,e) or neutral

molecules containing a double bond (figure 2.11a,d). Radicals have been referred to as the building blocks in traditional polymerisation [87].

Unfortunatly the plasma excitation also fragments polymers and monomers, leading to a depolymerisation. These smaller polymers and fragments of monomer participate in the polymerisation process.

Fourier transform infrared (FTIR) spectroscopy results show that plasma polymerisation occurs mainly through the opening of double bonds [104]. FTIR of plasma-polymerised acrylic acid compared to pure acrylic acid has been measured. The absorption line of the carbon-carbon double bond drops to almost zero as seen in figure 2.12.

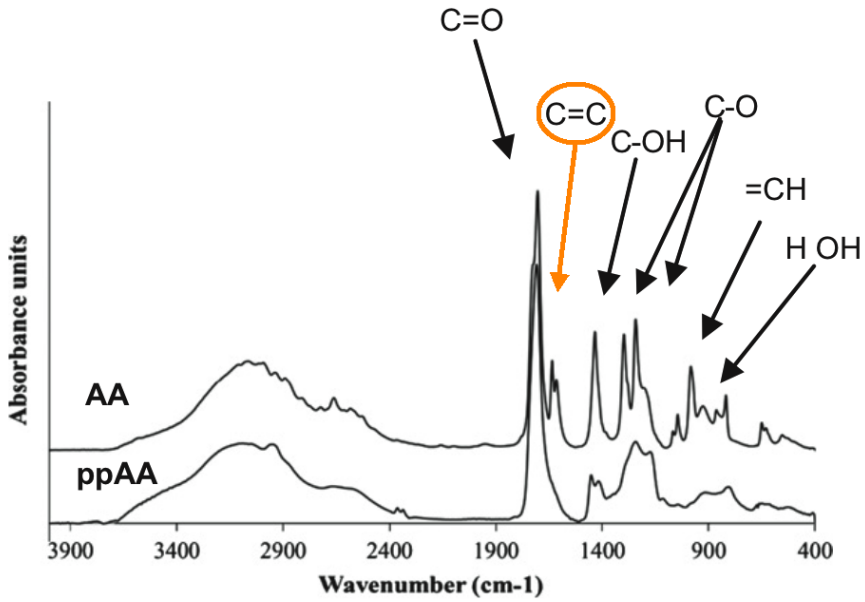

Figure 2.12: FTIR of monomer acrylic acid (AA) and plasma polymerised acrylic acid (ppAA). Taken from [104].

2.3.3 Acrylic Acid and Heptylamine

Acrylic acid is an organic compound with chemical formula of $C_3H_4O_2$ as seen on figure 2.13. Acrylic acid has a molecular weight of 72.06 Da, is a colourless liquid at room temperature and atmospheric pressure, and has an acrid odour. It is made of a carboxyl group (-COOH) and a vinyl group (-CH=CH_2).

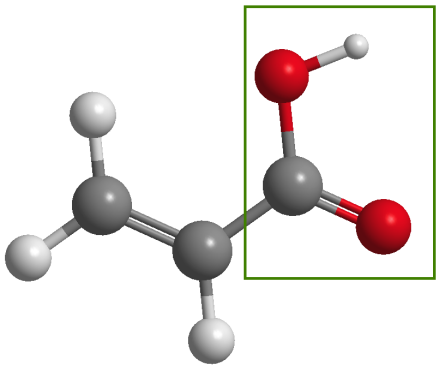

Figure 2.13: Representation of an acrylic acid molecule (grey: carbon; red: oxygen; white: hydrogen). The green square shows the functional carboxylic group.

The polymerisation through the carbon double bond produces poly(acrylic) acid as can be seen in figure 2.14.

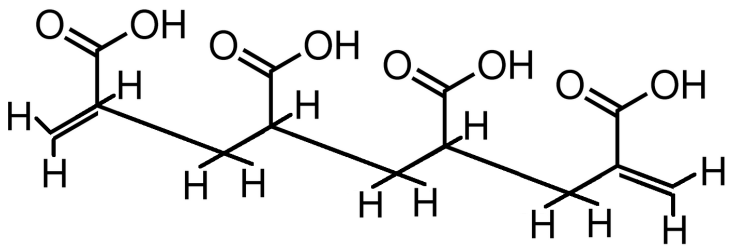

Figure 2.14: Representation of a poly(acrylic) acid oligomer.

Heptylamine is also an organic compound, containing a nitrogen atom its chemical formula is $C_7H_{17}N$ (see figure 2.15). Its molecular weight is 115.22 Da and is a carbon-chain containing a functional group called primary amine (-NH_2) at the end. Polymerisation is supposed to increase the length of the carbon-chain while maintaining the amino group.

Poly(acrylic) acid and heptylamine films are being used for several applications in sensor technology, in life sciences [28, 95, 115–118], and for super hydrophobic coatings [30, 119, 120].

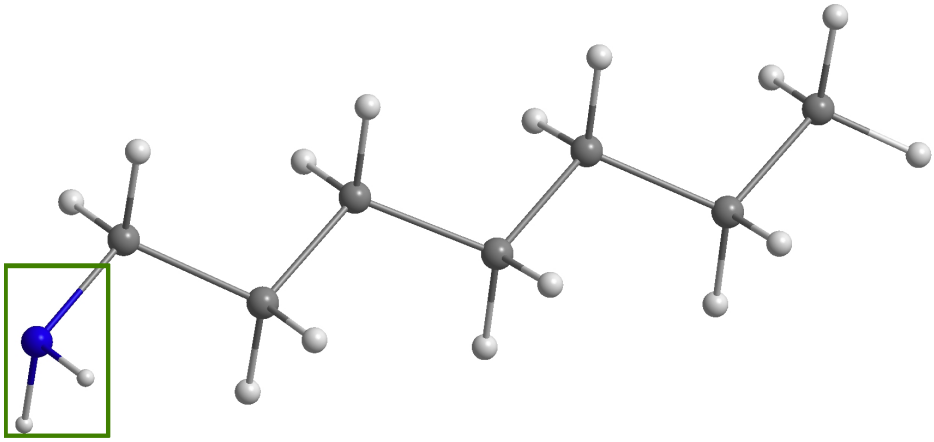

Figure 2.15: Representation of a heptylamine molecule (grey: carbon; blue: nitrogen; white: hydrogen). The green square shows the functional amine group (-NH_2).

2.4 Atmospheric-Pressure Plasma Jet Polymerisation

The retention value of a functional group of a deposited film is of great importance, high retention is often the key for good properties of the film. Low-pressure and atmospheric-pressure plasmas have been analysed to determine the factors which have the biggest impact on the retention of a functional group in the film deposition. High retention of functional groups have been seen to be obtained using low-pressure pulsed plasmas or with continuous wave plasmas using a low Yasuda parameter (Y) value.

It has been reported that for low-pressure plasmas that at low Y, depositions of acrylic acid have a high retention of the functional group but the polymers are not cross-linked and thus are soluble in water and out-gas with time. However, at high Y, the deposition is made of a more cross-linked material but the functional group retention is lower [121].

Candan *et al.* reported that ions have an important role in plasma polymerisation. Their study challenges the conventional polymerisation view which says that the radicals and neutrals have the main roles in plasma polymerisation [122].

Barton *et al.* used a bias substrate in a low-pressure plasma to filter the ions depending on their energy at the substrate. They reported that by modifying the bias the ion energy, and therefore the species, arriving onto the substrate

could be filtered. The surface chemistry was barely affected by changes in the bias which suggested that the main polymerisation pathway for acrylic acid film growth was the neutral grafting[1] onto free radical sites and not the ions-molecules mechanism [123].

Voronin *et al.* analysed the retention of carboxyl group of low-pressure pulsed plasmas of acrylic acid as a function of power and duty cycle. The retention of the functional group was found to be strongly influenced by the time-averaged power whereas the total deposition rate (without necessarily a high retention of functional group) is more dependent of the gas flow rate [124]. They also reported that the retention increases with the duty cycle and that ionised polymers are created in both on- and off-times [110]. It was also found that ions heavier than m/z >30 Da remained longer than lighter ions which decayed more quickly [125].

The main advantage of atmospheric-pressure plasma processes is the lower investment cost and the simplicity of implementation in assembly lines [126]. Wan *et al.* developed an atmospheric-pressure volume DBD to deposit poly(acrylic) acid on PTFE. The polymeric film was grafted on the PTFE surface with a high retention of carboxyl group [127].

An atmospheric-pressure ultrasonic nozzle was used in a glow discharge DBD system to atomise acrylic acid monomers in order to deposit poly(acrylic) acid [102]. The deposition showed good properties such as wettability, good adhesion, and good gas barrier characteristics. It was also reported, using XPS and FTIR, that polymerisation proceeds preferentially via the carbon double bond [102].

As is seen in low-pressure plasma [121], the properties of poly(acrylic) acid deposited using atmospheric-pressure plasma jet depend strongly on the Yasuda parameter. Depositions made with low power and high flow rate present a higher retention of the functional group, but are soluble in water [103]. Poly(acrylic) acid films showing similar properties (good retention and soluble to water) have also been deposited using an atmospheric-pressure plasma torch by Donegan *et al.* [30].

Poly(acrylic) acid has been deposited mainly on flat substrates such as glass or PTFE, Chen *et al.* reported deposition on silk fibers using an atmospheric-pressure plasma jet. The coated fibres presented an antimicrobial activity and inhibit E. coli bacteria better than the non-treated fibres [120].

[1] A graft polymer is a polymer which is grown off of a substrate.

It has been recently reported by Zheng *et al.* that a He/O_2 atmospheric-pressure plasma jet deposits films with much higher retention than an Ar/O_2 APPJ [128]. In this experiment O_2 was bubbled through liquid acrylic acid and the mixture was injected in an Ar or He plasma jet.

Oh *et al.* analysed polymerisation of heptylamine using an APPJ in air and in dry nitrogen surrounding atmosphere. Heavy polymer ions (up to $[6M+H]^+$) have been detected in both air and nitrogen. More species were detected by mass spectrometry in air than in nitrogen due to higher possibilities of chemical reactions in the plasma plume [105].

2.5 Atomic Layer Deposition

Plasma deposition is a common technique used worldwide. It is used for many application such as polymerisation as described above. Another deposition technique, which is particularly used in the semi-conductor industry, is the atomic layer deposition (ALD). ALD is a deposition technique which consists of exposing the substrate alternatively to different gases in a repetitive cycle and, relying on the self-limiting surface reactions, grows the chemically desired film atomic layer-by-atomic layer. This way of depositing films layer by layer make ALD the technique with the highest deposition thickness control on the market. This section describes the history, the mechanisms, and the commercial use of ALD as well as the description of the plasma-enhanced ALD technique.

2.5.1 History

The origin of atomic layer deposition is not so certain[2]. Two groups in the '60s were working on an advanced deposition technique. One research group, led by Aleskovskii at the Leningrad Lensovet Technilogical Institue, in Russia, was working on "molecular layering" [129]. However, the person who is most recognised as being the father of ALD is Dr. Tuomo Suntola from Finland. In 1974, he and his group at the R&D of the Instrumentarium Oy, developed a process to deposit zinc sulphide (ZnS) used in electroluminescent displays [129].

[2]A virtual project, led by Riikka Puurunen and Jonas Sundqvist, on the history of ALD is still in progress (http://vph-ald.com/index.html).

Suntola is said to have thought of a technique to deposit a thin film by injecting sequentially two compatible compounds while looking at a periodic table. The idea was that if the complementary compounds make a stronger bond with each other than with themselves a deposition of a mono-atomic layer could be performed [130].

The first deposition was made a few months later and the ZnS film made by ALD was stronger than previous methods, and it showed hydrophobic properties[3] [130]. It was also observed that the deposition structure was different compared to traditional deposition processes (sputtering and evaporation). Suntola called this new technique atomic layer epitaxy (ALE)[4] to emphasise the structural growth of the deposition and patented the technique in 1974 [131].

In 1983 the first large electroluminescent display made using ALD was installed at the hall of the Helsinki-Vantaa airport and was operational until 1998 [132]. From 1985 to 1990 ALD was commercially used without undergoing much change. Starting in the '90s the microelectronic industries happened to have need of a high quality deposition technique for very thin films as the semiconductor size quickly arrived at the dimensions lower than a micrometre. Given the importance of integrated circuits having the progression we know of today, the ALD reactor was in demand, and hence the development of them rapidly increased during the '90s [133].

2.5.2 Description

A basic atomic layer deposition cycle consists of sequentially injecting two gases into a chamber containing the substrate. Figure 2.16 shows a simple diagram of a typical ALD cycle.

The active gases, called precursor (A) and reactant (B), have self-limiting properties which means that once the gas species have been attached onto all the nucleation sites available, no more deposition occurs. This effect can been seen by varying the gas step of one of the gases whilst keeping the other gas steps constant and long enough such that the reaction with the other gas is certain to have been achieved. A so-called "saturation curve" of the growth rate can be measured (as can be seen in figure 2.17) and thus the minimum time needed to

[3]Hydrophobicity is the physical property of a material to repel water.

[4]The term epitaxy comes from the Greek $\varepsilon\pi\iota$ = "above" and $\tau\alpha\xi\iota\zeta$ = "an ordered manner"

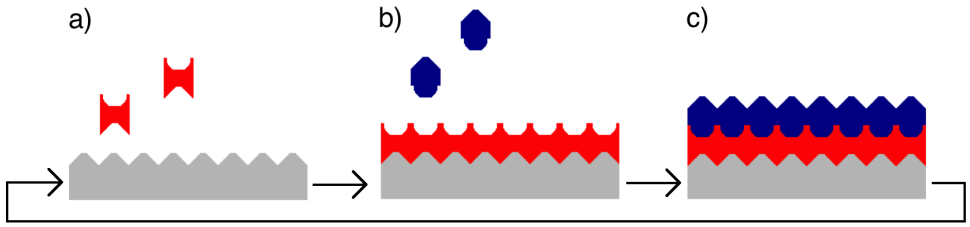

Figure 2.16: Schematic of an ALD cycle with 2 gases having self-limiting deposition properties. As the symbolic representation of the gas molecules is showing, the gas molecules cannot react with itself. However, the 2 different gases are chosen to react strongly with each other. To avoid reaction between them in the gas phase, the 2 gases are injected one after each other in the chamber, reacting only with the sample surface.

have complete saturation is known [134]. The measurement is then repeated for the other gas.

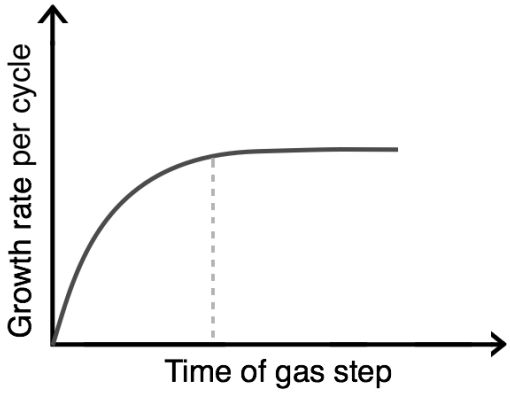

Figure 2.17: A typical saturation curve of the growth rate per cycle. The dotted line corresponds to the minimum duration of the step.

The gases chosen in ALD do not react with themselves and thus no chemical vapour deposition (CVD) happens above the surface, only reactions with the top molecular layer of the surface occur. However, the precursor and the reactant can react with each other. Therefore, to avoid any unwanted CVD reactions, a purge is performed between each gas step. As Georges describes in [132], ALD processes can be one of two types, either with a carrier gas, or without. The carrier gases used in ALD are inert gases, typically argon or nitrogen. The carrier gas increases the speed of the precursor and reactant delivery and decreases their purging time by pushing out the remaining gas. It can also allow the use of a liquid precursor.

Most ALD reactors use a carrier gas mainly for the reduction of the purging step time needed, and hence the total cycle duration.

The typical pressure of an ALD cycle is around 1 Torr, at this pressure, collision rate and density are the most important parameters for a fast and homogeneous deposition. The density of the precursor and reactant is high enough to quickly reach all the nucleation sites on the substrate and the collision rate is high enough to remove the active gases by the purge gas in a reasonable time [132].

To summarise, an ALD cycle is composed of four sequential phases:

1) The injection of the precursor (A).

2) The purge of the precursor and by-products.

3) The injection of the reactant (B).

4) The purge of the reactant and by-products.

The total AB cycle deposits a single atomic layer (a monolayer) of the chosen film. The deposition rate is then either given in thickness per time or thickness per cycle. The actual deposition thickness per cycle does not correspond exactly to a monolayer thickness. This disagreement is due to the surface species and the surface chemistry [132]. Generally, the growth rate per cycle averages to $\sim 1/3$ of the monolayer thickness.

To increase the deposition rate, the cycle needs to be as short as possible as the deposition rate per cycle is constant. Saturation curves are thus performed for step 1) and 3) of the cycle to determine the minimum duration of the respective phase. The duration of the purge of the precursor is also reduced to its minimum. The minimum time of the purging step is just before CVD occurs between the residual precursor and the injected reactant or vice versa.

In order to have short cycle time, precursors and reactants must react quickly with the surface to reach saturation in a short time. Leskelä *et al.* stated that "the desired ALD reaction should have a large negative ΔG value" implying an aggressive reaction between the gas and the surface [133]. The Gibbs free energy (ΔG) is the available energy in a chemical reaction. This implies that the properties of the combination of the precursor and the reactant need to be well chosen. The Gibbs free energy is also temperature dependant.

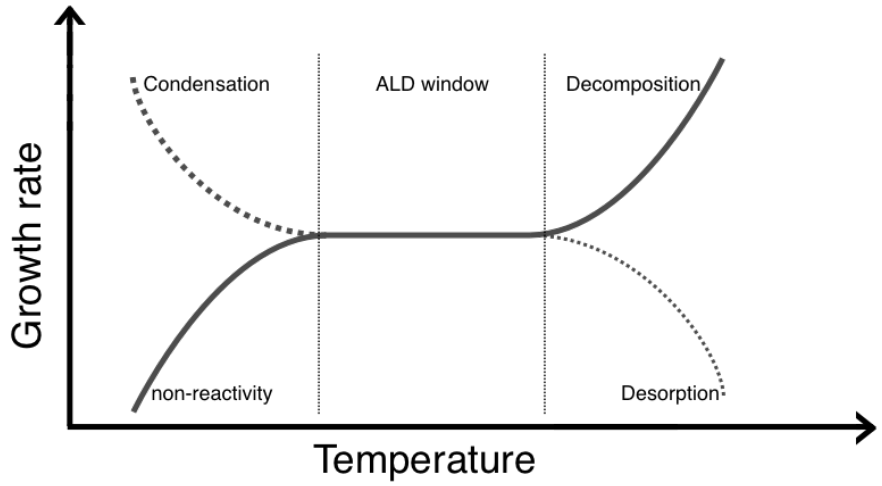

Figure 2.18: Growth rate as a function of the process temperature, the area between the dotted lines is called the ALD window or the ALD process window. Taken from [135]

For an ALD process with a given pressure and gases, there is a range of temperature, called the ALD window, which results in a monolayer deposition. Figure 2.18, shows the evolution of the growth rate as a function of the temperature. When the temperature is higher than the ALD window one or both of the active gases decompose everywhere in the chamber volume leading to a CVD-like process [136]. Desorption of the surface can also occur due to the heat. At a temperature lower than the ALD window the thermal energy is either not high enough to enable the chemical reaction in the surface-gas region, or the time needed for the reaction to happen is substantially decreased. In some cases a low temperature can lead to a condensation of one of the gases and hence to a multiple layer adsorption to the surface [136]. As Parsons *et al.* wrote "the growth rate within the ALD temperature window is determined by the density of available reactive sites on the surface and the optimum saturation occupancy of those sites by the adsorbed precursor" [129].

2.5.3 Commercial Use

Due to its properties, the atomic layer deposition technique is used in industrial firms for several applications. The first film to be deposited was ZnS by Suntola's group, nowadays several different film compositions are deposited using this technique, the most common being Al_2O_3 due to its stability and aggressive

Thin Film Product	Example Precursor	Reactant	ΔG (kcal/mol)
Al_2O_3	$2Al(CH_3)_3$	$3H_2O$	-370
ZnO	$Zn(C_2H_5)_2$	H_2O	-72.6
TiO_2	$TiCl_4$	2 H_2O	-20.3
SiO_2	$SiCl_4$	2 H_2O	-37.3
HfO_2	$HfCl_4$	2 H_2O	-31.5
W	WF_6	SIH_4	-130

Table 2.1: Example precursors and reactants for some common ALD materials and the free energy change for the overall deposition reaction. Taken from [129].

deposition reaction (see table 2.1). There are several commercial uses of ALD, the most common are: Al_2O_3, for electroluminescent structures [137], insulated films in integrated circuits [138], and for electrical tunnel barriers [139]; TiO_2, for several applications such as chemical sensors and solar cells [140]; metal and nitride thin films for semiconductor devices [136], and ZnO for oxide-based thin film transistors [141].

2.6 Development of ALD

This section is about the improvements brought to ALD since its beginning. The main drawbacks of ALD are the slow deposition rate and the limited composition of the deposition. Two techniques have been used to improve the speed of the deposition rate, batch ALD and spatial ALD. Classic ALD consists of a single wafer put in a heated chamber where the precursor and the reactant are sequentially injected in. In batch ALD the reactor is bigger allowing the placement of several wafers. In spatial ALD, the substrate moves from an area containing the precursor to an area containing the reactant, both gases are spatially separated by a wall, inert gases, and/or a pumping system. The substrate moves either horizontally through several successive ALD steps or in a closed loop, depending on the reactor type [142]. The firm Beneq is selling a roll-to-roll ALD reactor for flexible films using spatial ALD. The performance is a deposition thickness of 25 nm for a web speed[5] up to 2 m per minute [143].

The limited composition of the deposition can be partially resolved by the use of a plasma during one or more additional steps of the cycle, it is known as

[5]The web speed is the speed of the deposited substrate going out of the machine.

plasma enhanced ALD (PEALD) also called plasma-assisted ALD.

2.6.1 Plasma-Enhanced Atomic Layer Deposition

In ALD, single element depositions using thermal ALD is difficult to produce [144]. Plasma-enhanced ALD can help with these cases and enable other precursors to be used in an ALD process. A plasma is added during one of the steps of the cycle as shown in figure 2.19. In this figure the step using the reactant (2.19v) is shown for a thermal ALD (2.19vi) and with a plasma-enhanced ALD (2.19vii). The plasma activates the reactant giving energy to the gas and allowing it to react more intensely with the surface [134]. The plasma can also induce reactions which are not possible with classic ALD [145].

The plasma in PEALD does not increase the process temperature for two reasons. Firstly, plasmas used in PEALD are cold plasmas which barely heat the system. PEALD deposits films at room temperature [146]. Secondly, the plasma is used only for a fraction of the cycle, limiting its effect on the whole cycle.

The first PEALD was performed in 1991 using a H_2 plasma [147]. It has even been shown that PEALD of Al_2O_3 performed at low temperature gives better electrical properties and a denser bulk [146]. The possibility to produce ALD films at low temperatures allows the utilisation of thermally weak substrate material like polymers. For different thin film processes plasma etching or plasma cleaning must be performed [148], already having a plasma reactor in the ALD chamber is therefore an advantage.

The addition of plasma to ALD, however, does not only improve the process, it can also hinder it. Table 2.2 shows the advantages and disadvantages of PEALD. PEALD can also damage the films due to accelerated ions going through the plasma sheath and bombarding the surface of the substrate. The UV photons created by the plasma can also damage the surface.

The poorer conformality comes from two different effects, the first lies in the difficulty of achieving uniformity in the plasma. Even when ALD is one of the best deposition techniques concerning the uniformity of the film, PEALD needs to have a uniform plasma in order to have all the available reaction sites filled [134]. The second is the problem of radical recombination with the surface, which reduces the deposition on high aspect ratio profiles [142]. For high aspect ratio, such as deep trenches, the active species in the gas needs to reach the bottom of the

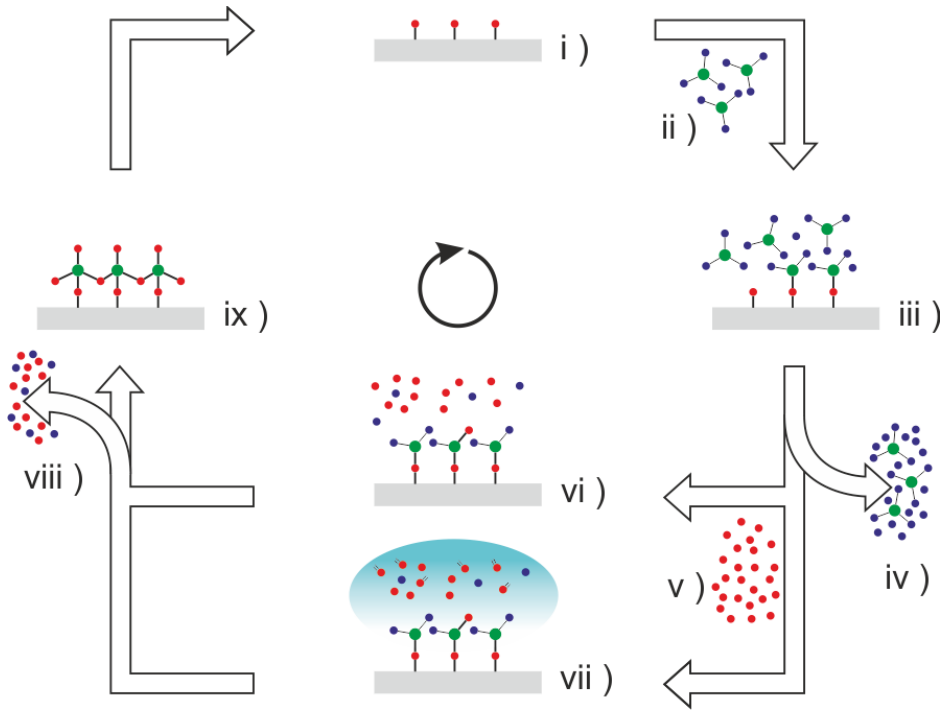

Figure 2.19: ALD and PEALD cycle: i) the chamber is purged of reactive gas, then the two active gases are transported alternatively into the chamber [ii) and iv)] where the half reaction steps occur [iii), vi) and vii)]. To avoid contact between the two precursors, an inert gas is used to purge them [iv) and viii)]. After the two full reactions the top atomic layer [ix)] is the same as before the cycle [i)]; the process can be repeated.

trenches. For classic ALD this may not be a problem because the active species are everywhere in the precursors, thus as long as the gas molecule can reach the bottom of the trenches ALD can occur. For PEALD , if the substrate has a profile with high aspect ratio, the plasma sheath will accelerate the ions on the side of the trenches before they can reach the bottom. For the radical species, being neutral, they do not feel the electric field from the plasma sheath. However, the chance of contact with a surface before reaching the bottom is high in a deep trench and therefore they may lose their reactivity before reaching the bottom.

Pros	Cons
Lower deposition temperature	More complicated chamber design
Broader range of chemistry possible	More complicated reaction chemistry
Denser films	Potentially poorer conformality
Lower impurity	(Damage to films)
In situ plasma treatments	
Can used thermally sensible substrate	
(Faster)	

Table 2.2: Pros and cons of PE-ALD. The brackets mean that it is not always the case that the effect appears. Table reproduced from [135]

2.7 Analysis Technologies

This section introduces and describes the different technologies used in this thesis. Mass spectrometry is presented focusing on the quadrupole and the time-of-flight analyser. A small section on detectors is also described. Lastly, X-ray photoelectrons spectroscopy is presented.

2.7.1 Mass Spectrometry

Sir Joseph John Thomson developed the ancestor of the modern mass spectrometers at the beginning of the last century [149]. His student Francis W. Aston improved the spectrometer design [150, 151] and was awarded the Nobel prize for Chemistry in 1922 for his work.

Nowadays, mass spectrometers are a very common analytical method used in a wide range of scientific domains for various applications. A mass spectrometer consists of an ionisation source, a mass analyser, a detector, and a computer. The analyser and the detector are under ultra high vacuum to avoid collision of the collected particles. Mass spectrometers record mass-to-charge ratio (m/z) of ions.

Different sources of ionisation are available, in this thesis the plasma is used as the source and ions detected are being created by the plasma device before entering the mass spectrometer.

Mass Analyser: Quadrupole

Introduced in 1953, the quadrupole analyser, shown in figure 2.20, is a type of mass analyser [152]. The pairs of rods are driven by a combination of DC and RF signals. The rods then act as mass filter, the currents affect the ions trajectory and only ions with a specified m/z ratio get through the analyser section; the other ions collide with the rods, the walls, or the exit panel (see figure 2.20).

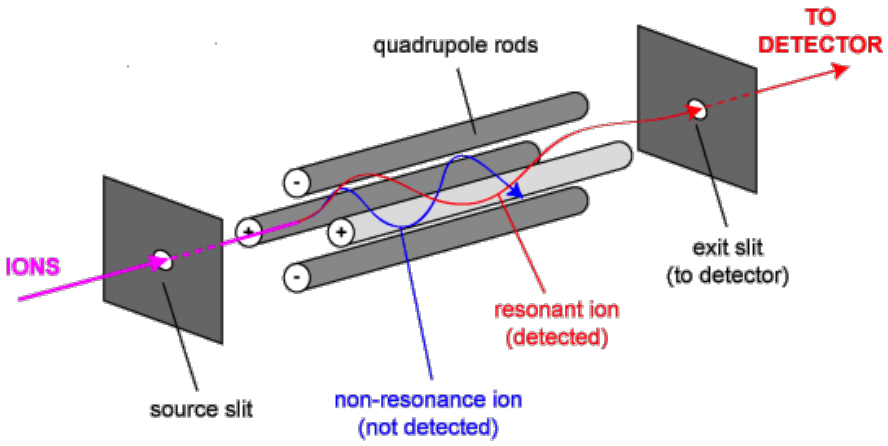

Figure 2.20: Schematic of a quadrupole analyser. Taken from [153].

Mass Analyser: Time-of-Flight

Stephen and Wolff described the premise of a new kind of mass analyser using the time of flight (TOF) of particles to calculated their mass-to-charge ratio in [154]. The first TOF mass spectrometer was commercialised in the '50s. TOF analysers have a high sensitivity and no upper mass limit. They consist of a flight tube with an acceleration region at one side and a detector at the other, as is shown in figure 2.21.

The ions are thus detected according to their velocity, which depends on their m/z ratio. As their is no electric field in the flight tube, the velocity is constant ($v = d/t$). With potential and kinetic energy being equal in the acceleration zone. We have $E_\mathrm{p} = E_\mathrm{k}$ which is equivalent to $zU = \frac{1}{2}mv^2$, as E_k is $\frac{1}{2}mv^2$, and E_p corresponds to the ion charge multiplied by the electric potential (zU). Hence

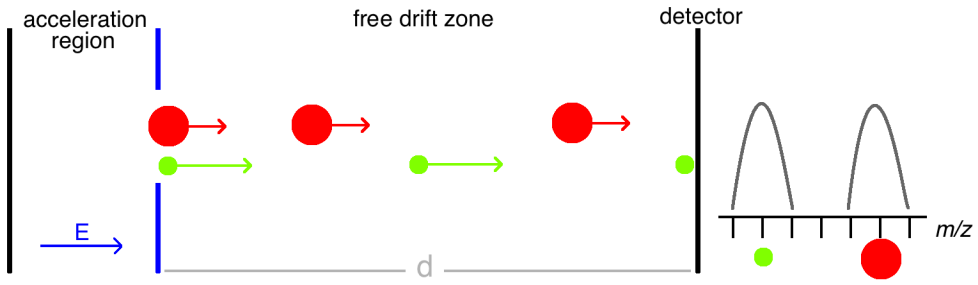

Figure 2.21: Schematic of a TOF analyser. Adapted from [155].

equation 2.3 is obtained.

$$t = d\sqrt{\frac{m/z}{2U}} \tag{2.3}$$

However, TOF analysers have poor resolution due to the variation of initial velocity of ions with the same mass-to-charge ratio, this leads to the broadening of each peak. To solve this problem different solutions were designed: the reflectron and the orthogonal acceleration device.

The reflectron is an electro-mirror which reflects the ions at the end of the flight tube back to the detector placed next to the acceleration section [156]. Ions with same m/z ratio but with higher initial kinetic energy will be faster when arriving in the reflectron, hence they will enter deeper into it, lengthening their path compared to ions with a lower initial velocity causing the ions to arrive at the detector at the exact same time.

Another design is the orthogonal acceleration in TOF analysers proposed in 1964 [157] and properly developped in the '90s [158, 159]. By placing the acceleration region perpendicular to the ions source, the orthogonal acceleration TOF reduces the effect caused by differences of the initial velocity for ions with the same m/z ratio.

2.7.2 Detectors

Detectors are able to detect and emit a usable signal for each selected ion. The most common type of detector is the electron multiplier. These detectors multiply the collected signal by a cascade effect as seen in figure 2.22. Electron multipliers produce a gain in current by a factor of 10^5 to 10^8 using the process called secondary emission.

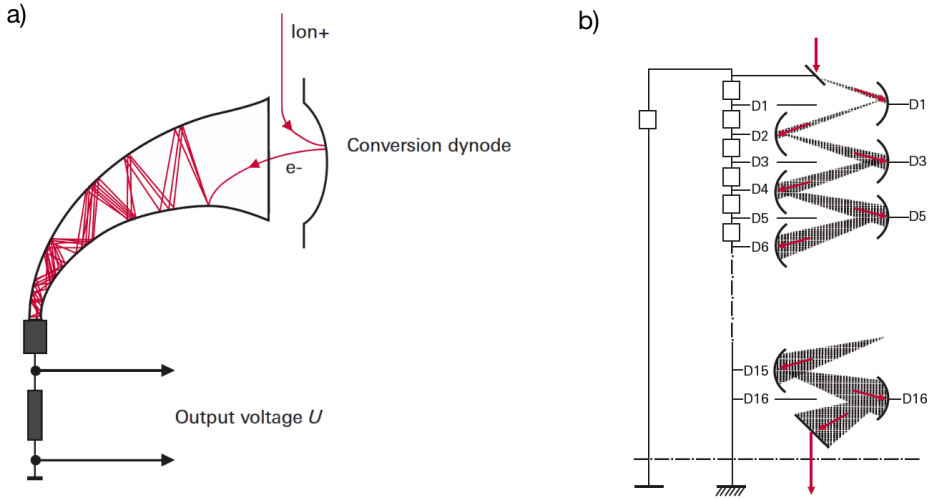

Figure 2.22: Schematic of a electron multipliers: a) continuous-dynode electron multiplier, b) microchannel plate electron multiplier. Taken from [160].

2.7.3 X-ray Photoelectron Spectroscopy

X-ray photoelectron spectroscopy (XPS) is a surface analysis technique. An X-ray containing photons of a particular energy (monochromated X-ray) is incident on a sample surface. The beam reacts with molecules, atoms, and intermolecular bonds at the top of the bulk. The energy of the X-ray is greater than the binding energy of the surface allowing the creation of photoelectons which are subsequently collected by the extractor [161]. To avoid reaction of the detached electrons before reaching the detector, a high or ultra-high vacuum is required.

The binding energy (E_{B}) of the photoelectron can be calculated using the following equation:

$$E_{\mathrm{B}} = h\nu - E_{\mathrm{k}} - \phi \tag{2.4}$$

with h: he Planck constant, ν: the frequency of the associated electromagnetic wave of the X-ray, E_{k}: the kinetic energy of the photoelectron measured by the XPS device, and ϕ: the work function which is a constant related to the spectrometer and the surface material corresponding to the energy needed to separate the electron from the bulk. The product $h\nu$ is the energy of the monochromatic X-ray (Plank-Einstein relation).

The binding energy does not depend solely on the elemental composition, but also on the neighbouring atoms, the chemical environment of the atom. Hence,

the XPS can detect the composition of a surface as well as information about its chemical state [162].

In some particular cases when a particular chemical bond cannot be distinguished a derivatisation process can be applied. This process consists of chemically modifying every specific chemical bond of the bulk into another molecule easily distinguishable by an XPS scan. For example, acrylic acid contains a carboxyl group (-COOH) which is undistinguishable from another similar group, such as -COONa for example, when looking at the carbon bonding energy; they will be under the -COOR binding energy (R being any atom or molecule). Derivatisation, such as esterification through chemical reaction, can modify only the carboxyl groups leaving the -COONa group as they are. Further XPS analysis on the derivatised sample will be able to detect the new chemically added group and thus the percentage of -COOR being -COOH and therefore the percentage of -COOR being -COONa can be measured. The derivatisation process is described in more detail in chapter 4, subsection 4.2.1.

Chapter 3

Experimental Setup

This chapter describes precisely all the apparatus used to collect the data. The information written in this chapter is sufficient to help anyone who would like to reproduce the apparatus of this thesis. Furthermore, in the following chapter the methods for gathering the data are described and justified to complete the precise description of the experiments. An example of a jet setup is shown in figure 3.1.

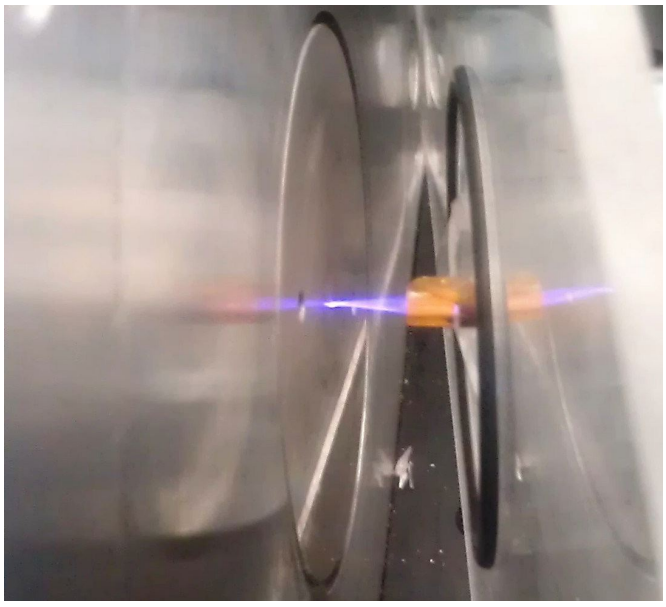

Figure 3.1: Photo of the APPJ directed on the front of the mass spectrometer.

3.1 Dielectric Barrier Discharge

The plasma jet used in this study was a cylindrical dielectric barrier discharge (DBD) as is shown in figure 3.2. It consisted of a 100 mm quartz capillary (outer diameter (OD): 4 mm, inner diameter (ID): 2 mm), with a copper ring electrode (ID: ∼4 mm, OD: 5 mm and 10 mm, and 10 mm in length) attached 5 mm from the end of the capillary (see figure 3.2). Different tubes were used throughout the duration of this study. Deposition inside the tube, due to plasma deposition of the ionised monomer, can affect the quality of the plasma, thus glass tubes were changed as soon as deposition was clearly visible to the naked eye. Glass capillaries were cut using a file and then sanded down to show a clear straight end. The copper ring was custom-made to fit exactly around the glass tube. To avoid displacement along the capillary axis, a small piece of Kapton tape was placed on the glass next to the electrode. The position of the electrode on the glass was measured using a ruler, error in positioning could lead to small differences in replicated measurements. The glass was attached to a custom-built piece of PTFE. Nylon screws were used to fix the glass in position. The PTFE piece was screwed to a manual $x - y - z$ stage (Thorlabs) with a micrometre resolution which was fixed to the table.

The glass tube was fed with helium gas of 99.996 % purity (BOC), at atmospheric pressure using the pressure regulator (BOC). A custom-built connector made of PTFE links the glass tube with the pipe. The gas was fed through 1/4 inch PTFE pipes. The connections used are either plastic (push-in nylon connector from Advanced Fluid Solutions Llc.) or metallic (compression fitting from Swagelok). Some of the initial measurements were made using manual flowmeters (InFlux and Omega). The manual flowmeters were calibrated using a MKS mass flow controller. However, these flowmeters have been seen to be extremely unstable especially when a small flow was used, typically ∼10 sccm (standard cubic centimetre per minute), into a higher flow, typically ∼1 slm[1] (standard litre per minute). The imprecision of the manual flowmeters were creating major problems in finding the right ratio of monomer/carrier gas for the acrylic acid polymerisation. Hence they were replaced by two MKS mass flow controllers. For the acrylic acid experiment, typical flow rates were 1.5 slm for the helium carrier

[1] 1 slm = 1,000 sccm

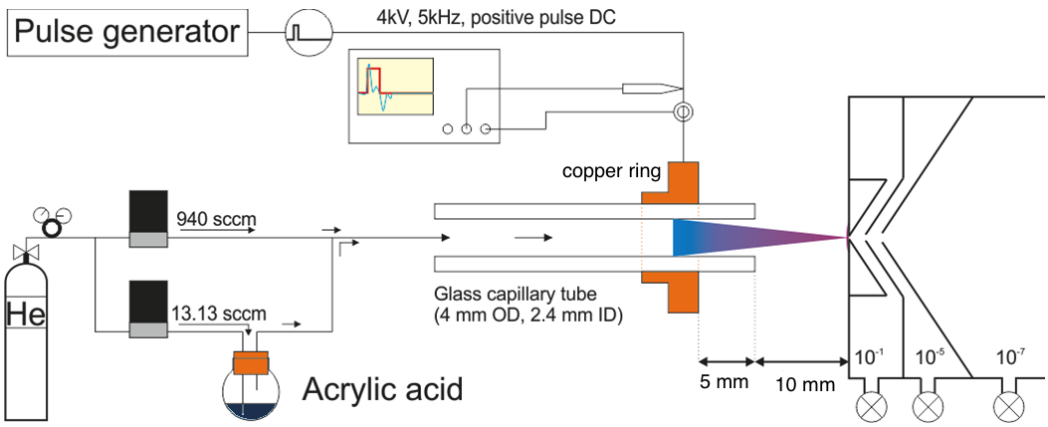

Figure 3.2: An illustration of the DBD jet apparatus for the pulse generator mode. Helium at atmospheric pressure is piped through two mass flow controllers, one line is bubbling into a liquid monomer (acrylic acid here), then joins the other line and flows through the glass tube into the atmosphere. Electrical signal is generated by the power supply, measured using a current probe and a voltage probe connected to an oscilloscope, and fed to a copper ring electrode put around the glass capillary. The plasma is pictured as a blue-purple cone between the electrode and the front of the mass spectrometer. The three pumping regions of the mass spectrometer are represented on the right of the schematic.

gas and 14.6 sccm for the helium-acrylic acid mixture, this mixture allowed for a stable plasma to be formed at all duty cycles applied. Errors and variations in manual flowmeters greatly contributed to problems in reproducibility.

To evaluate the concentration of monomer in the carrier gas, the Antoine equation has been used, given by,

$$\log_{10} p = A - \frac{B}{C + T} \tag{3.1}$$

where p is the vapour pressure, T is the temperature and A, B, and C are constants specific to the fluid composition. The Antoine equation allows one to calculate the partial pressure p of the monomer knowing its Antoine coefficients (A, B, and C), and the temperature. The Antoine coefficients of acrylic acid have been taken from [163], then the ratio of the partial pressure, calculated using the laboratory temperature over the atmospheric pressure, gives the monomer concentration, typically 40 ppm. The Antoine equation is very useful as it allows the evaluation of the monomer density without perturbing the system. However, variations in the temperature greatly affect the chemical concentration; for example, the concentration of acrylic acid doubles when its temperature rises from 22.5 to 32.5 °C.

3.1.1 Continuous Wave Jet

For the continuous wave jet, frequencies between 6 and 40 kHz were used with a peak-to-peak voltage in the range of 5 kV. The apparatus used was the following: a signal generator (TTi TG200) connected as an input to an audio amplifier (STA-800 Stageline). A custom-made step-up transformer (Express Transformers, custom model, maximum: 10 kV and 40 mA, working range: 3-50 kHz) was connected to the output of the audio amplifier and to the electrode. A voltage probe (PINTEK HVP-15HF) and a current monitor (Pearson 2877) were connected to the wire before the electrode and to an oscilloscope (Tektronix DP03034) as can be seen in the schematic in figure 3.3

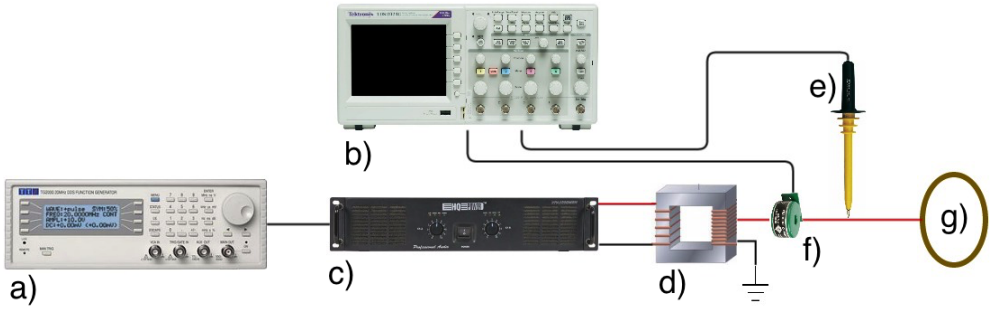

Figure 3.3: The apparatus used to generate to generate the continuous wave signal as described in section 3.1.1 with a) signal generator, b) oscilloscope, c) amplifier, d) transformer, e) voltage probe, f) current monitor, and g) copper ring electrode.

3.1.2 Positive Pulsed DC Jet

The jet was powered using monopolar pulsed excitation. The positive pulsed DC power supply consists of a high power supply going through a custom-built device made by Dr. James Walsh. The input of the device receives the signal created by a pulse generator (DG645, Stanford Research Systems), and requires a low voltage of ∼50 V. The output signal is a positive pulse with ∼4 kV peak-to-peak amplitude and with a short rising and falling time of ∼40 ns. The voltage probe used was the Tektronix P6015A. The frequencies used were 5 and 10 kHz and the duty cycle was varied from 5 to 90 %. The apparatus is shown in the schematic in figure 3.4 where some of the components have already been described above (section 3.1.1).

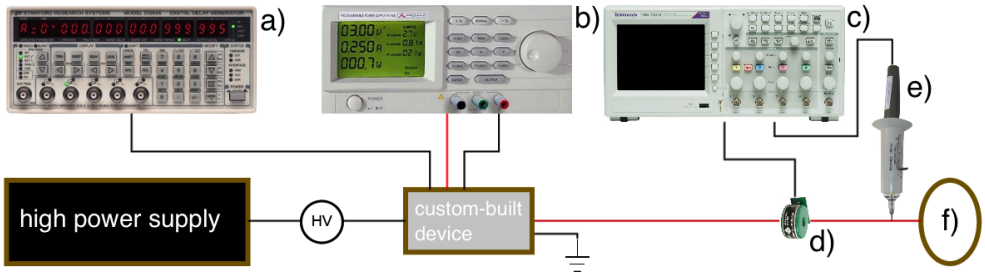

Figure 3.4: The apparatus use to generate the DC pulsed signal as described in section 3.1.2 with a) pulse generator, b) low-voltage power supply, c) oscilloscope, d) current monitor, e) voltage probe, and f) copper ring electrode.

3.1.3 Surface Discharge

The surface discharge was used for the PEALD experiment. The design is the following: the two electrodes (aluminium tape) are glued on either side of a 1 mm thick perspex disc with a 30 mm radius, a dielectric epoxy is moulded around the driven electrode (more details in subsection 3.4.1). The power supply consists of a signal generator which fixes the frequency, a power supply, which controls the signal amplitude, and a custom built electronic board (designed by Dr. James Walsh) which transforms the signal generator and the power supply inputs into a modulated signal. The output is then connected to a custom high voltage transformer (Amethyst) to create a signal from 1 to 15 kV. The apparatus is shown in the schematic in figure 3.5.

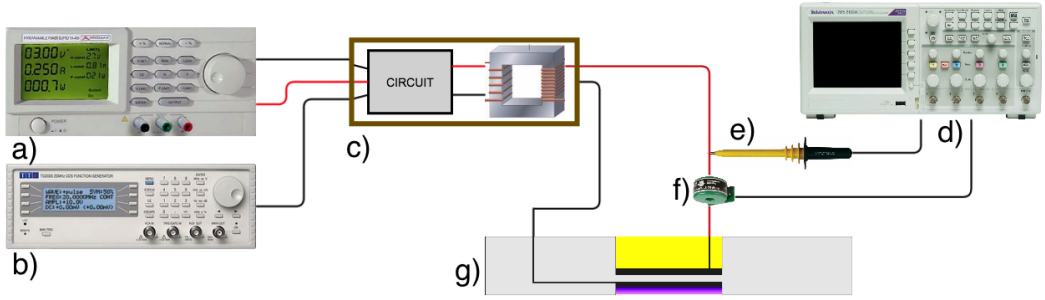

Figure 3.5: The apparatus used for the surface discharge reactor as described in section 3.1.3 with a) power supply, b) signal generator, c) electronic board & transformer, d) oscilloscope, e) voltage probe, f) current monitor, and g) electrodes glued on perspex with epoxy (yellow).

3.2 Mass Spectrometer

The mass spectrometer used was a quadrupole-based molecular beam mass spectrometer (MBMS), the HPR-60, manufactured by Hiden Analytical Ltd©. It consists of a three stage differentially pumped inlet system separated by aligned skimmer cones and turbomolecular pumps, and has been specifically designed for the chemical analysis of atmospheric-pressure plasmas. The pressure reduction stages (P1, P2, and P3), shown in figure 3.6, provide a pressure reduction from atmospheric pressure down to 10^{-1} Torr (P1), 10^{-5} Torr (P2), and 10^{-7} Torr (P3). The front cone orifice dimension can be modified, in this thesis a 100 μm has been used.

The HPR-60 can be used to detect neutral species (residual gas analyser (RGA) mode) as well as both positive and negative ions (secondary ion mass spectrometry (SIMS) mode). In RGA mode the neutral molecular beam is internally ionized before it reaches the quadrupole stage. In SIMS mode the molecular beam is already ionized and positive and negative ions are separated by applying voltages to the skimmer cones.

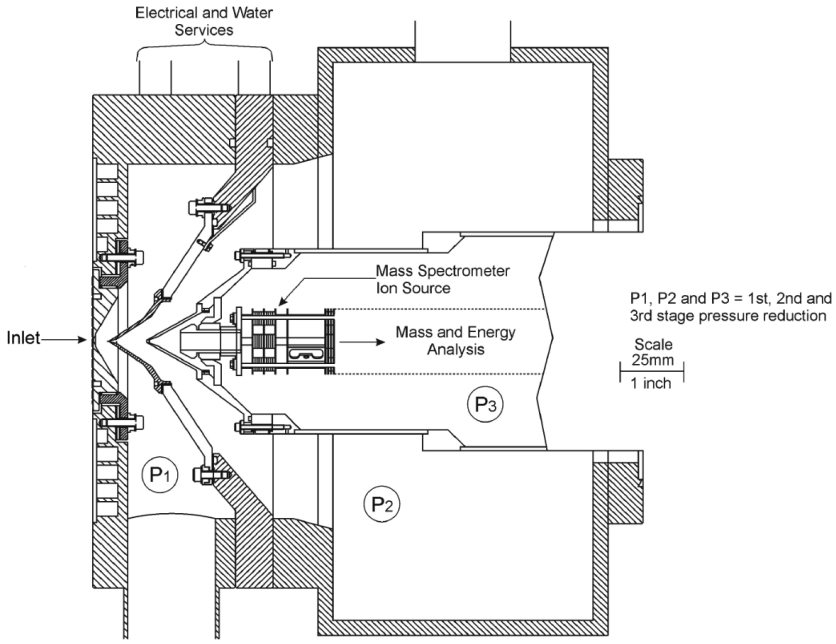

Figure 3.6: A cross section of the HPR-60 mass spectrometer. Image taken from the HPR-60 manual.

The mass spectrometer was calibrated using heptacosafluorotributylamin (Sigma-Aldrich) for heavy masses (671.09 Da) and atmospheric nitrogen for lower masses (28 Da).

As specified in [164], the measurements are influenced by the mass spectrometer transmission function which decreases with increasing of mass. No account of this dependency was taken in the report of the measurement in this thesis.

Positive and negative ions generated by the plasma jet were readily detected using the HPR-60 system. The plasma jet was aligned with the centre of the sampling orifice and the distance from the end of the capillary was fixed to 10 mm.

Positioning of the plasma jet was performed using a pure helium jet. The glass cylinder was moved until the plume was visually close to the front cone hole. Then using live readings of positive SIMS of nitrogen, water, helium, and protonoted monomer when fed into the plasma, the position of the jet was tuned until the readings of helium and the protonoted monomer were the highest, and the reading of nitrogen and water the lowest possible. The reason is that water and nitrogen ions, coming from the surrounding atmosphere, are generally situated on the outer part of the plasma plume, however, the helium (and monomer if added), are situated at the center of the plasma plume.

The mass spectrometer was operated in time-averaged and time-resolved mode (see section 4.1.2 for detailed explanations). When used in time-resolved mode, the mass spectrometer was connected to the signal generator (see sections 3.1.1 and 3.1.2) synchronising the driving voltage with the detector.

Before taking each measurement, a startup procedure was followed. First, a neutral scan of the background atmosphere was performed. This highlights any initial problem with the detector or with the orifice. Then a pure helium jet was used to centre the plasma plume exactly onto the spectrometer orifice as described above. Then 3 to 5 scans, called cycles in the Masoft software, were performed successively without changing any parameters. The data were averaged and plotted.

Within the mass spectrometer there is a significant transit time through the device for each ion; with heavier ions taking longer than lighter ions, for example, protonated acrylic acid with a mass of 73 Da needs $\sim 101\,\mu$s to transit from the mass spectrometer entrance to the detector whereas the protonated acrylic acid oligomer $[3M+H]^+$ (217 Da) needs $\sim 175\,\mu$s. To allow for correlation be-

tween the ions detected and the voltage and current waveforms the ions signal is temporally corrected using an algorithm developed by Hiden Analytical Ltd; this accounts for the transit times of different ions through the various parts of the mass spectrometer (appendix A.2 presents the calculation of the transit time).

Tunings of all the mass spectrometer parameters were performed at the beginning of the experiment. The values were tuned using a helium plasma jet with the default values chosen to be the values that Dr. Jun-Seok Oh used in a previous experiment [105]. Three main tunings were made, one for RGA mode, one for negative SIMS, and one for positive SIMS. Occasional tunings were performed to make sure the maximum signal was recorded. These tunings consist of reusing existing files and operating an auto-tuning using the Masoft software, which slightly adjust a few parameters (such as front cone or extractor voltage value). Tuned values were similar for time-averaged and time-resolved measurements. The only modification was the *gating* parameter which was enabled (1 instead of 0), which enable external gating of the readings, and the modification of *gate_width* and *foreground_delay* which control the duration of the readings and the delay between the gating and the reading respectively (see section 4.1.2 for more details). Typical values for the mass spectrometer parameters are listed in the appendix (see A.3).

3.3 Surface Analysis

X-ray photoelectron spectroscopy (XPS) and time-of-flight secondary ions mass spectrometry (TOF-SIMS) were performed by Sebastiaan van Nuffel. Both devices are installed in the Laboratory of Biophysics and Surface Analysis at the School of Pharmacy at the University of Nottingham.

3.3.1 X-ray Photoelectron Spectroscopy

XPS spectra were acquired on a Kratos Axis Ultra (Kratos) with a monochromated Al Kα source (1486.7 eV) using an emission current of 10 mA and an anode potential of 12 kV. Wide scans were acquired with a pass energy of 80 eV; high resolution scans of carbon 1s binding energy were acquired using a pass energy of 20 eV, for all the cases charge neutralisation was used.

Both an underivatised and a derivatised sample of each type were analysed. A wide scan and a high resolution C 1s scan of three different spots on each sample were acquired. The XPS spectra were analysed and fitted using CasaXPS software (version 2.3.16). The derivatisation process is described in details in chapter 4, section 4.2.1.

3.3.2 TOF-SIMS

The TOF-SIMS analyses were executed using a TOF-SIMS IV instrument (ION-TOF), equipped with a bismuth liquid metal ion gun (Bi LMIG). The primary ion beam is directed at the sample at an angle of 45° to the normal and has a beam spot of 1-2 μm in the high-current bunched mode. Throughout all measurements, 25 keV Bi_3^+ ions were used. Charging of the sample is compensated with the low-energetic electrons of the flood gun.

Ion images were recorded in the high current bunched mode, which allows for higher mass resolution. Stage scans with 150 pixels/mm and 15 frames per patch (1 shot per pixel) allowed large analysis zones. With a target current of 0.3 pA in AC mode, this resulted in an ion dose of 1.58×10^9 primary ions cm^2. The mass resolution was on average 2474 (FWHM) at an m/z ratio of 15.

The positive ion mass spectra were calibrated with an m/z of 1 (H^+), 15 (CH_3^+), 29 ($C_2H_5^+$), 43 ($C_3H_7^+$), and 57 ($C_4H_9^+$). The negative ion mass spectra were calibrated with an m/z of 1 (H^-), 12 (C^-), 13 (CH^-), 16 (O^-), and 17 (OH^-). Secondary ion images were then reconstructed from the raw data files. Data processing was performed with the commercial ION-TOF software (Surfacelab 6) and Matlab.

3.3.3 Ellipsometry

Ellipsometry measurements were conducted at the University of Liverpool with the help of Dr. Ian Brunell. Ellipsometry uses the properties of the reflection of a polarised light off a surface to analyse the refractive index of a material. It can also determine the thickness of a thin film deposited on a known material. The ellipsometer used is the model AutoEL IV (Rudolph Research) shown in figure 3.7. It is a single wavelength (0.6328 μm) null ellipsometer with a 70° angle of incidence. It was used to measure the thickness of Al_2O_3 films deposited on

silicone wafers.

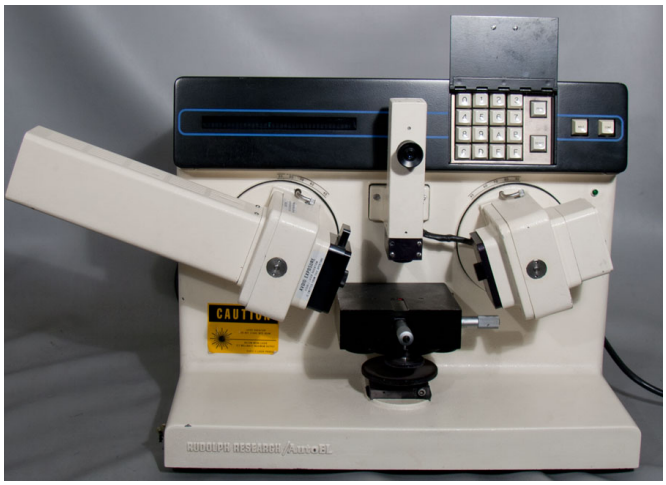

Figure 3.7: The AutoEL IV ellipsometer (Rudolph Research) used to measure deposition thickness of ALD and PEALD samples. Photo from [165]

3.3.4 Electrostatic Measurement

The contactless electrostatic probe is a 6000B-5C high-resolution probe with a voltmeter model 347 from TREK©. The substrate analysed was an acrylic sheet set on a metallic plate which was grounded to avoid external interference. The probe measures the potential of a surface with a precision of 1% and a spot area of 53 mm^2 for a 2 mm gap between the probe and the substrate (probe resolution is given in appendix A.4). More explanations on the probe and derivation of the charge are presented in section 4.2.2. An image of the probe system is shown in figure 3.8.

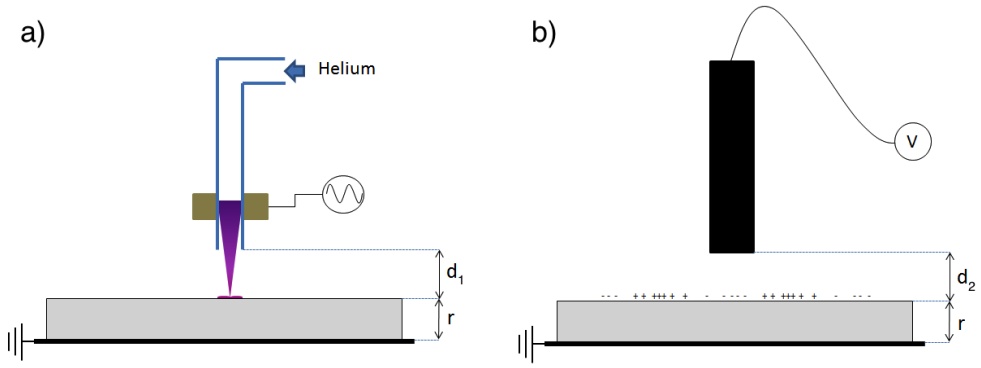

Figure 3.8: Schematic of the electrostatic apparatus with r = 5 mm, $d_1 = 50$ mm, and $d_2 = 2$ mm. Where a) shows the plasma jet on the acrylic sheet (grey), b) shows the electrostatic probe reading the charge density of the acrylic sheet (grey) at a certain distance.

3.4 ALD Instrument

The ALD reactor used in this thesis is the model Savannah from Ultratech (figure 3.9). It has a computer controlled box, a rotary pump, a cylindrical vacuum chamber, a heating system for the chamber, four fast ALD valves, and different gases connected to the valves. The software can modify the temperature of the chamber, switch the pump off or on, and control cycles of gas entering the chamber. To synchronise the plasma reactor to the ALD system, an output from the computer controlled box was fed to the gate input of the signal generator. To facilitate the plasma ignition, air was used as the reactant gas. Nitrogen in air ionised easily allowing the ionisation of oxygen contained in air. The pressure was 1 Torr and the temperature was fixed at 50 °C. The purge gas was argon and the aluminium precursor was trimethylaluminium (TMA) with the chemical symbol of $Al_2(CH_3)_6$ and is in a liquid state at atmospheric pressure between 15 °C and 125 °C, thus argon was bubbling through TMA to inject the aluminium compound in the reactor chamber. A typical cycle in terms of gas injection is displayed in figure 3.10.

Figure 3.9: The ALD reactor Savannah from Ultratech. Image taken from the Ultratech Cambridge NanoTech's website.

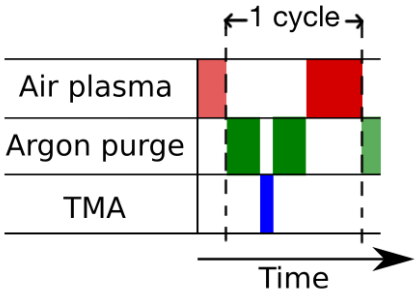

Figure 3.10: A typical ALD cycle through time.

3.4.1 PEALD Reactor

The ALD reactor was custom-built. It was made from a cuboid of acrylic. An inner disk was removed from both sides, leaving a thin round area 2 mm thick. A diagram of the reactor is shown in figure 3.11. The electrodes are made of aluminium tape, cut using a vinyl cutter. The electrodes are taped to each side of the inner circle carved in the acrylic. The volume above the driven electrode was filled with a silicone epoxy (RTV silicone SE2005) to avoid undesired discharges. The electrode on the bottom is connected to the ground and the other electrode to a high voltage signal. The plasma reactor is made to fit perfectly on the ALD reactor and sustain a decrease in pressure without damaging or leaking. When the reactor was heated to more than 100 °C, the thin acrylic area began to bend under the pressure gradient. The temperature was thus reduced to 50 °C.

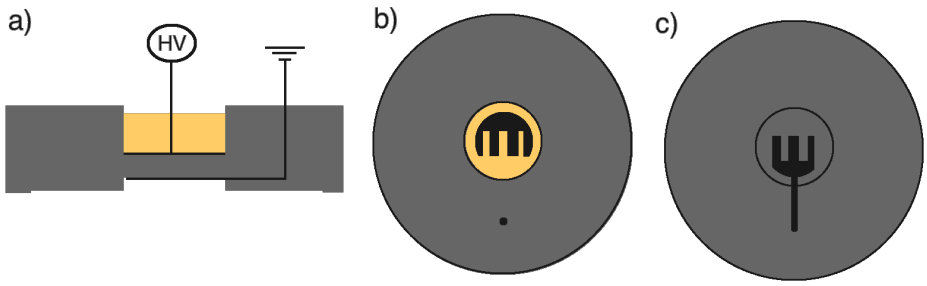

Figure 3.11: Schematic of the custom-build PE-ALD reactor: a) cross-section, b) top view, and c) bottom view. The grey part is made of acrylic, the orange part is an epoxy, and the black area is aluminium. The diameter of the reactor is 300 mm, the inner diameter of the disk containing the two aluminium electrodes is 60 mm.

Chapter 4

Methods and Descriptions of Analysis Techniques

This chapter describes and justifies the data gathering method used, it also details some analysis techniques. The previous chapter presented all the devices used in this thesis, this chapter complements it by giving information about routines and particular processes made on these devices. This chapter outlines electrical measurements gathered of the atmospheric-pressure plasma jet experiment (current, voltage, and power calculation), explains the different mass spectrometry measurement methods (time-averaged and time-resolved procedures), and describes precisely some surface analysis modus operandi (XPS derivatisation, High resolution C 1s scans, and electrostatic probe measurement).

4.1 Plasma Analysis

Here the analysis of the plasma will be explained.

4.1.1 Current, Voltage, and Power Measurements

Current and voltage

The current was measured using the current monitor. The sensitivity is $1\,\mathrm{V} \leftrightarrow 1\,\mathrm{A} \pm 1\%$, meaning that for each ampere detected, the probe output produced 1 volt. The probe was connected to an oscilloscope and the signal was saved using a floppy disc then load into Origin to plot and analyse. The voltage was measured by connecting a high voltage probe to the wire between the power supply and the

electrode. The probes used were either the Pintek HVP-15HF or the Tektronix P6015A, both have a reading of $1\,\mathrm{V} \leftrightarrow 1000\,\mathrm{V}$, meaning that for each thousand volts measured the probes produce 1 volt. The voltage signals were taken in the same manner as the current signals. The sample interval used by the oscilloscope was 2 ns with a precision of $1\,\mu\mathrm{V}$. The behaviour of the voltage, the current, and the power as a function of the plasmas parameters is explained in the next paragraph. An example of voltage and current of a positive pulsed DC signal is shown in figure 4.1.

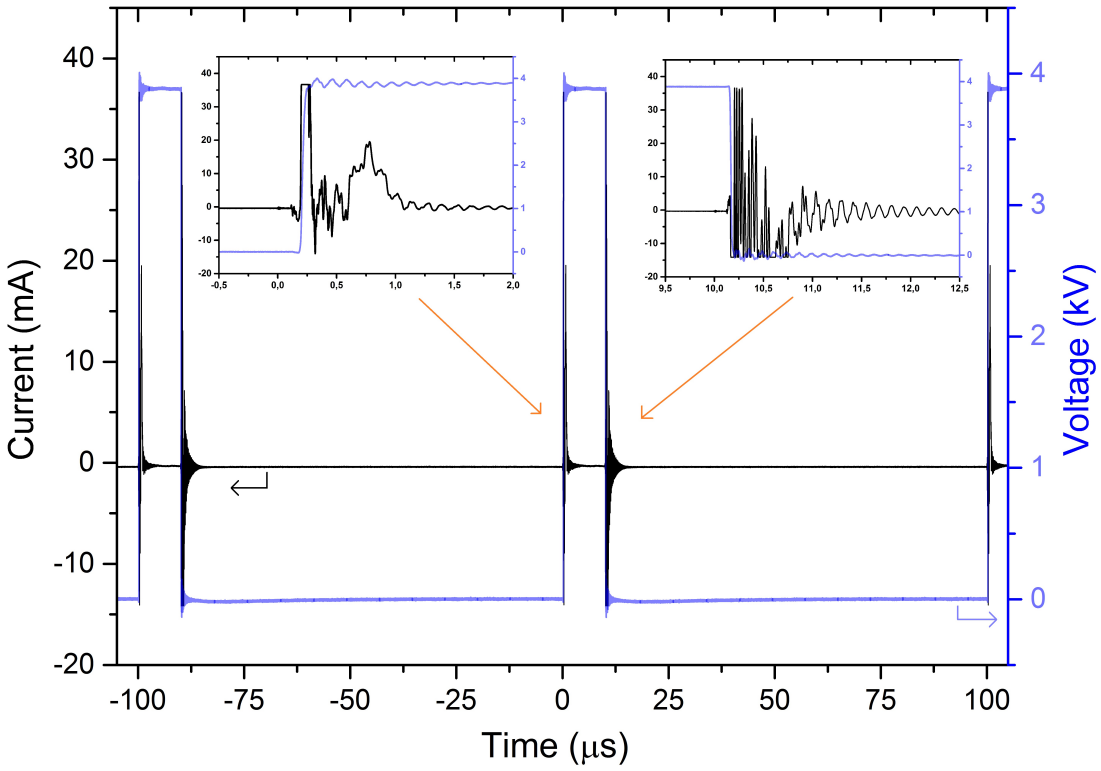

Figure 4.1: Current (black) and voltage (blue) of a 10 kHz, 10 % duty cycle at ∼4 kV of amplitude. The quick rise of voltage creates a high displacement current clearly seen at -100 μs and 0 μs, the oscilloscope peak is saturated in this figure, the peak value was ∼10 A. The quick drop of voltage creates an identical phenomenon with an opposite sign for the generated current. The positive bump visible at ∼0.8 μs corresponds to the plasma bullet current. A negative plasma bullet current is also recorded at ∼10.7 μs, however, it is hidden in the noise of the signal and is cut by the y-axis of the oscilloscope

Power measurement of Pulse DC

The high current signal at the rising and falling edge of the voltage in figure 4.1 is the displacement current given by the following equation:

$$I_{\text{disp}}(t) = \varepsilon \frac{d\Phi_{\text{E}}}{dt} \tag{4.1}$$

where I_{disp} is the displacement current, ε is the relative permittivity, and Φ_{E} the electric flux. The displacement current (I_{disp}) can be related to the so-called capacitor equation (4.2). In order to simplify things, the apparatus (electrode and front cone of mass spectrometer) can be assumed to correspond to a parallel plate capacitor with an area of A, thus $\Phi_E = A \cdot E$ where E is the electric field between the plates and with $E = V/L$ with L and V being the distance and the potential between the plates. Therefore equation (4.1) becomes,

$$I(t) = \varepsilon \frac{\mathrm{d}\,(A \cdot E)}{dt} = C \frac{dV(t)}{dt} \tag{4.2}$$

where $C = \varepsilon A/L$. The plasma bullet current can be seen on figure 4.1 at $\sim$0.8 μs visible on the higher magnification. A negative bullet current trace is also present, however, it is harder to detect on figure 4.1 due to a noisy current signal, furthermore, the oscilloscope y-axis signal was chosen to be between -15 and 40 mA slightly cutting the negative bullet current in this particular example.

The power is calculated using $P(t) = I(t) \cdot V(t)$ where current and voltage are recorded by the probes. Instant power is presented in figure 4.2 using the current and voltage from figure 4.1. As expected, the instant power is zero for most of the signal duration, the only non-zero values are at $100n\,\mu$s and $(100n + 10\,\mu\text{s})$ with $n \in \mathbb{Z}$. The power contributing to the plasma is the positive plasma bullet power which is the bump seen between 0.6 μs and 1.1 μs in figure 4.2, the negative bullets do not contribute to the power as it occurs when the voltage is zero. The average power is the integral of $I(t) \cdot V(t)$ over the period duration. To calculate the average power, first the energy of the plasma bullet (E_{bullet}) is estimated using the following formula:

$$E_{\text{bullet}} = \int_{t_{\text{start}}}^{t_{\text{end}}} (I(t) \cdot V(t))\mathrm{dt} \tag{4.3}$$

where t_{start} and t_{end} are the starting and the end time of the plasma bullet, respectively. Then using the fact that only the positive bullets contribute to

the plasma power the following equation has been used to evaluate the average plasma power (P_{avg}):

$$P_{\text{avg}} = \frac{1}{T}\int_{t_0}^{t_0+T}(I(t)\cdot V(t))\text{dt} = \frac{E_{\text{bullet}}}{T} \tag{4.4}$$

where T is the period. Thus P_{avg} is the power of the plasma jet averaged over the period. As the power is mostly zero over the period, $I(t)\cdot V(t)$ is integrated over a reduced the time step. In this way, integration of the noise is greatly reduced.

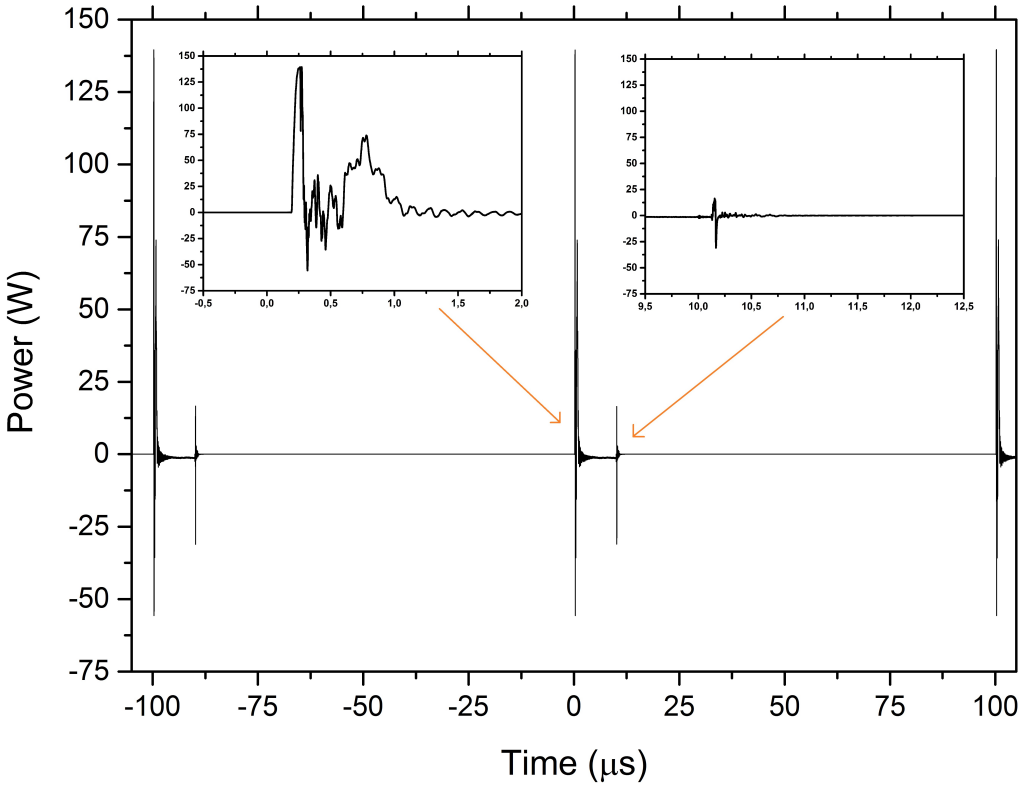

Figure 4.2: Power of a 10 kHz, 10 % duty cycle at ∼4 kV of amplitude. Power is calculated using current and voltage displayed on figure 4.1.

Power measurement of continuous wave

For continuous wave, the displacement current, as given by equation figure 4.2, is also sinusoidal. As in [80], plasma current can be observed after removing the displacement current (see figure 4.3). As opposed to the pulsed DC mode where

the variation in the voltage appears on a very short time scale, displacement currents of continuous wave in the range of 10 kHz, are very stable through time.

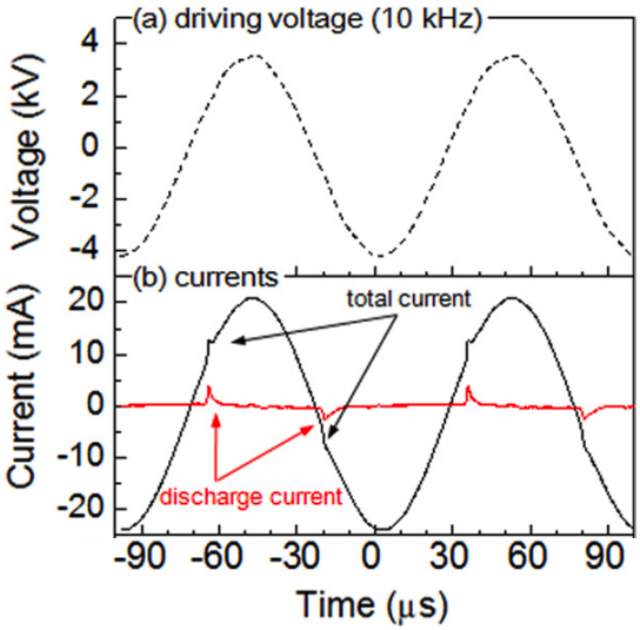

Figure 4.3: Plots of typical driving voltage (a) current signals, (b) total and discharge currents. In this case the driving frequency is 10 kHz. The currents have been intentionally delay by the authors to remove the 90 degree shift between current and voltage, taken from [80].

Power is measured similarly to the pulsed DC mode. By calculating the integral of $I(t) \cdot V(t)$ averaged over one period, P_{avg} can be achieved, given as:

$$\begin{aligned} P_{\text{avg}} &= \frac{1}{T}\int_{t_0}^{t_0+T} ((I(t) - I_{\text{disp}}(t)) \cdot V(t))\text{dt} \\ &= \frac{1}{T}\int_{t_0}^{t_0+T} (I_{\text{bullet}}(t) \cdot V(t))\text{dt} \end{aligned} \tag{4.5}$$

where $I_{\text{disp}}(t)$ can be measured by removing the helium and thus turning the plasma off whilst keeping the signal unchanged.

4.1.2 Time-Averaged and Time-Resolved Mass Spectrometry

Time-averaged measurements

The detector records the arrival of a specified mass for a certain period of time

called the dwell time. This parameter can be controlled by the user. For the present work it was kept fixed at 100 ms. This value is long enough to collect much more data than the background noise, and small enough to allow a scan to stay in the range of 1 to 10 minutes. The detector records the average number of counts per second. Most of the results shown are an average of two to four spectra taken successively.

The "increment" is the mass step for the collector scan. For fast scans, 1 Da was chosen and for precise scans like those presented in this thesis, the increment parameter was fixed at 0.1 or 0.2 Da.

It can be noted that for the time-resolved measurement, the mass spectrometer collects molecules of mass ± 0.5 Da of the specified mass.

Time-resolved measurements

Time-resolved measurements are averaged measurements taken only at a certain time of a period. To execute a time-resolved measurement, the mass spectrometer has to be connected with a periodic signal. Each time the external signal crosses a certain voltage, it triggers the spectrometer. The time between the trigger and the measurement is called the foreground delay and can be varied automatically. The duration of the measurement, called the gate width, is the time during which the collector is open. Figure 4.4 explains how the time-resolved measurements are processed. The gate width was set to 5 μs for most of the measurements made.

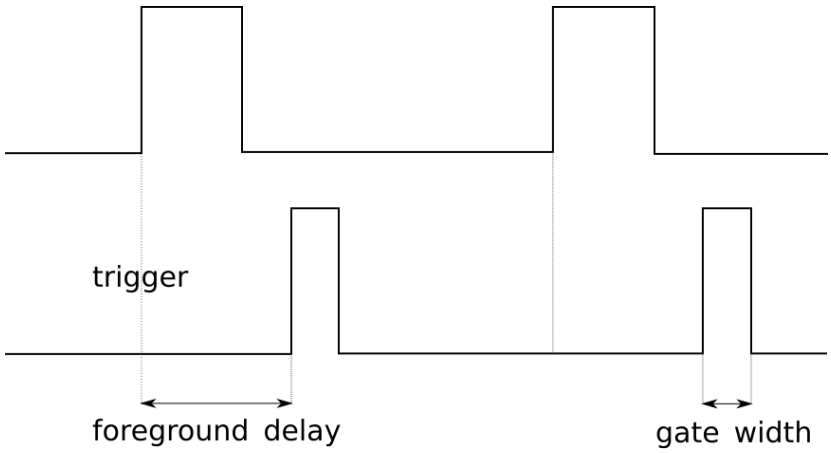

Figure 4.4: A diagram of the time-resolved process. The top line is the output of the signal generator, the bottom line is the signal given to the mass spectrometer detector. During a time-resolved measurement foreground delay is varied allowing a scan over the whole period.

For most of the results, the time resolution of the system, i.e. the duration of the foreground delay steps, was set to 3 μs. Higher resolution measurements (0.5 μs) were conducted and showed similar trends. Using the higher resolution, however, increased the measurement time significantly, leading to the mass spectrometer orifice becoming coated with polymer material decreasing the signal intensity during the measurement. Therefore 3 μs was chosen for most of the results shown in section 5.3 as it was sufficient to monitor changes in flux without compromising signal intensity.

The mass spectrometer in time-resolved mode takes several measurements of the same mass until the amount of time multiplied by the gate width is equal to the fixed collection time, the dwell time. For example, if the dwell time is fixed to 100 ms and the gate width to 5 μs, $100\times10^{-3} / 5\times10^{-6} = 20\,000$ periods are necessary to record one point of the spectrum data.

In the time-resolved measurements taken in this thesis, between two and four individual masses were chosen, and the foreground delay was varied for a duration of around one and a half periods.

4.2 Surface Analysis

4.2.1 X-Ray Photoelectron Spectroscopy

In some particular cases when a particular chemical bond cannot be distinguished by the XPS, a derivatisation process can be applied. This process consists of chemically modifying every specific chemical bond of the bulk into another molecule easily distinguishable by an XPS scan. The derivatisation of the carboxyl group contained in the acrylic acid is explained in this section. Furthermore, the methods used for the high resolution C 1s scans are explained.

Derivatisation

A derivatisation of the carboxyl groups (-COOH) was necessary to be able to discern the group among other carbon group (-COOR) where R represent any atoms or molecules but hydrogen. In order to assess the degree of esterification of the carboxyl groups[1], the samples underwent esterification[2] with 2,2,2-

[1] ratio of ester group (-COOR) over carboxyl group (-COOH).

[2] chemical reaction in which 2 reactants form an ester as a product.

trifluoroethanol as described in [166]. This derivatisation technique consists of selectively modifying the carboxyl group (-COOH) into a new compound, -$COOCH_2CF_3$. To do so, the samples were placed in a glass tube on a microscope slide. Using a micropipette, 0.9 ml of 2,2,2-trifluoroethanol was added underneath the microscope slide; the tube was sealed with a stopper wrapped in PTFE tape. After 15 minutes, 0.4 ml of pyridine (C_5H_5N) was added. After another 15 minutes, 0.3 ml of N,N-di-*tert*-butylcarbodiimide (^{t}Bu-NCN-^{t}Bu) was added. The reaction (see equation (4.6) and figure 4.5) proceeded overnight at room temperature. The samples were subsequently stored in a desiccator.

$$\mathrm{RCOOH} + \mathrm{CF_3CH_2OH} \xrightarrow[\mathrm{C_5H_5N}]{^t\mathrm{Bu\text{-}NCN\text{-}}^t\mathrm{Bu}} \mathrm{RCOOCH_2CF_3} \tag{4.6}$$

The derivatisation reaction is reported to be near stoichiometric ($87 \pm 15\%$) [167]. This error needs to be take into consideration when analysing the XPS results.

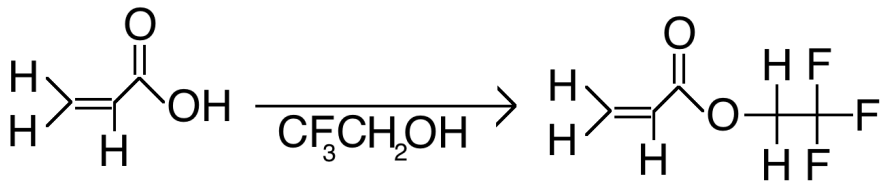

Figure 4.5: The derivatisation process: on the left-hand side is the underivatised acrylic acid and on the right-hand side the derivatised acrylic acid (C = carbon, H = hydrogen, O = oxygen, and F = fluorine).

High resolution C 1s scans

The high resolution scan of the C 1s signal allows peak fitting to be performed. Based on the structure of (non-plasma) poly(acrylic) acid, a fitting scheme was applied at first. The fitting was using three different carbon binding energies contained in acrylic acid: the so-called "aliphatic carbon" (-**C**-H/C), the "carboxylic carbon" (**C**OOH), and the "carboxyl induced beta-shifted carbon" (**C**COO) as shown in figure 4.6. The respective binding energies are: 285 eV, 285+(0.4-0.7) eV, and 285+(3.64-4.33) eV.

However, in the XPS results, this three-peak fitting scheme did not generate a good fit so more peaks needed to be added. This implied that the deposited acrylic acid suffered modification. The same peaks are used for the derivatised samples, but a sixth CF_3 peak (+ 7.65-7.72 eV) is added to the scheme.

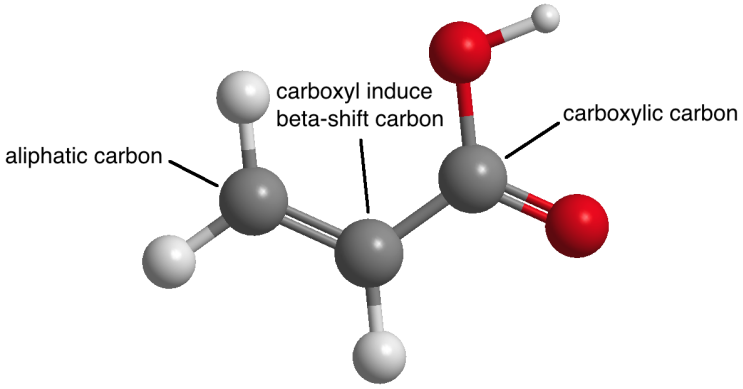

Figure 4.6: Acrylic acid molecule with the names of its three carbons.

Because almost all the carboxylic acids are in principle trifluoroethanol esterificated, the ratio of the CF_3 peak and the COO peak reflects the percentage of the carboxyl functionalities that are present as acids, i.e. [COOH]/[COOR]. It is then possible to calculate the percentage of carbon present as carboxylic acids [COOH] in the underivatised samples by multiplying the percentage of the COO peak, i.e. [COO], with the average [COOH]/[COOR] for that sample type.

As an example, pure acrylic acid can be taken, table 4.1 shows the different concentration and ratios. To simplify the notation concentrations of derivatised and underivatised acrylic acid are subscripted with "der" and "under", respectively. The ratio $[CF_3]_{der}$ / $[COO]_{der}$ is 100%, corresponding to the ratio of the COO being COOH. Then ($[CF_3]_{der}$ / $[COO]_{der}$)·$[COO]_{under}$ = 33% which corresponds to the concentration of COOH in the underivatised compound. Thus the concentration of carboxylic group in the compound over the theoretical value for pure poly(acrylic) acid (33%) is called the retention.

Concentration	Underivatised acrylic acid (%)	Derivatised acrylic acid (%)
[COO]	33.3	20
[CCOO]	33.3	20
[C-H/C]	33.3	20
[CO]	0	20
$[CF_3]$	0	20

Table 4.1: Concentration of the different carbons in underivatised and derivatised acrylic acid.

4.2.2 Electrostatic Probe

The electrostatic voltmeter was clamped on a $x - y - z$ stage, it detects charges on a surface situated on a certain area A. The area detected by the electrostatic probe model 347 is dependant on the distance between the tip of the probe and the surface (see appendix A.4 for the probe resolution). The probe was positioned at $\sim$2 mm from the surface which give an area of detection of $\sim$53 mm^2 with an error of 1% according to the manufacturer.

Charge calculation

The charge density ρ on a surface is calculated using the parallel-plate capacitor formula:

$$V = \frac{\rho d}{\varepsilon} \Rightarrow \rho = \frac{\varepsilon_r \varepsilon_0 V}{d} \tag{4.7}$$

where V is the voltage at the surface, d the substrate thickness, and $\varepsilon_r\varepsilon_0$ is the permittivity of the dielectric (here an acrylic sheet). The voltmeter is using a Kelvin vibrating capacitive sensor as the detecting element. This sensor is oscillating which allows the measurement of a current at different distance from the surface. Knowing the vibration of the sensor (speed and amplitude), the difference of the potential between the sensor and the surface can be measured precisely[3]. The voltmeter has an electrode at the tip which replicates the voltage of the surface using the sensor measurement. If the sensor would remain stationary it will thus measure nothing as the electrode will nullify the electric field of the surface. As the sensor oscillates, it can measure the difference of the potential between its previous position and thus measure the surface potential independently of the distance between the voltmeter and the surface [168].

Using the data on the area of detection given by the manufacturer, the charge density can be estimated. The charge density is either given in coulombs per square metre [C m^{-2}] or in nanocoulombs per square centimetre [nC cm^{-2}] with the relation being

$$1 \text{ nC cm}^{-2} = 10^{-5} \text{ C m}^{-2}$$

[3]The permittivity of the material between the surface and the probe is assumed to be that of air.

Chapter 5

Analysis of the Spectrometry of the Plasma Polymerisation

5.1 Overview

Mass spectrometry of plasma polymerisation has been already performed by several research groups [105, 109, 110, 121, 123, 124, 169–173]. Most of these studies analysed polymerisation processes using low-pressure plasmas.

In the literature, time-averaged mass spectra are more common than time-resolved measurements. Whittle *et al.* in [100] and [87] presented and compared time-averaged mass spectra of acrylic acid performed in different laboratories using low-pressure plasmas. These references are useful to compare the results presented in this chapter.

Plasma polymerisation, performed at low pressures differs from polymerisation performed under atmospheric pressure as is the case in this thesis. First of all, as described in section 2.2.2, collisions are more frequent in atmospheric plasma discharges than in low-pressure plasmas due to the reduced mean free path, resulting in a reduced ion energy distribution. Hence the lower amount of energy per ions reduces the fragmentation of the monomers and polymers present in the plasma. On the other hand, the lower energy of the ions also decreases the probability of polymerisation. Low-pressure plasmas have ionisation degree much higher than atmospheric-pressure plasma jets. As seen in section 2.3.2, ions and radicals are activated species necessary for a step-growth polymerisation. Results presented in this chapter show heavy protonated polymers for both heptylamine

and acrylic acid thus proving that the drawback of reducing polymerisation is overcome by the decrease of fragmentation. Another difference between low- and atmospheric-pressure plasma polymerisation is the control over the gas composition. Low-pressure plasma processes are operated in vacuum vessels allowing a very precise control over the gas composition and a low content of contamination species ($\sim$1 ppm for H_2O and Ar, $\sim$1 ppb for O_2) [174]. Whereas for atmospheric-pressure plasmas, often performed in air and rarely in a vacuum-tight environment, have many species present.

The gas composition is relatively well defined in the glass tube, hence also at the beginning of the plasma plume (setup described in chapter 3). However, as soon as the plasma plume is located outside the glass cylinder, the species contained in the surrounding atmosphere take part in the plasma reaction in a multitude of ways. Therefore, ionised elements and molecules of large number of different masses are present in the time-averaged mass spectra displayed in section 5.2.4. In the mass range below 50 Da, ionised water, nitrogen, and carbon dioxide among others are detected. High amounts of large ions which are not pure protonated polymers are also detected. They are either composed of a combination of polymers and another molecule, or fragmented oligomers (having lost a molecule of H_2O or OH).

This effect can also be visible for the low-pressure plasma, however, the higher possibility of combination due to the higher diversity of molecules available in the atmospheric case, greatly increases the creation of these heavy ions. As seen in [171], when plasma polymerisation is used it appears that positive ions and - often neglected - negative ions have an important role to play. Therefore most of the results shown in this chapter are mass spectra of ions (RGA spectra which are the neutral mass spectrometer readings can be found in the appendix A.5).

Results in this chapter show the production of heavy oligomers of heptylamine and acrylic acid using atmospheric-pressure plasma jets driven by either a continuous wave or a positive pulsed DC signal with helium as carrier gas. This production is accompanied by a high amount of heavy mass by-products which are comparatively more present than in low-pressure plasma polymerisation. These by-products are produced by the reactions occurring between plasma particles and ambient air molecules.

Time-resolved measurements were performed for acrylic acid polymerisation

using pulsed DC in order to understand better the polymerisation process as well as to analyse the effect of varying the duty cycle.

5.2 Time-Averaged Spectrometry

5.2.1 Introduction

In the literature, most of the analyses published for plasma polymerisation focus on the analysis of the film produced, by either bulk or surface measurements [30, 102, 103, 106, 115, 115, 119, 120, 126, 175–182]. Amorosi *et al.* point out that properties of the deposited thin film do not only depend on the composition of the coating but also on the morphology and the degree of polymerisation in [104]. They predicated that the oligomerisation state of the deposited polymers are very important in the long term stability of the film. Ionised polymers, both negative and positive, play a role in the retention of functional groups in plasma polymerisation according to [171].

Only a few number of papers have used Fourier transform infrared spectroscopy (FTIR) or optical emission spectroscopy (OES) to investigate directly the plasma [103,183–185] . These techniques are able to record the general composition in terms of atoms, excited electronic states, or chemical bonds of a molecule, however, they cannot directly detect the presence of complex molecules [186,187]. Mass spectrometers are used for such purposes (see section 3.2).

Mass spectrometers work under vacuum and spectrometers able to measure atmospheric-pressure plasmas is a recent technology. These instruments are still limited, for example the HPR-60 used in this thesis cannot record ions from an atmospheric-pressure surface discharge and has difficulty detecting atmospheric-pressure volume discharges (i.e. has a low count per second). Jet plasma ions, however, can be easily detected as long as its plume is aimed directly on the mass spectrometer orifice. The issue lies in encouraging the ions to travel from the plasma into the orifice of the mass spectrometer, this is why jets work easily and surface discharges present difficulties.

As just mentioned, the mass spectrometry of polymerisation plasma has been performed by D. Barton *et al.* or I. Swindells *et al.* for low-pressure plasmas [123,171]. J-S. Oh, using the same mass spectrometer as the work presented here, was the first to publish a scientific article on mass spectrometry of polymerisation

of heptylamine produced by a plasma jet in [105]. Acrylic acid has been more studied in this thesis due to this previous work realised by J-S. Oh on heptylamine.

As Voronin *et al.* describe, it appears that pulsed plasmas are more efficient at producing polymers than plasmas created by a continuous signal. According to this study, monomers are ionised during the on-time and polymerisation occurs in the on-time and the off-time. To confirm this assumption and to compare it to work at higher pressures, a pulsed DC signal has been used [110].

Parameters such as voltage, frequency, duty-cycle, and type of signal (continuous or pulsed) were modified to analyse and understand polymerisation of a simple monomer using atmospheric-pressure plasma jet.

J-S. Oh has performed a similar experiment using heptylamine and a y-shaped glass tube [105]. Detection was made of $[n\mathrm{M}+\mathrm{H}]^+$ with $n = 1, 2, 3 \ldots$ up to 6 and relative yield of polymer as shown in table 5.1 using a resolution of 1 Da. The information given in the table is coming from a figure in [105]. The first row gives the relative yield which is the intensity of a particular m/z over the total intensity. The second row summarises the intensity ratios of monomer and polymers positive ions over the monomer intensity. It will be of interest to compare the relative yields of acrylic acid found in the present study to the values found by J-S Oh.

$[n\mathrm{M}+\mathrm{H}]^+$ with $n =$	1	2	3	4	5	6
Relative yield (%)	2.4	1	0.5	0.9	0.4	0.1
Percentage of monomer value	100	41.7	20.8	37.5	16.7	4.2

Table 5.1: The relative yield and percentage of monomer value of heptylamine using a y-shaped glass tube. Values reproduced from [105].

5.2.2 Experimental Setup

The equipment involves a quartz tube with 2 mm internal diameter, and 4 mm external diameter with a copper ring around it. Helium gas at atmospheric pressure is injected into the glass tube. In every experiment, 1 % of the helium flow (14.6 sccm) was bubbling through pure liquid monomer and added to the main flow (1500 sccm) in the acrylic acid experiments. When the copper electrode is driven by a sufficient voltage a plasma discharge occurs (see section 3.1 for more descriptions and a diagram of the apparatus). When the jet has not been used for several tens of minutes it needs a higher voltage to be ignited due to the lack

of electrostatic charges deposited on the inside of the glass tube. To avoid damaging the system by applying too high a voltage, a grounded cable connected to a metallic bulk, typically a copper wire attached to a screwdriver, was moved close to the tube nozzle which increases the electrical field between the electrode and the cable. This results in either a spark or a high density plasma which creates a sufficient number of ionised particles and electrons, to therefore sustain a stable plasma when the cable is withdrawn.

Electrical signals were driven with either a continuous wave (see section 3.1.1) or a positive pulsed DC signal (see section 3.1.2). The pulsed signal enables one degree of freedom more than the continuous one, the variation of the duty cycle whilst keeping the frequency constant. As seen in section 4.1.1, the modification of duty cycle should not modify the power delivered to the electrode. However, due to imperfections in the custom-built power supply (see section 3.1.2), the potential applied for a given value displayed on the high voltage box varies slightly with the duty cycle as is shown in appendix A.6.

The mass spectrometer used was the HPR-60, manufactured by Hiden Analytical Ltd, it is described in details in section 3.2. The orifice size of the front cone was 100 μm. The distance between the jet and the front of the mass spectrometer was 10 mm and the arrangement as shown in section 3.1 was used.

Reliability of the measurements

As the orifice in the front cone of the mass spectrometer has a diameter of 100 μm any slight change in the position of the jet may affect the measurement. It has been seen that when the glass tube has been replaced and positioned to what seemed to be the exact same position according to the micrometre screws, the measurements differed slightly. The temperature in the laboratory also varied with time during the day and, of course, from one day to another, this change modified the amount of monomer in the gas mixture as the enthalpy of vaporisation is highly sensitive to the temperature around room temperature. The humidity in the atmosphere was also changing with time, and with it, increasing or decreasing the amount of water in the ambient air. To minimise these effects most of the data presented in this chapter were performed with measurements made one after the other, where no modification of the jet position was made, and the temperature and humidity were more or less constant.

Another effect which could unfortunately not be removed was the coating of both the internal surface of the glass tube and the front face of the cone. The mass spectrometer cone was cleaned using a tissue soaked with isopropanol after each measurement. However the glass tube was replaced or cleaned only after a couple of measurement to avoid modification of its position. This coating is made of monomers, polymers, and other species present in the plasma and are etched by the plasma, slightly affecting the amount of ions and neutrals detected by the mass spectrometer. The coating on the cone can slightly decrease the diameter of the orifice decreasing the total amount of species going into the mass spectrometer. The front cone was regularly cleaned in a isopropanol sonic bath followed by an ethanol sonic bath and then dried by high-pressure nitrogen.

5.2.3 Preliminary Results

Starting with acrylic acid, parameters such as frequency, voltage and flow of monomer were varied to find the optimal conditions of polymerisation.

When the frequency is modified, the average plasma power varies as $P_{\text{avg}} = E_{\text{bullet}}/T$ (eq. 4.4), where E_{bullet} is the energy of the plasma bullet and T the period (see section 4.1.1). As the frequency for a continuous wave signal is varied, so to does E_{bullet} which should, however, be independent of the frequency for the positive pulsed DC signal. Furthermore, alteration of the frequency changes the time in which polymerisation can occur. Each stage of the step-growth polymerisation requires a certain amount of time. Ref. [110] and [124] implied that polymerisation is very dependant of the duty cycle and that polymerisation occurs also in the off-time; increasing the frequency whilst keeping the duty cycle fixed increases the duration of the off-time, the time between the plasma bullets also rises. Section 5.3 shows that this phenomena is similar for polymerisation using APPJs. One explanation may be that plasma bullets fragment heavy polymers and their less energetic plasma trails allow the process of step-growth polymerisation to occur. If this is the case, a high frequency signal would greatly reduce the amount of heavy ionised oligomers while leaving the quantity of lighter ionised molecules such as helium, water, and nitrogen, constant.

Figure 5.1 shows the intensity of $N_2{}^+$, protonoted monomer, and polymer ions of acrylic acid as a function of the frequency for a continuous wave signal. It can be seen that at higher frequencies the amount of heavy polymer ions

decreases without changing the intensity of nitrogen ions. For frequencies lower than 10 kHz, P_{avg} may be not high enough to ionise enough monomer molecules. Frequencies under 5.5 kHz could not sustain a plasma with the apparatus used. At frequencies of 15 kHz or even 10 kHz, a higher amount of $[M+H]^+$ and $[2M+H]^+$ seemed to be produced, however, heavy oligomers production is lower than for 10 kHz. Therefore, 10 kHz was chosen for the rest of the measurements.

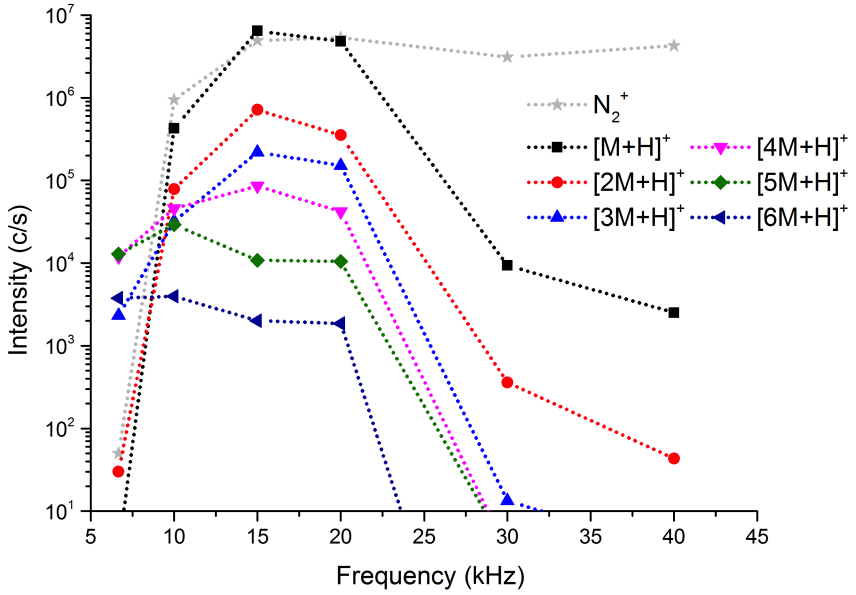

Figure 5.1: Intensity of positive ions of $N_2{}^+$, $[nM+H]^+$ with n from 1 to 6, for acrylic acid as a function of the frequency. The voltage was fixed to 5.5 kV and the flow of monomers was 8 sccm.

Next, the flow of helium going through liquid acrylic acid was varied and the effects were recorded. Figure 5.2 displays the intensity of $N_2{}^+$, protonoted monomer and polymer ions of acrylic acid as a function of the inverse of the monomer flow (1/sccm). The x-axis has been chosen to be linearly proportional to the Yasuda parameter (Y) (see section 2.3.1) as the power was kept constant in figure 5.2. It can be observed that as the flow increases (hence 1/flow decreases) the total plasma intensity drops as the power per molecule decreases until it is no longer high enough to sustain a plasma. The most plausible explanation is that the high amount of monomer increases the amount of collisions between the electrons and the complex molecules. Normally collisions between an atom (for

example helium) and an electron result in either an elastic collision, where the electron energy is barely modified, or ionisation of the atom. One the other hand, the monomer molecules have various excitation levels, thus most of the collisions will reduce the energy of the electron. Hence a high ratio of monomer in the total gas flow decreases the electron energy distribution leading to a reduction of particle ionisation.

For the highest monomer flow one can see in figure 5.2 that the oligomer ions have a higher intensity than the monomer and nitrogen ions. This is due to the plume length: for high monomer flow, and also for a low frequency (see figure 5.1), the plasma plume length is smaller. With the experimental setup used, the plasma plume barely reaches the mass spectrometer front cone orifice. The end of atmospheric-pressure plasma jet plumes is a spatial afterglow. Afterglow plasma composition can be significantly different from the composition in the middle of a plasma plume. This difference is probably the cause of the sharp decrease of nitrogen and monomer ions intensity for low frequency and low monomer flow in figure 5.1 and 5.2.

The monomer flow was chosen to be 8 sccm. A better choice would seem to be 9 sccm due to the higher heavy oligomer production as seen on figure 5.2, however, 8 sccm has proved to be more reproducible, probably due to the production of a more stable plasma.

Finally the voltage was modified slightly around 5 kV. The effect of its variation is presented in figure 5.3. As seen in section 4.1.1, the plasma power is linearly the Yasuda parameter. In figure 5.3, the intensities can be seen for positive ions of $N_2{}^+$ and $[n\mathrm{M}+\mathrm{H}]^+$ with n from 1 to 6, for acrylic acid for voltages between 4.6 and 5.5 kV with a fixed frequency and flow. Unfortunately, the intensity values for the 5.75 kV are not available due to technical problems, however, similar measurements (not displayed here) have shown that for a high voltage, the intensity of heavy ions decreased whilst the intensity of nitrogen ions stays constant. As flow is kept constant in figure 5.3, the intensity is proportional to the Yasuda parameter. It can be noted that the variation of voltage affects the plasma plume width which can thus be the cause of the changes seen in figure 5.3. Small variations of the voltage does not greatly affect the amount of heavy oligomers, 5 kV was therefore chosen for the future measurements.

Fixing the frequency, flow, and voltage, as described above for acrylic acid

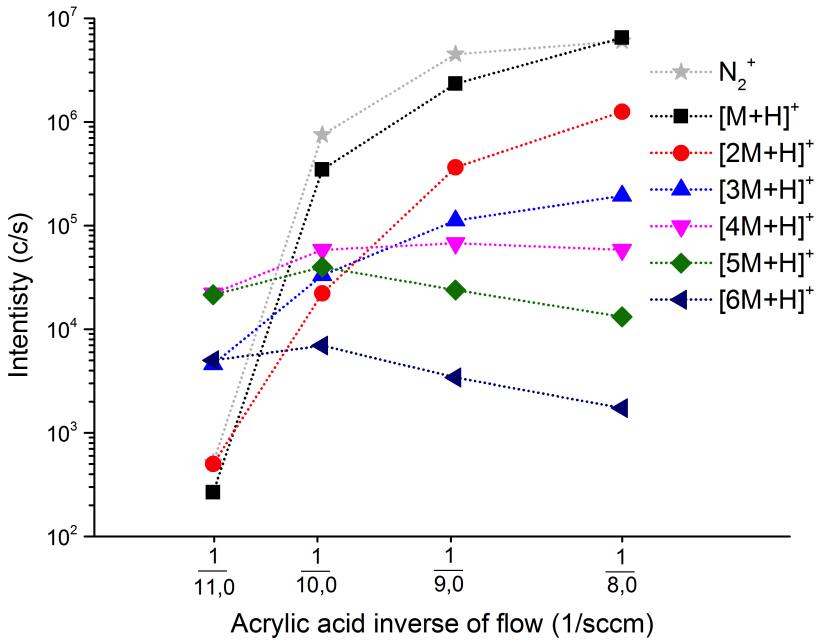

Figure 5.2: Intensity of positive ions of $N_2{}^+$ and $[n\mathrm{M} + \mathrm{H}]^+$ with n from 1 to 6, for acrylic acid as a function of the inverse of the monomer flow. The voltage was fixed to 5 kV and the frequency was 10 kHz.

using the continuous wave signal, a similar procedure was performed for heptylamine to find the optimum parameters which are reported in table 5.2. Then time-averaged mass spectra of acrylic acid and heptylamine were performed and the results are shown in the next section.

Monomer used	Frequency [kHz]	Helium flow bubbling through the monomer [sccm]	Helium flow [sccm]	Voltage [kV]
heptylamine	10	50	0.6	7
acrylic acid	10	8	940	5

Table 5.2: A list of parameters fixed for the heptylamine and acrylic acid studies using continuous wave plasma jets.

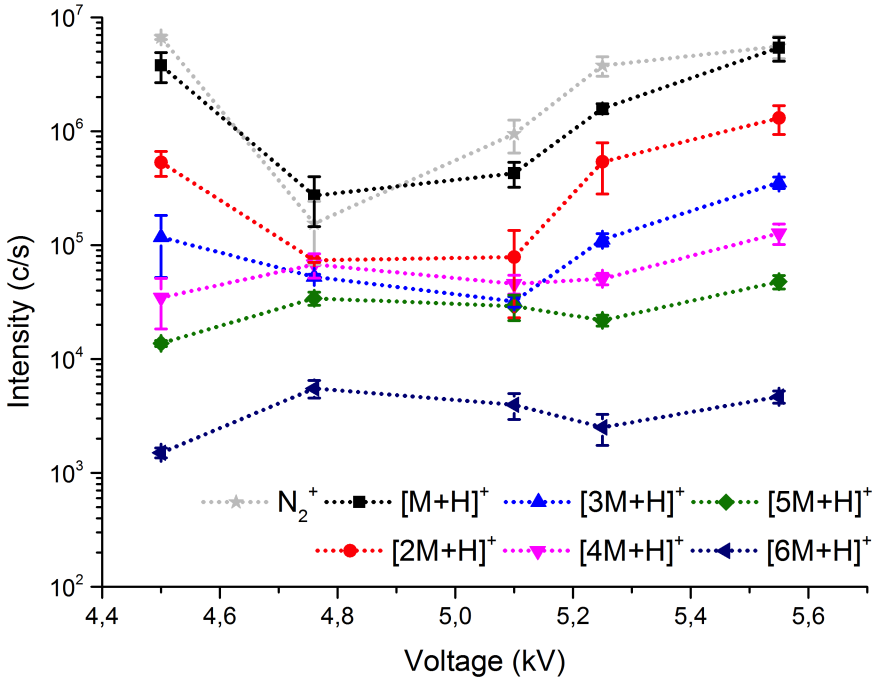

Figure 5.3: Intensity of positive ions of $N_2{}^+$ and [nM + H]$^+$ with n from 1 to 6, for acrylic acid as function of the voltage. The frequency was fixed to 10 kHz and the flow of monomers was 8 sccm.

5.2.4 Results and Discussion

After finding the optimal parameters for the polymerisation of acrylic acid and heptylamine, time-averaged mass spectra were performed. The results are shown in figure 5.5 and 5.4 respectively.

Figure 5.4 is very similar to figure 2 in [105] and will thus not be precisely described here to avoid repetition.The figure shows the detection of atoms and molecules contained in the air (low m/z ratio), fragments of monomer, monomer, oligomers, and molecules resulting of a combination of oligomers and air molecules.

The same species were found and table 5.3 shows similar ratio between oligomer and monomer intensity for the [3M+H]$^+$ and [4M+H]$^+$. The results in [105] have a better ratio of polymer over monomer for the other positive ions detected. Similar results could be obtained with a finer tuning of our apparatus. Due to time constrain this research is more focus one acrylic acid in order to perform an original study and to avoid repeating results found in a published paper.

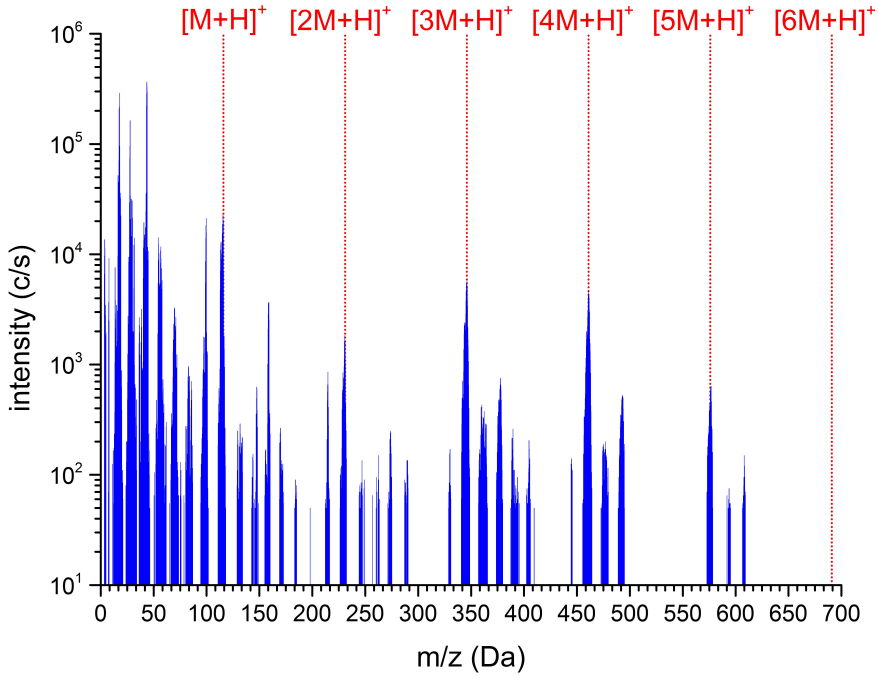

Figure 5.4: Positive time-averaged ion spectra for heptylamine. The frequency was fixed to 10 kHz, the voltage was 7 kV

Source	$[n\mathrm{M}+\mathrm{H}]^+$ with $n=$	1	2	3	4	5	6
Fig. 5.4	Relative yield [%]	0.7	0.16	0.03	0.07	0.02	0
Fig. 5.4	Percentage of monomer value	100	8	24	20.4	2.8	0
Ref. [105]	Relative yield (%)	2.4	1	0.5	0.9	0.4	0.1
Ref. [105]	Percentage of monomer value	100	41.7	20.8	37.5	16.7	4.2

Table 5.3: The relative yield and percentage of monomer value of heptylamine.

In figure 5.5 several positive oligomer ions ($[n\mathrm{M}+\mathrm{H}]^+$, where n=1-6) of acrylic acid were detected in the range 0-450 Da. In addition to the positive acrylic acid oligomer series, several other positive acrylic acid fragments and oligomers plus NH_4, CNH_4, CH_5O_2, C_3H_3O, and $C_2H_4O_2$ attachments were also detected (figure A.4 represents a few possible examples of by-products). These additional ions are produced through fragmentation and interaction with the open air. Sections 2.3.1 and 2.3.2 describe the possible paths of polymerisation growth. For example TOF-SIMS has detected NH_4 of a deposited film (see the result in section 6.4) and it is therefore a possible match for combination with the oligomers. Giorda-

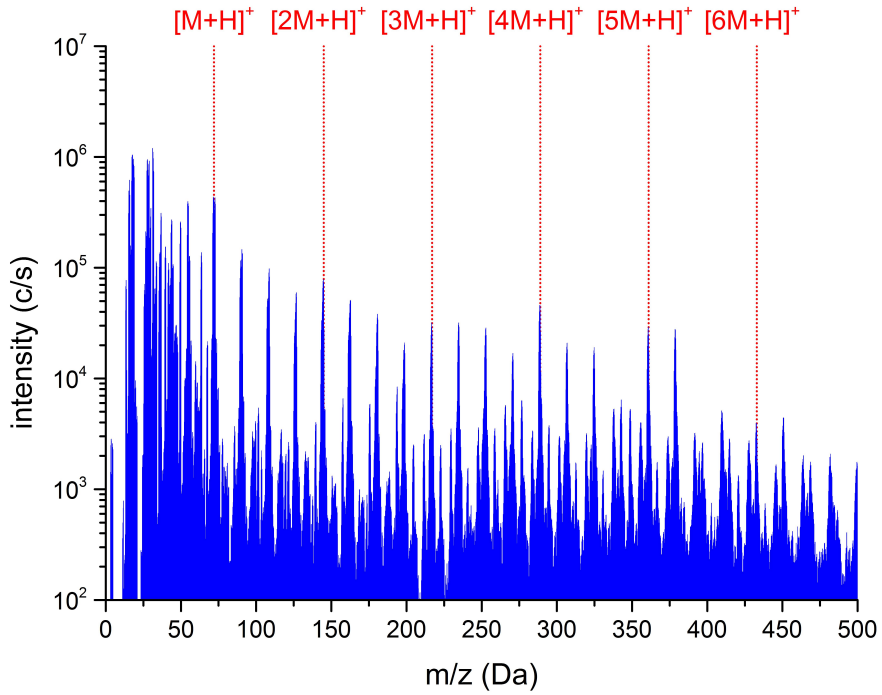

Figure 5.5: Positive time-averaged ion spectra for acrylic acid. The frequency was fixed to 10 kHz, the voltage was 5 kV, and the flow of monomers was 8 sccm.

nengo *et al.* describes that H_2O, among others, is commonly disassociated from poly(acrylic) acid molecules [188]. Figure 5.6 shows the process of the water loss, two H_2O molecules could also be lost for oligomers bigger or equal to [4M].

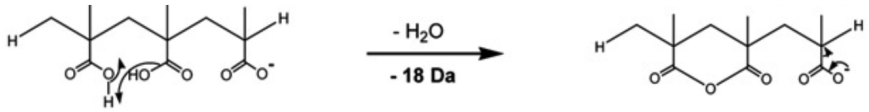

Figure 5.6: A diagram of water loss for poly(acrylic) acid, taken from [188].

Other molecules having the corresponding mass, chemistry, and composition have been found for most of the peaks present in figure 5.7, they are written in the legend of the figure. They are hence not guaranteed to be the real composition of the peak, they are only the best interpretations possible.

Frequency, voltage, and flow for positive pulsed DC signal were selected after a parameters optimisation was performed, as was done for the continuous wave case. Optimal flow was found to be 8 sccm of helium bubbling through liquid acrylic acid, and 1500 sccm of pure helium. Voltage input was put to 4.2 kV on the power

supply power supply dial which correspond to 3.85 kV fed to the electrode due to losses. Higher voltage may have produced better polymerisation, however, it could have damaged the power supply, thus 4.2 kV was chosen. Frequency did not vary substantially the result so two frequencies were chosen: 10 kHz, to keep the parameters similar to the continuous wave, and 5 kHz as it doubles the off-time for a similar duty cycle. It is important to repeat that changing the frequency for the pulsed DC signal does not vary the displacement current as explained in section 4.1.1 and therefore does not modify E_{bullet} either. Although E_{bullet} is independent of the frequency, P_{avg} is linearly proportional to the frequency as seen in equation 4.4.

Figure 5.7 shows the time-averaged positive and negative ion spectra obtained for the 5 kHz and 10 kHz pulses with a fixed duty cycle of 10 %. From figure 5.7a and 5.7b it can be seen that for both frequencies several positive oligomer ions ($[n\text{M} + \text{H}]^+$, where n=1-6) of acrylic acid were detected in the range 0-450 Da. The positive ions spectra in figure 5.7 display similar peaks to figure 5.5, and is already described above.

To determine the effect of pulse modulation on the production of the positive and negative oligomer series ($[n\text{M} \pm \text{H}]^{\pm}$) the duty cycle was varied from 10 % to 90 %. It was seen that a change in the duty cycle results in a change of the average power in the discharge due to imperfections in the power supply as seen in appendix A.6. However, as seen in figures 5.1, 5.2, and 5.3, However, as seen in figures 5.1, 5.2, and 5.3, the positive ions are less affected by slight variations in the voltage than variations of flow or frequency. This is quite likely true for the negative ions too.

The Yasuda parameter, in W slm^{-1}, has been used here to examine oligomer formation for the various conditions studied. The average plasma power (P_{avg}) has been calculated as seen in chapter 4 using equation (4.4). In figure 5.8a it can be seen that the intensity of the positive oligomers in the 5 kHz pulsed case remained relatively constant as Y increased. A similar trend can be seen for the negative oligomers (figure 5.8c). For the 10 kHz pulse, however, the intensity of the positive oligomers increased by approximately an order of magnitude as Y increased from 45 to 95 mW slm^{-1} (figure 5.8b).

For the negative ions we see that the de-protonated acrylic acid negative ion ($[\text{M-H}]^-$) intensity increased as Y increased from 65 to 95 mW slm^{-1}, however

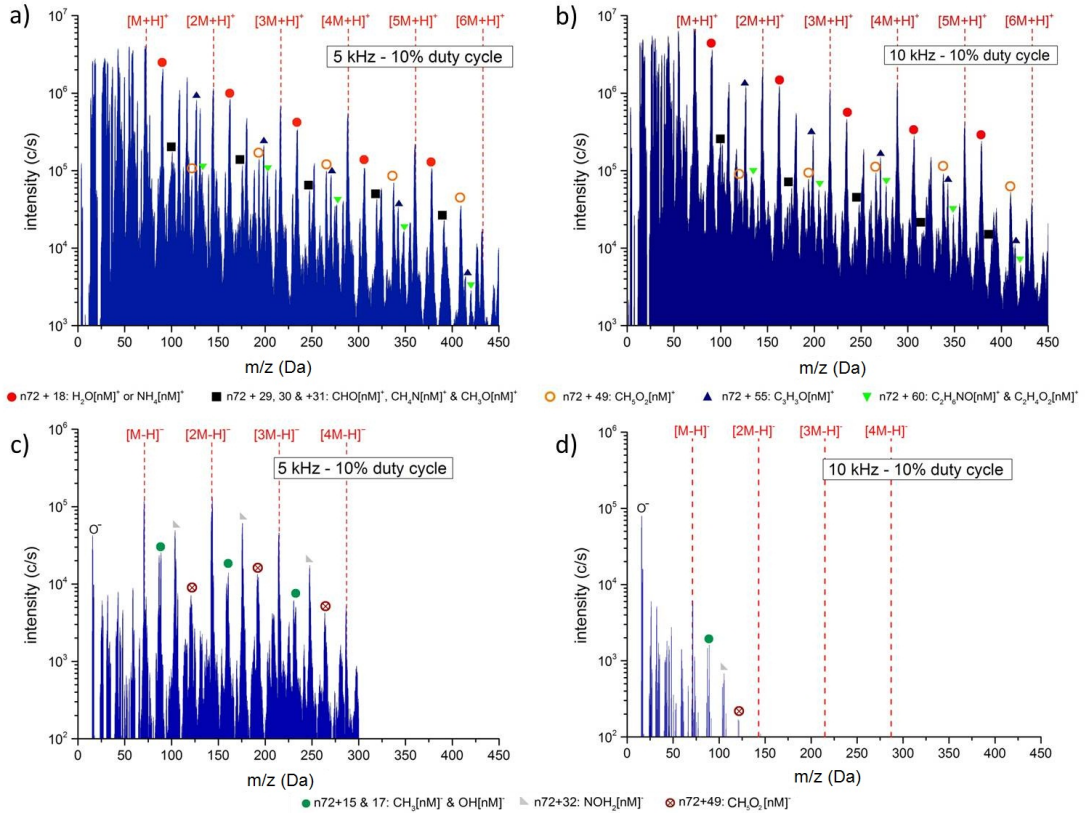

Figure 5.7: Time-averaged ion spectra for He^+ and acrylic acid for a) positive ions, 5 kHz, 10 % duty cycle, b) positive ions, 10 kHz, 10 % duty cycle c) negative ions, 5 kHz, 10 % duty cycle, and d) negative ions, 10 kHz, 10 % duty cycle.

there was a decrease of the higher order oligomers over the same range (figure 5.8d). One explanation is that a too high Y leads fo fragmentation of the heavier negative oligomer ions which is not the case for positive ions.

From figure 5.8 it can be seen that increased positive oligomer formation is linked to an increase of the average power. Although the average power effects positive oligomer formation it is not thought to be the main influencing factor for the formation of large negative oligomers, instead, negative ion formation is thought to be mainly influenced by formation time [171]. As the Yasuda parameter is proportional to the power and because the power is linked to the duty cycle only in the results shown in figure 5.8, the effect could also be explained in terms of duty cycle as seen in figure 5.9.

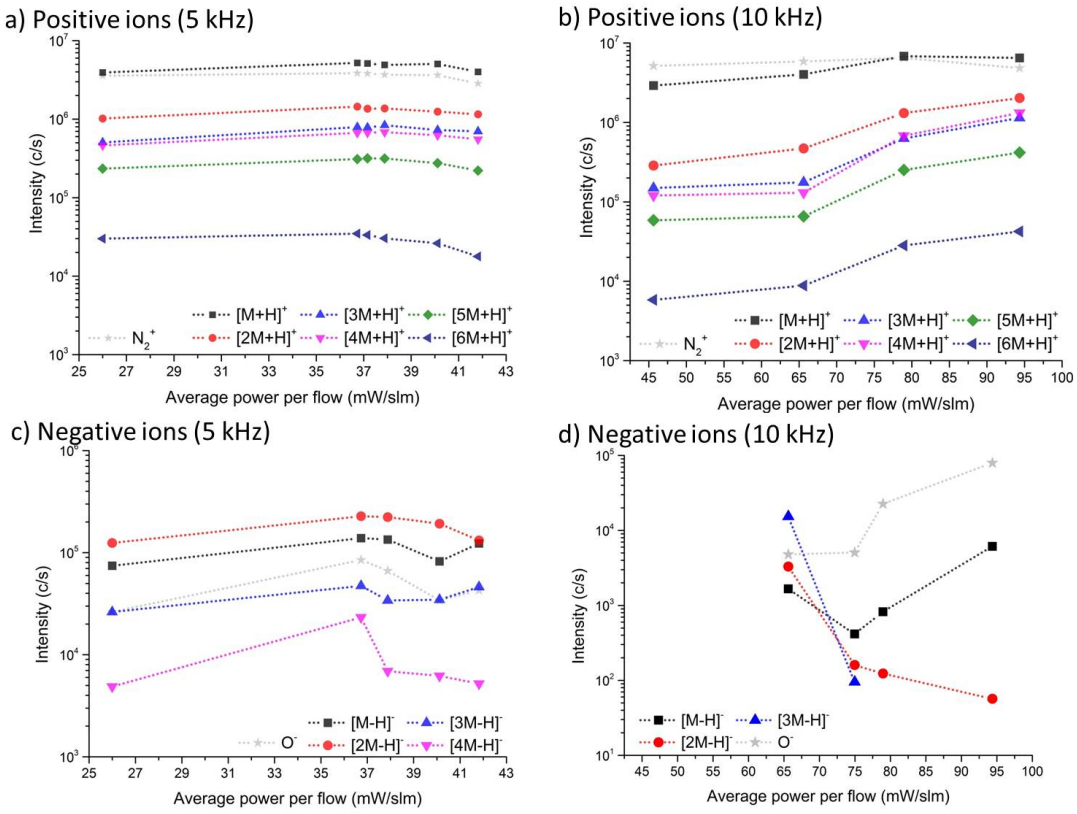

Figure 5.8: Trend of the main positive and negative oligomers as a function of average power/flow for 5 and 10 kHz.The power was modified whilst the flow was kept constant.

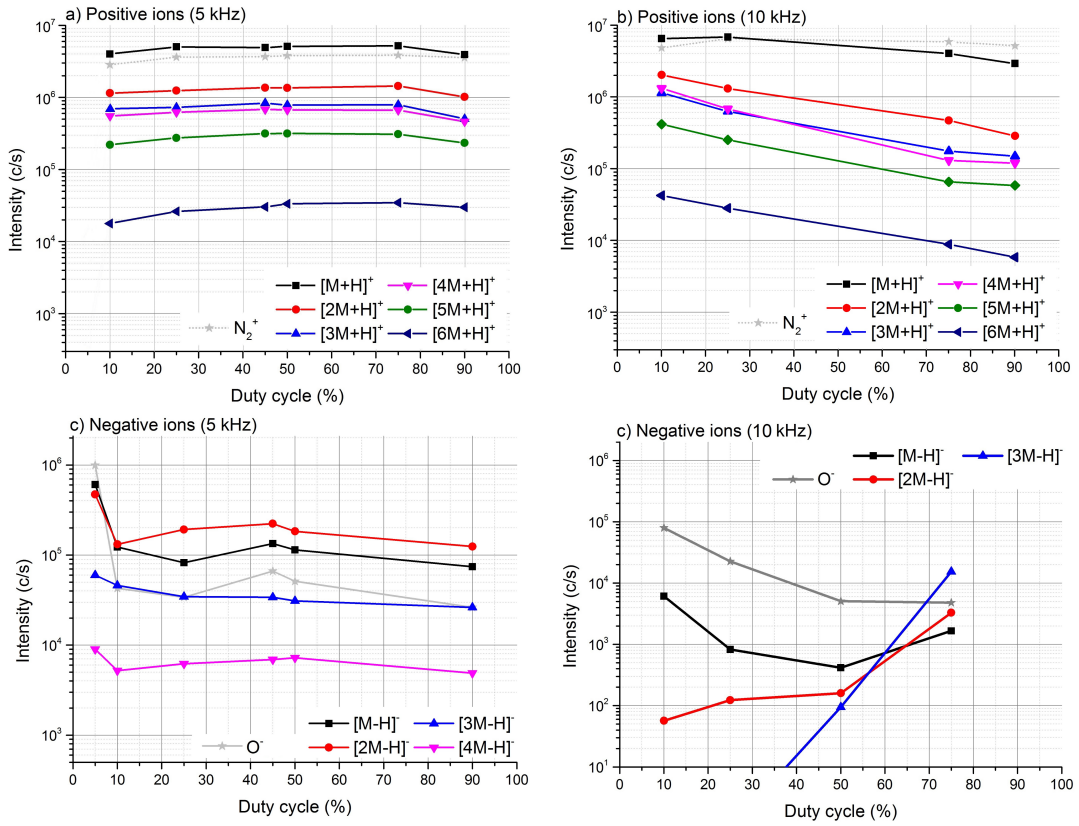

Figure 5.9: Trend of the main positive and negative oligomers as a function of the duty cycle for 5 and 10 kHz.

5.3 Time-Resolved Spectrometry

In the previous section, the measurements of time-averaged mass spectrometry has been shown. It has been seen that heavy oligomers of acrylic acid and heptylamine were created using a continuous wave or a pulsed DC signal. To understand the polymerisation mechanisms, time-resolved mass spectrometry of the pulsed DC atmospheric-pressure plasma jets were performed. This section presents the time-resolved measurements of positive and negative ions of acrylic acid using different duty cycles.

5.3.1 Introduction

Atmospheric-pressure mass spectrometry was used as described in section 3.2. The time-resolved measurement, as described in section 4.1.2, allows the detection of chosen masses during a time progression along a period of the signal. The variation of intensity of mass during a period provides important information to help understanding of the polymerisation process using atmospheric-pressure plasma jet.

As seen in section 5.2.4, changes in the duty cycle seemed to have a little effect on the positive ions of poly(acrylic) acid. This variation, however, could be the main cause in the modification of negative ions formation.

The next section analyses the formation of positive and negative protonated oligomers during a whole period. The effect of varying the duty cycle is studied, and measurements using two frequencies, 5 kHz and 10 kHz, are also compared.

5.3.2 Experimental Setup

The apparatus has already been describe in section 3.1 for the jet arrangement, section 3.1.2 for the electronics, and section 4.1.2 explains the gathering of the time-resolved measurement. As this chapter will show, the intensity of the species is not constant throughout time. Hence, when time-resolved measurements are taken at the interval when the intensity is maximal, the counts per second can be really high. Unfortunately the software does not allow recording of more than 10^7 counts per second to avoid damaging the detector. Hence low masses of high intensity as seen on figure 5.7 have their peak intensity too high to be

recorded without changing the experimental setup or the parameters. To be able to record these particular high intensity species, one would have to either lower the plasma power, position the electrode away from the mass spectrometer orifice, or decrease the orifice size. No such modification was made to be able to compare the time-resolved to the time-averaged measurements.

Only elements with lower intensity were selected to be recorded, i.e. $[2M + H]^+$, $[3M + H]^+$, $[4M + H]^+$, and $[M - H]^-$, $[2M - H]^-$, $[3M - H]^-$, $[4M - H]^-$ where M is monomer of acrylic acid. Heavier oligomers have an intensity too low to be useful in the time-resolved results presented in the following section.

5.3.3 Preliminary Results

Preliminary tests have been made using a slightly different mass flow than the other positive pulsed DC spectra displayed in this thesis. The mass measurements of the positive ions for the helium, monomer, and some oligomers are shown in figure 5.10. The detection of the helium ions are $\sim 20\,\mu$s after the first plasma bullet, whereas the maximum intensity of the heavy molecules is being measured $\sim 50\,\mu$s later than helium. One can observe that the heavier the species, the latter its peak of intensity is. This delay can be due to the longer formation time of heavier polymers.

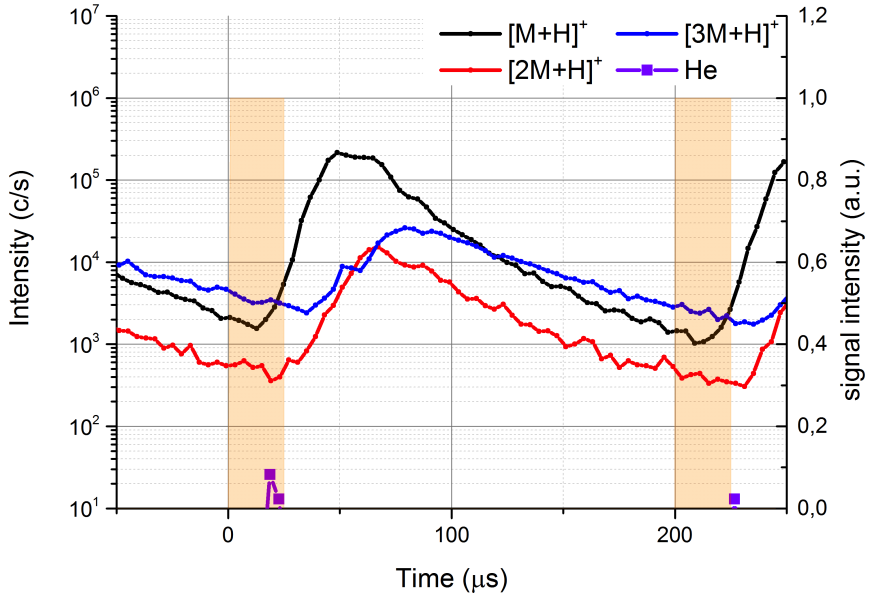

Figure 5.10: Positive time-resolved ion mass measurements of monomer, oligomers, and helium using 5kHz, 12.5% duty cycle, and 4 kV

5.3.4 Results and Discussion

Using time-resolved measurements of the plasma chemistry the temporal evolution of the polymer chains can be seen. Figure 5.11 shows the positive and negative oligomer ions for the 5 and 10 kHz pulses with a 10 % duty cycle (the 10 kHz cycle has been repeated over two cycles to display similar time-scales). From this it can be seen that peak positive oligomer formation occurred ~75 μs after the start of the pulse for both the 5 and 10 kHz cases. In the 5 kHz case, the small negative oligomer ion ($[M\text{-}H]^-$) also reached peak formation after ~75 μs, however the larger negative ions ($[n M\text{-}H]^-$, where n=2-4) did not reach their peak until ~125 μs after the start of the pulse. It is worth mentioning that these delays are not due to the time of flight in the mass spectrometer as the algorithm has been applied on the measurements shown (see appendix A.2 for the details of the algorithm). This delay is due to the time necessary for the oligomers to form. As a result of this longer formation time the larger oligomers do not have sufficient time to reach peak formation in the 10 kHz case. This accounts for the lower intensity observed in figure 5.11f and 5.12f for the negative ions in the 10 kHz case compared to that observed in the 5 kHz case. The time delay between

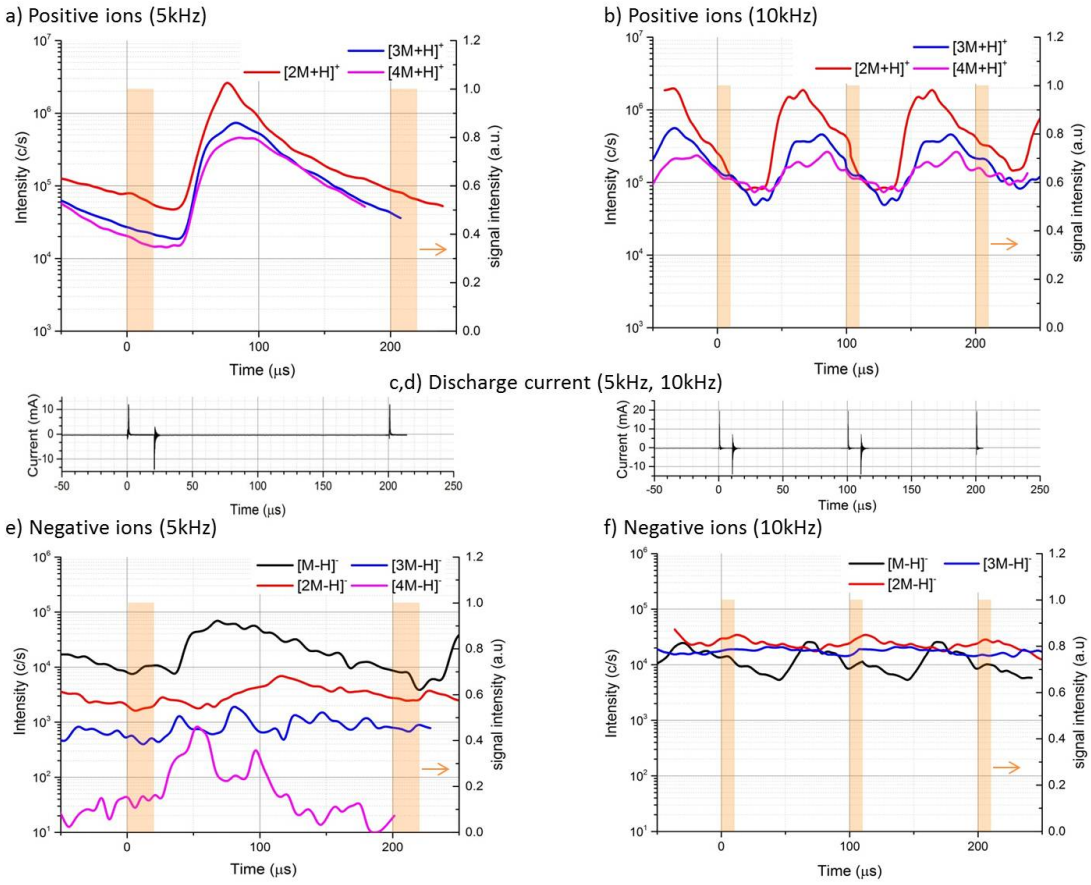

Figure 5.11: a) Positive and e) negative time-resolved ion mass measurements using 10 % duty cycle of a 5 kHz signal and b) positive and f) negative ions using 10 % duty cycle of a 10 kHz signal. Currents are shown for both frequency: c) 5 kHz and d) 10 kHz. In the 10 kHz cases, the signals have been duplicated to display similar time scale to the 5 kHz cases.

the pulse and the peak oligomer formation indicates that the formation of the polymer chains occurs in the afterglow region of the plasma.

To better understand the influence of the positive and negative current peaks, which are generally associated with the plasma jet ionisation fronts, on the oligomer formation the time-resolved spectra from the 50 % duty cycle case is presented in figure 5.12. From this it can be seen that there were two periods of positive ion production for the 5 kHz case, one peaking ∼50 μs after the positive current peak and one ∼50 μs after the negative current peak. This implies that positive ion oligomer formation is influenced by both of the ionisation fronts which propagate away from the powered electrode. The first production period

shows creation of larger oligomer ions from smaller ones, the second period, however shows fragmentation of large oligomers to smaller ones hence the change in species dominance over the pulse cycle. For the 10 kHz pulse there was only one period of formation visible, this period starts $\sim$90 μs after the start of the pulse and peaks during the beginning of the next pulse. As a result of the shorter cycle in the 10 kHz case the polymers do not undergo fragmentation in the off-phase, as was observed in the 5 kHz case, so the positive polymer intensity increases as a function of power/flow as shown in figure 5.8b.

For the negative ions, one distinct period of increased production can be seen in the 5 kHz case $\sim$50 μs after the start of the voltage pulse. In the 10 kHz case there is no distinct period of increased production for the negative ions, again this is a reflection of the longer generation time required to reach peak production for the negative ions.

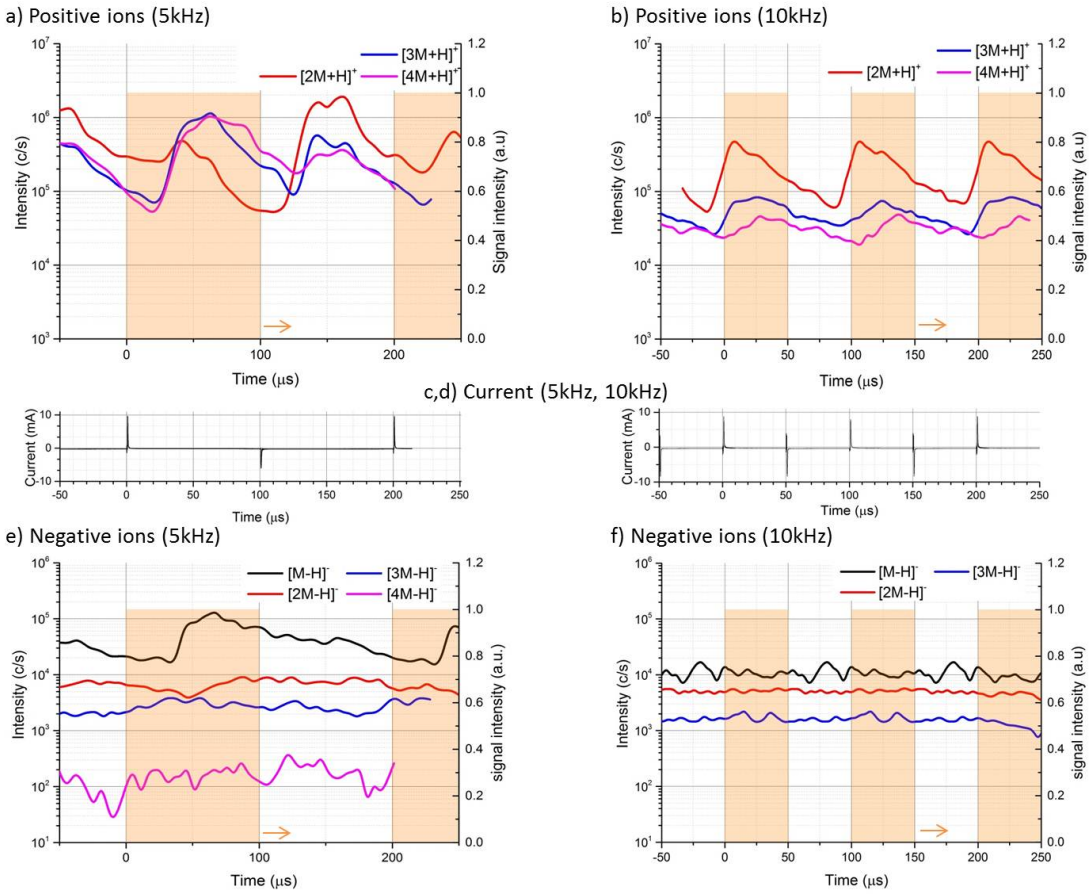

Figure 5.12: a) Positive and e) negative time-resolved ion mass measurements using 50 % duty cycle of a 5 kHz signal and b) positive and f) negative ions using 50 % duty cycle of a 10 kHz signal. Currents are shown for both frequency: c) 5 kHz and d) 10 kHz. In the 10 kHz cases, the signals have been duplicated to display similar time scale to the 5 kHz cases.

5.4 Conclusions

Polymerisations of heptylamine and acrylic acid have been performed and analysed using atmospheric-pressure plasma jets. Mass spectrometry of positive and negative ion species has been performed for different jet parameters. Heavy positive and negative ions have been detected. This shows that polymerisation of the monomers occurred in the plasma. Section 5.2.4 presents the measurements of time-averaged mass spectrometry which have shown that heavy oligomers of acrylic acid and heptylamine were created using a continuous wave or pulsed DC signal. The duty cycle has been varied and the effect of this variation on the

intensity of the acrylic acid oligomers have been analysed. The positive protonated ions were seen to be only slightly affected by the variation of the duty cycle, however, the negative de-protonated ions are very sensitive to this variation.

Section 5.3.4 presents time-resolved measurements of acrylic acid oligomer ions for two frequencies (5 kHz and 10 kHz) and for different duty cycles. It has been shown that there appears to be little difference between the on-time and the off-time period on the positive ions. However, the duration between the positive and the negative bullet plays an important role in the evolution of oligomers formation. As the bullets are created during the rise and fall of the voltage, this means that both the duty cycle and the frequency can vary the temporal creation of the polymerisation. A delay of a few tens of μs between the bullet creation and the detection of the oligomer shows that the oligomer ions are not created in the bullet, rather the polymerisation occurs in the plasma tails. This can be explained as follows: in the bullet, the energy of the electrons and photons is too high to lead to polymerisation, however, in the tail of the bullet, radical and metastable species subsist. These species, as seen in section 2.3.1 and 2.3.2, are the most important in the polymerisation mechanisms. The heavier oligomers have their maximum intensity slightly after their lighter counterparts because they require more steps to form. By analysing the variation of time-resolved measurements of protonated oligomers, step-growth formation of oligomers has been confirmed.

Chapter 6

Analysis of Deposited Thin Films

Polymerisation plasmas of acrylic acid have been analysed as a function of different parameters using mass spectrometry in chapter 5. In this chapter, deposition using similar plasmas were performed and examined. This chapter presents the analysis of two different batches of poly(acrylic) acid samples deposited using atmospheric-pressure plasma jets. The surface of the deposited thin films were examined using XPS and TOF-SIMS. Preliminary studies of the effect on the charge deposition of an atmospheric-pressure plasma jet of helium on an insulating substrate were also performed.

6.1 Introduction

Acrylic acid has been studied more in the literature than heptylamine, therefore depositions presented in this chapter have been made using only acrylic acid. Two different experimental setups have been used in order to deposit acrylic acid. One setup was a horizontal configuration with a fixed jet on a fixed substrates and the other setup used a vertical arrangement with a fixed jet on a moving substrate. The first batch of samples was made using the manual flow controllers and the horizontal setup using a pulsed DC jet, they were analysed with TOF-SIMS and XPS. The second batch was created later on with the MKS digital flowmeters using the vertical arrangement and a positive pulsed DC. A few deposited samples were made for the second batch and TOF-SIMS was performed on them for different duty cycles. Unfortunately the second batch could not be analysed by XPS due to technical difficulties. Both XPS and TOF-SIMS have been performed

at the University of Nottingham by Sebastiaan van Nuffel as explained in section 4.2.1.

6.2 Experimental Setup

This section describes the apparatus and methods used for depositing the two batches of samples and also the film analysis devices.

1) First batch
For the first batch, the continuous wave jet was used, a description of the configuration of the apparatus is given in section 3.1.1. A grounded metallic plate of 50×60 mm was put 10 mm in front of the jet. The jet was driven by a pulsed DC of 4 kV and 5 kHz with an on-time of 10 μs. A glass slide of 10×10 mm was then attached on the metallic plate in front of the plasma plume. To avoid the plasma plume searching for direct contact with the metallic plate behind the glass sample, wide pieces of insulated tape was put around the glass sample. The samples were exposed to the plasma for 5 minutes.

2) Second batch
For the second batch, a motorised $x - y$ stage was used to deposit on the samples according to a chosen shape. The $x - y$ stage was connected and controlled by a custom-made Matlab software. A cross was chosen as the shape (see figure 6.1) in order to allow analysis of regions of varying deposition thickness and to study the edge of the deposition area. The time needed for the moving stage to complete the pattern was 5 minutes. The experimental setup involved using a positive pulsed DC signal, as is described in section 3.1.2. The moving stage involved a stainless steel plate, polished by hand, connected to ground. A 1 mm thick acrylic sheet of 20 x 20 mm was added on top of the stainless steel plate during the charge density analysis. For the deposition, the glass substrates of 10 x 10 mm were added on top of the stainless steel plate. Pieces of Kapton tape were placed over each other forming an L shape on the plate to be able to accurately position the glass substrates as shown in figure 6.2. Furthermore, a single layer of insulated tape was place under the edge of the substrate. This was done to prevent the plasma from directly reaching the grounded metal plate when close to the substrate edges.

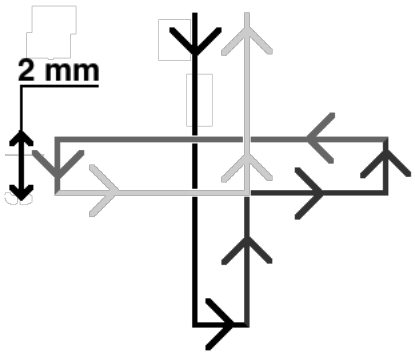

Figure 6.1: The path of the atmospheric plasma jet over the glass samples.

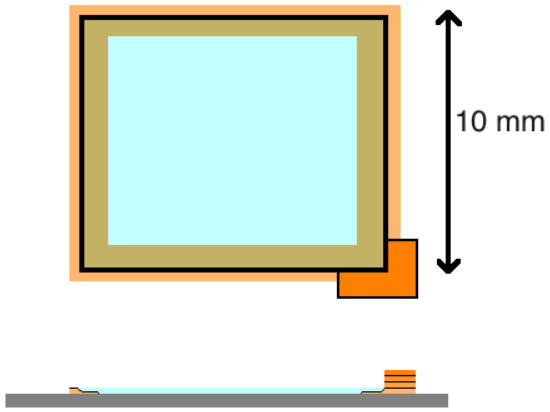

Figure 6.2: Diagram of the glass substrate on the grounded metallic plate (grey), the orange rectangles are the pieces of Kapton tape.

XPS

Information about the derivatisation of the carboxyl group and the high resolution of C 1s scan are given in section 4.2.1.

Reference ions for TOF-SIMS

For the first batch, the sample analysis was performed 6 days after the deposition was made. For the second batch, the analysis was made ∼1 month after the deposition. These delays can alter the quality and composition of the deposited film and need to be taken into account when analysing the results.

A list of expected peaks in the TOF-SIMS results is given. In the positive spectrum, key peaks are expected at a m/z ratio of 18 (H_2O^+), 27 ($C_2H_3^+$), 45 ($COOH^+$), 55 (CH_2CHCO^+), and 72 (M^+) [169]. These ions arise from fragmentation of the acrylic acid monomer. Higher mass peaks may arise at m/z ratio of 145 ($[2M+H]^+$) and 217 ($[3M+H]^+$) [169]. In the negative spectrum, peaks originating from the acrylic acid monomer are expected at a m/z ratio of 41 ($CHCO^-$), 59 ($CH_3CO_2^-$), and 71 ($[M- H]^-$) as well as peaks at a m/z ratio of 143 ($[2M-H]^-$), 215 ($[3M-H]^-$) and 287 ($[4M-H]^-$) [166].

Electrostatic probe

The electrostatic probe was held via a clamp over the $x-y$ stage. An acrylic

substrate was cleaned using isopropanol which was left to evaporate off, as rubbing a cloth to dry would have created static charges. Rubber gloves were used during the manipulation of the substrate. A thin sheet of aluminium connected to the ground was slowly passed over the surface in an attempt to reduce the electrostatic charges on the substrate surface. A pure helium plasma jet using continuous wave voltage was exposed to the sample for 1 minute and then switched off by quickly reducing the voltage and stopping the helium flow. The acrylic sheet was then moved with great care underneath the contactless probe attached to the manual $x - y$ stage (see figure 3.8). The probe was then manually moved, in steps of 0.5 mm, 15 mm on the y-axis and 13 mm on the x-axis around the spot where the plasma plume was in contact with the acrylic substrate.

6.3 Preliminary Results

Initially the electrostatic probe measurements were studied. The goal was to analyse the effect of a pure helium APPJ driven by a sinusoidal voltage.

6.3.1 Electrostatic Measurements

The surface potential measured under the probe is shown in figure 6.3. The area measured by the probe is $\sim$53 mm^2 and thus each measurement overlaps each other leading to smoother results.

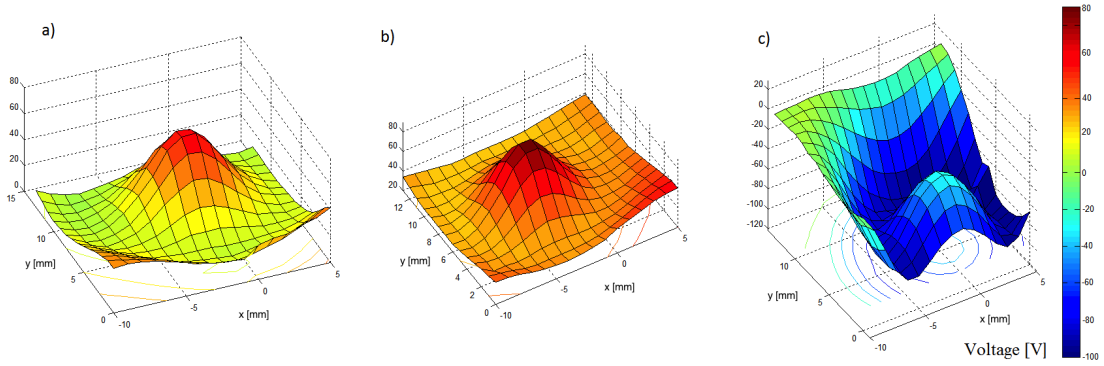

Figure 6.3: Three different surface potential obtained from the voltage probe. The time when the plasma is turned off differs causing different values of the surface potential (a), b), and c)), however, the pattern does not vary.

According to [189] the charge density changes its sign during the period, however, the shape is more or less constant. The charge density results, calculated using equation (4.7), are shown in figure 6.4. The cross section presented at the bottom is made along the y-axis. Figures 6.4a-b show a positively charged profile whereas figure 6.4c shows a negatively charged profile, thus the results presented are in agreement with this article. The profile has a ring-shaped, this is due to the cylindrical configuration of the plasma jet. The profiles are similar to those in [189].

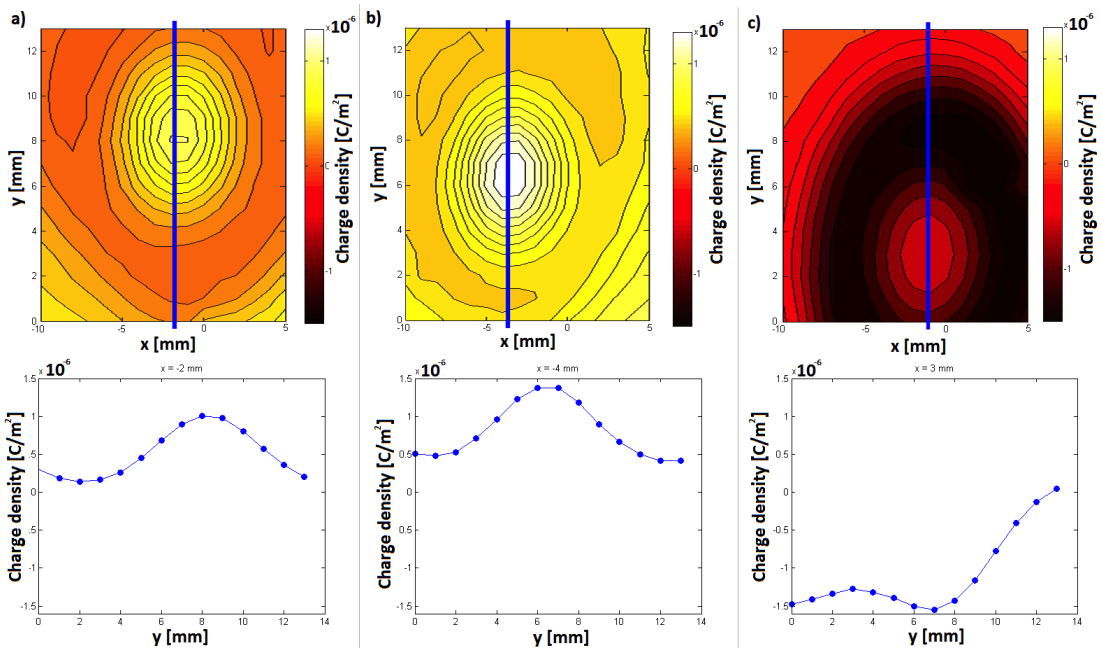

Figure 6.4: Charge density on a acrylic sheet after a helium plasma jet treatment. Top: maps of charge density. Bottom: sections of the charge density crossing the center of deposition. Again, the time when the plasma is turned off differs causing different values of the surface potential (a), b), and c)) whist keeping the same pattern.

Simulation

Simulations of a helium plasma with similar parameters (dimension, pressure, maximum voltage, frequency, etc.) have been done. The surface charge distribution of figure 6.5 is taken from one of these simulations where the dielectric is assumed to be positioned at 3 mm distance from the orifice. At this distance, the bullet's head maintains its annular structure. The simulation was performed

using COMSOL by M. Hasan at the University of Liverpool. This simulation is not detailed here and only serves as an aid to help understand the shape of the charges left on the substrate.

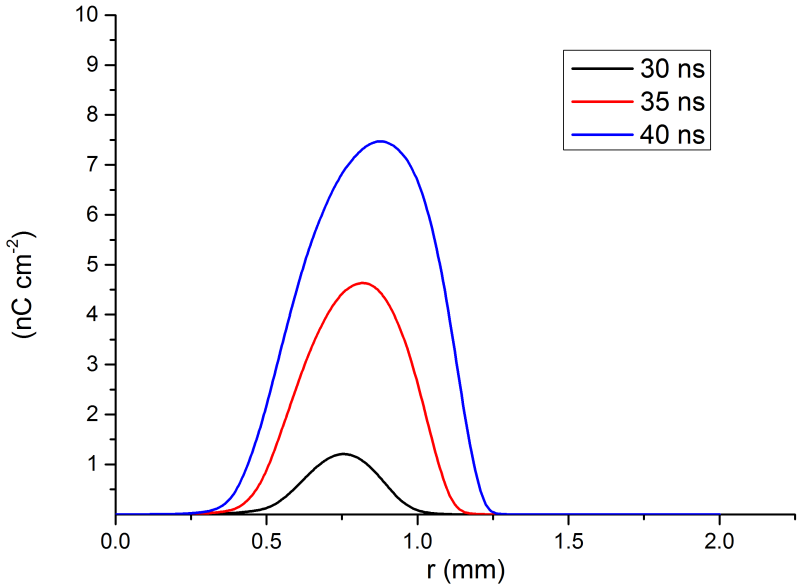

Figure 6.5: Simulation of the charge density section at different time after the end of the pulse. The origin of the x-axis is the center of the plasma plume. Made by M. Hasan, University of Liverpool.

Figure 6.6 shows the difference in the bullet structure for cases where the dielectric is assumed to be 3 mm and 10 mm from the orifice respectively. For 10 mm the structure changed from annular to spherical. The surface charge distribution for 10 mm case is not available at the moment

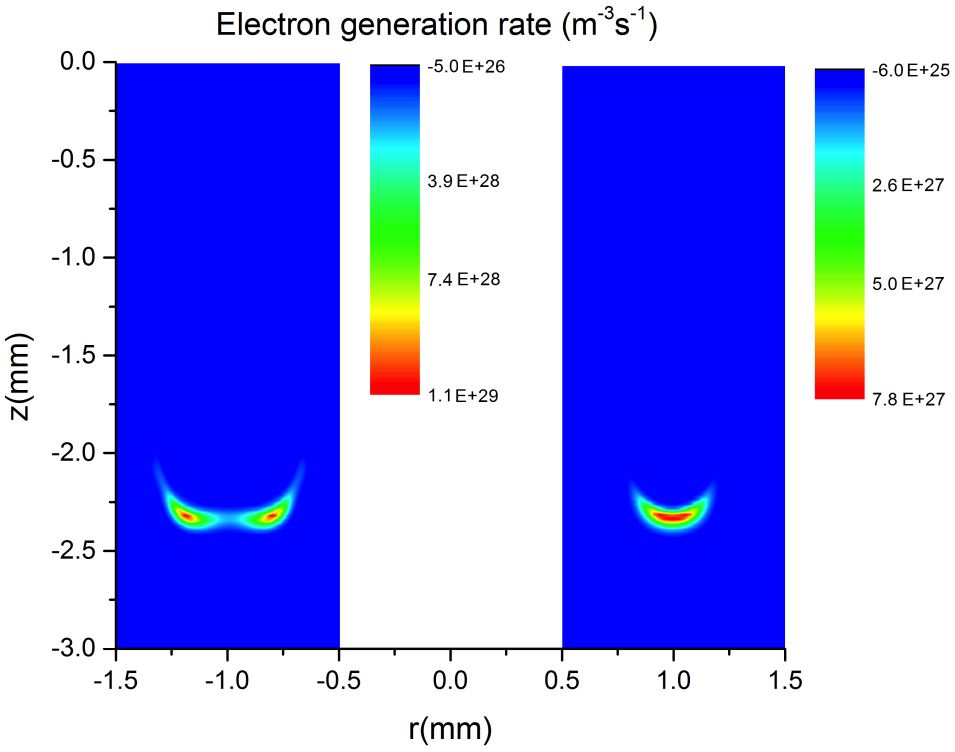

Figure 6.6: Simulation of electronic density of a helium plasma jet.

Problems and development

The difference of value between the simulation ($8\times10^{-5}\,\mathrm{C\,m^{-2}}$) and the measurements ($1.5\times10^{-6}\,\mathrm{C\,m^{-2}}$) is almost 2 orders of magnitude. Several explanations can be made. The first one is the time between the bullet hitting the dielectric and the recording of the charges. In the simulation the charge densities are taken when the bullet hits the surface whereas in experiment, the measurements were taken several minutes after, this can also explain the difference in charge density. The way the plasma jet was switched off: by quickly reducing the high voltage signal, can affect the last plasma bullet by reducing its electron and ion density. Another explanation can be that the simulation used a positive pulse which induces a much higher displacement current compare to the continuous wave signal from the experimental plasma. The distance can also influence the result. If the jets is a bit further away from the surface compared to its simulation counterpart, the deposited charge on the surface will be also smaller than expected [189].

6.4 Results and Discussion

The electrostatic charge deposition of a pure helium APPJ was analysed, a ring-shape pattern was observed. This section examines the film composition of acrylic acid deposited by APPJs of different paramters. TOF-SIMS measurement allows detection of patterns in the deposition. Analysis of deposition for different jet parameters indicates their effect on the deposition and the plasma polymerisation.

6.4.1 XPS

The XPS results shown in this section are only a selected few of the analyses performed. Only the first batch of samples have been analysed using XPS. Tables 6.1 and 6.2 and graphs in figure 6.7 are focused on the carbon 1s binding energy. The values are averaged over measurements from three separate films . Table 6.1 corresponding to the values shown on the graph in figure 6.7a) give the percentage of the elementary composition of the carbons. In a pure acrylic or poly(acrylic) acid surface the results would be 33 % for CCOO, COO and C-H/C (see section 4.2.1 for more explanation). The important functional group in acrylic acid is the carboxyl group corresponding to -COOH. As the results show, the XPS can only detect the COO group and cannot tell if any other element is attached to it, be it hydrogen, another atom, or a molecular group. As the carboxyl group is of high interest, the surface was transformed using trifluoroethanol derivatisation (see section 4.2.1). This technique consists of selectively modifying only the carboxyl group (-COOH) into a new compound, -$COOCH_2CF_3$. The new surface can be analysed by XPS where the CF_3 is clearly visible (see figure 6.7b). The ratio between CF_3 over COO in the derivatised sample is the percentage of the COOR detected being COOH, where R represented any molecule or group. The retention of carboxyl group, which is the percentage of measured carboxyl group over the theoretical percentage, is then calculated using the following formula:

$$\frac{[\mathrm{COO}]_{\mathrm{underivatised}}}{33} \cdot \frac{[\mathrm{CF_3}]_{\mathrm{derivatised}}}{[\mathrm{COO}]_{\mathrm{derivatised}}}$$

The retention was calculated to be 23.43 % using table 6.1 and 6.2. A retention of carboxyl group of ∼25 % is low, most low-pressure plasma polymerisation in the literature obtained a retention of 45 % and above [100]. However, published articles do not always perform derivatisation and often use only the ratio of

COO/33 as the retention assuming that all the COO are coming from the carboxyl group [30,100,103,120,123,169,170][1]. One could note that if a similar assumption was performed here a retention of 67 % could be claimed.

Measurement: [%]				
C=O / O-C-O	CCOO	CO	COO	C-H/C
17.03	0.19	28.86	22.08	31.83

Table 6.1: Values of the underivatised XPS.

Measurement: [%]					
C=O / O-C-O	CCOO	CO	COO	C-H/C	CF3
16.9	1.69	27.08	21.45	25.35	7.51

Table 6.2: Values of the derivatised XPS.

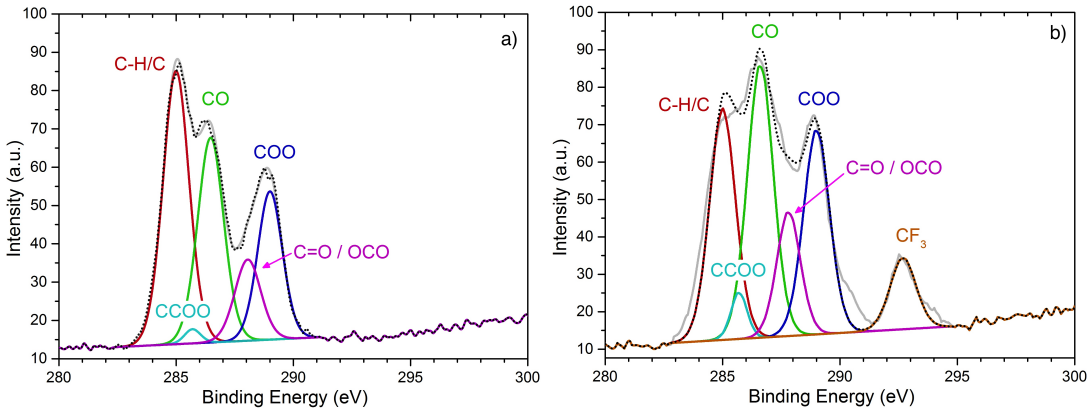

Figure 6.7: XPS results of the C 1s binding energy, with a) underivatised and b) derivatised sample.

6.4.2 TOF-SIMS

Table 6.3 shows a couple of examples of surface concentration for different ions. The graphs in the first column are the total positive and negative ions detected. The two graphs on the second column are both acrylic acid fragments concentration: the top one from the positive ion $C_3H_3O^+$ and the bottom one from

[1] A publication which does not state if derivatisation was performed is assumed to not have done it.

the negative ion $C_2H_3O_2^-$. These graphs prove that components from acrylic acid have been deposited on the glass. The third column of table 6.3 shows the heaviest ions detected by the TOF-SIMS machine, having a mass heavier than an oligomer containing 2 monomers (144 Da), it proves that polymers have been deposited on the glass. The two graphs of the 4th column are ions coming from the glass surface itself, they show, accordingly with the other TOF-SIMS graphs, that the deposition has a ring-shape. This shape can be one of the reason for the poor carboxyl retention measured on the XPS and reported in the previous section. The XPS analysed only a small spot in the center of the deposition. TOF-SIMS results show that the center of the deposition does not contain the maximum of the coating.

	total	$C_3H_3O^+$	206.10$^+$	Na_2OH^+
+ ions	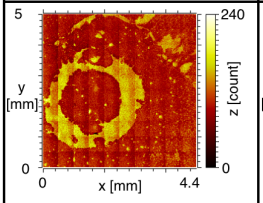	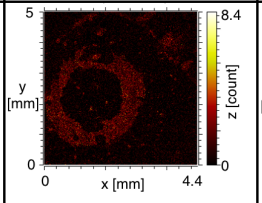	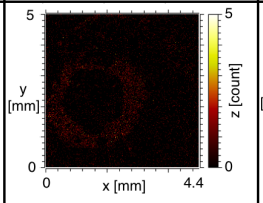	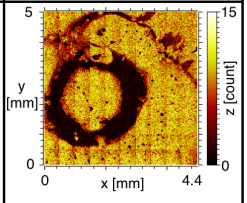
	total	$C_2H_3O_2^-$	133.01$^-$	$SiHO_3^-$
- ions	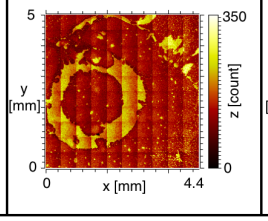	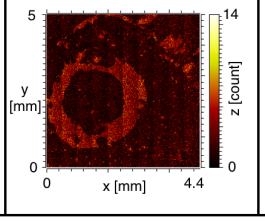	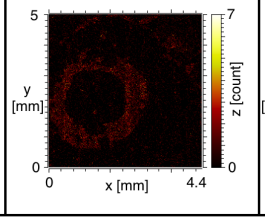	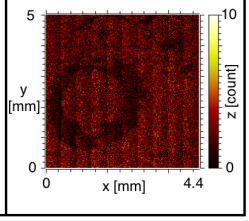

Table 6.3: Positive and negative ion TOF-SIMS of thin film deposited on glass made using a pulsed DC jet, 5 kHz, 10 μs.

Figure 6.8 shows TOF-SIMS images of the second batch of thin films deposited using different APPJ parameters. The image shows the total of the detected positive ions, with the colour code as follows: the low luminosity (dark red) represents the minimum of the intensity measured and the high intensity (light red) the maximum of ions measured. The first row shows the effect of the increase of the jet voltage and the second row of the increase in the duty cycle. Intensities of the masses from 1 to 200 Da has been measured and are given in the appendix

A.8.

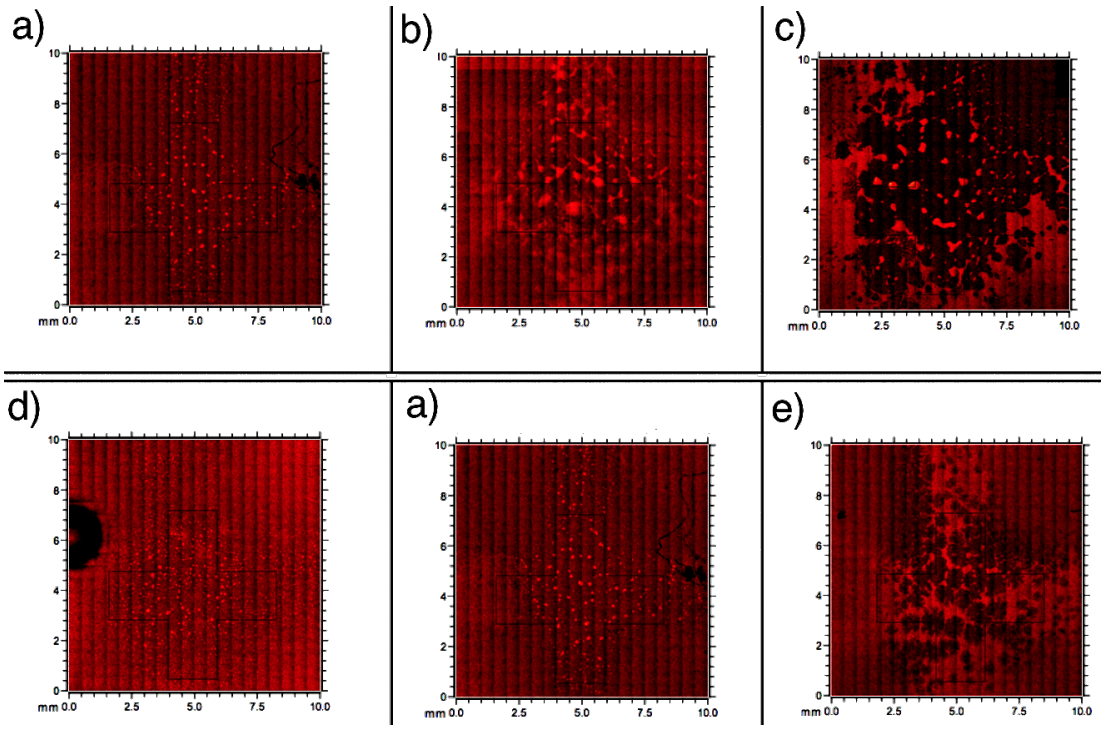

Figure 6.8: Positive ions TOF-SIMS of thin film deposited on glass made using a 5 kHz pulsed DC jet, with the following parameters: a) 3.7 kV (peak-to-peak) & 100 μs(on-time), b) 4 kV & 100 μs, c) 4.3 kV & 100 μs, d) 3.7 kV & 20 μs, and e) 3.7 kV & 150 μs. Dark red represents the minimum of intensity and light red the maximum. The slight black cross is added to show the path of the deposition.

The change of voltage clearly has an important impact on the deposition. The films made using 3.7 kV (figure 6.8a,d-e) all have an intensity of $[M+H]^+$ lower than for the 4 and 4.3 kV. However, for the $[2M+H]^+$ peak, the intensity is twice as high for the 3.7 kV than for the other two voltage (see spectra in appendix A.8). This indicates that higher voltages reduce plasma polymerisation as it has been seen in the plasma phase.

The deposition follows the cross shape made by the plasma jet. The effect on the deposition is clearly noticeable in figure 6.8 by the higher intensity of positive ions measured (light red). For the deposition made using 3.7 kV with different duty cycles, the following observations can be made. For the shortest duty cycle (10%, figure 6.8d) the positive ions detected agglomerate into small dots, for the middle duty cycle (50%, figure 6.8a) the dimensions of the agglomerations

are bigger, whereas for the highest duty cycle (75%, figure 6.8e) there is no more dotted agglomeration, the deposited area seems connected to each other forming a fractal pattern. Further investigation should be performed to indicate the benefit of each deposition pattern.

The change in duty cycle does not seem to affect the intensity of the masses lower than 200 amu. One noticeable change is the intensity of the 90 amu positive peak ($H_2O[M+H]^+$ or $NH_3[M+H]^+$) as shown in table 6.4.

duty cycle (%) (*on-time (µs)*)	intensity (counts)
10 (*20*)	1.0×10^4
50 (*100*)	4.5×10^4
75 (*150*)	4.0×10^4

Table 6.4: Intensity of the 90^+ Da peak of deposition of acrylic acid for different on-time. Taken from TOF-SIMS spectra shown in appendix A.8

6.5 Conclusions

Firstly, a study on the effect of a pure heluim atmospheric-pressure plasma jet on the surface charge density of an insulating surface has been made. The results are in agreement with the literature; a ring shaped pattern is left on the surface once the plasma is switch off. Wild *et al.* performed some live measurements and recorded that this pattern is constant but that the surface potential varies, following the driven voltage [189]. The measurements made were performed once the plasma was off, leaving only the surface charge density left by it. Comparison with 2D COMSOL simulations were made and although the value of the surface charge density were ∼2 order of magnitude lower, the shapes were found to be similar.

This ring shape was observed on the thin film deposited using a fixed jet. TOF-SIMS measurements show that a ring shape containing heavy ions were deposited. The ions detected were heavier than the monomer weight proving that polymerisation occurred and was deposited, however the ions detected on the surface differ from those detected in the plasma using the mass spectrometer (see chapter 5). There are several explanations for this difference. One is that the plasma interacts with the polymers deposited on the surface, modifying the

composition before new polymers were deposited. Another reason can be made by looking at the graph of the mass spectrometry of the atmospheric plasma containing acrylic acid: the amount of compounds which are not simply the oligomer $[nM + H]$ ions are important leading to a very complex deposition mechanism. It is possible that some molecules are very stable in the gas phase but are not in the solid phase, thus are not being deposited on a substrate. Further investigation should be made in this direction.

The deposition using the cross pattern have shown that although the plasma jet was moving flawlessly almost all the samples display agglomeration of deposition. The size of these agglomerations are dependent on the duty cycle of the pulsed DC signal. The intensity of the peak-to-peak voltage also affects the deposition, using a voltage too high can alter the deposition by leading to bigger agglomeration and increasing the deposition area. This shows that using a too high voltage is not suitable to deposit precise pattern with an APPJ. It has also been measured that the density of $[2M+H]^+$ is higher with lower voltages.

The XPS results have shown that the carboxylic retention of the deposition is only $\sim$25%. This value has been obtained using a derivatisation which although make the results very certain in terms of quality (the retention measured comes only from the COOH group), error can come in term of quantity (the derivatisation is $\sim 87 \pm 15\%$ efficient [166]). Another reason for the low retention measured is the high quantity of fragmented compounds in the plasma, these fragments can decrease the carboxylic retention value. Furthermore, ions seem to contain a high percentage of heavy polymers, however, neutrals contain mainly monomer [87] . As a non-thermal plasma is mainly composed of neutral, this can lead to a low total number of oligomers which can be reflected by the deposition composition.

Further analysis of the deposition should be made to evaluate their properties such as its hydrophobicity or its efficiency of immobilisation of a biomolecule.

Chapter 7

Plasma-Enhanced Atomic Layer Deposition

This thesis also studies depositions of a low-pressure plasma reactor coupled with an ALD machine. This PEALD reactor was used to deposit aluminium oxide (Al_2O_3) using trimethoxyamphetamine ($Al_2(CH_3)_6$ or TMA). The particularity of the plasma reactor is that it was conceived as an atmospheric-pressure surface discharge.

7.1 Introduction

ALD and PEALD, as explained in section 2.5, are techniques used worldwide when high precision in terms of thickness and quality of deposition are required [191]. In this thesis a simple surface discharge arrangement was added to an existing ALD machine. The chamber temperature was reduced to approximatively room temperature. The plasma was controlled by the ALD device and was thus switched off and on along with the ALD cycle. Different cycles were performed to analyse the response of the deposition to the cycle, in terms of quality and thickness. Two studies have been made by each using five different deposition cycles:

1. The number of cycles was increased from 50 to 800 whilst keeping all the other parameters fixed.

2. The duration of the oxidation step was modified from 2 s to 16 s for a fixed number of cycles.

The result of the first study should give a linear trend of the thickness as a function of the cycles. This will allow the calculation of the deposition rate per cycle. The results of the second trend should produce a saturation curve which can give the shortest time needed for the oxidation step (see section 2.5). A saturation curve implies that the deposition mechanism is one from ALD and not from CVD. To be able to produce ALD at room temperature using TMA and air or water as a precursor, a plasma assisted oxidation step is necessary. Otherwise the temperature window is 100-300 °C, above 300 °C the TMA desorbs from the surface and the growth rate decreases. A temperature of ∼300 °C is usually used to obtain good quality films in terms of thickness uniformity and refractive index [192].

7.2 Experimental Setup

The experimental setup is as described in section 3.4. The ALD device was situated in a clean room in the department of materials science of the University of Liverpool.

The plasma was turned on during the oxidation step and was turned off for the rest of the cycle. The input voltage was gated to the controlled box of the ALD device. The plasma reactor can thus be controlled along with the other parameters of the cycle by the ALD software.

Argon was used as the inert purge gas. A flow of 20 sccm of argon was constantly flowing through the ALD chamber. A small leak between the argon bottle and the chamber was intentionally added to allow air to enter the chamber. The signal was a continuous wave of ∼1.7 kV peak-to-peak and a frequency of ∼42 kHz. The reactant was liquid TMA ($Al_2(CH_3)_6$), argon gas flowed through a gas bubbler to inject TMA particles into the ALD chamber. A typical deposition is a succession of cycles described as follows:

1. TMA pulse of 0.02 s
2. A 3 s pause
3. Plasma for 3 s
4. A 3 s pause

5. Repeat

The duration of step 3 was varied from 2 s to 16 s and the number of cycles was varied from 50 to 800.

The samples were made of silicone and were cut manually using a glass cutter. The refractive index of the silicon sample was always measured before being put in the ALD chamber. The samples were only handled with rubber gloves.

The samples were placed as shown in figure 7.1 inside the ALD chamber. The lid containing the plasma reactor was then closed and the chamber was pumped down using a rotary pump. The argon flow was then fixed to 20 sccm which fixed the pressure to ∼0.9 Torrr. The bottom of the chamber was heated by an internal electrical heater to 50 °C.

When the deposition was finished, the pump was switched off and the chamber was vented using a small valve. Once the lid was opened, the samples were directly measured by the ellipsometer to determine the refractive index and the thickness. Figure 7.2 shows the experiment setup with the plasma turned on.

Deposition of Al_2O_3 was performed with the help of Dr. Ian Brunell who performed the spectrometry analysis of the silicone samples.

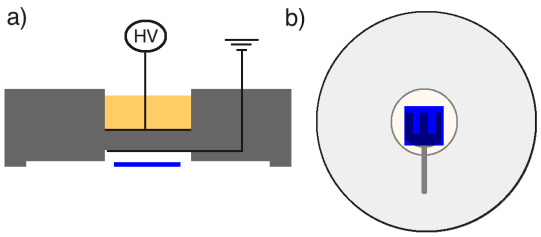

Figure 7.1: Cross-section a) and top view b) of the PEALD reactor with in blue the silicone wafer.

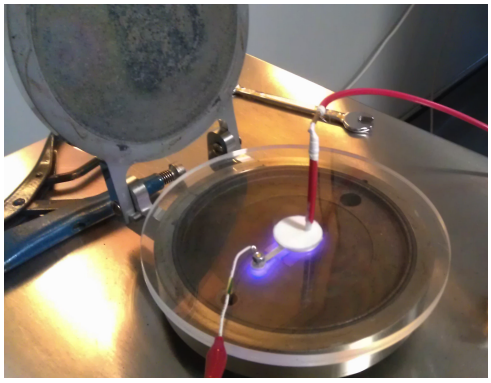

Figure 7.2: The PEALD experimental setup, with the plasma visible through the acrylic lid.

7.3 Results and Discussion

On a conventional ALD, without the assistance of the plasma, the oxidation step is made using water vapour gas and by having the chamber temperature around

300 °C. Using TMA, oxygen, and argon as the purge gas, Al_2O_3 has been made with the same ALD device at a temperature of 50 °C.

Several attempts did not work due to arcing problems. The optimum working pressure and voltage were found after several attempts. This difficulty implies that if this apparatus is used on another device using pure oxygen or an argon-oxygen mixture, tests with different voltage and pressure would be necessary to find the optimal condition for the discharge.

Another problem occurred when the voltage was too high. The plasma reactor created small arcs, these small filaments were barely visible, however, they are made of high current which disturbed the electronics of the ALD device, causing a lose in contact between the computer and the ALD controller box.

Variation of the number of cycles

The first study of the PEALD of aluminium oxide involves varying the number of cycles. Depositions were made using 50, 100, 200, 400, and 800 cycles. The time for each individual cycle was precisely 9.02 s.

The measurements of the refractive index and the deposition thickness are shown in figure 7.3. The thickness is linearly dependant on the number of cycles with an R^2 value of 0.9989. It shows that the deposition is constant per cycle. The linear fit has the following form:

$$y = 2 + 0.207x \tag{7.1}$$

where y is the thickness in nanometres and x is the number of cycles. The constant 2 in the equation represents a deposition thickness of 2 nm without any deposition. It is due to the normal oxide layer which is naturally created on a silicone wafer. The slope gives the deposition rate per cycle which is slightly over 2 Å per cycle which is a little higher ALD and PEALD growth rate in literature [141, 193, 194].

The refractive index shows that the films have the refractive index of Al_2O_3 for exposures of more than 200. The smaller refractive index for the sample deposited with 100 and 200 cycles can be due to the very small thickness of the deposition. The ellipsometer used did not have a very high sensitivity, therefore, small film thickness could give a refractive index between the substrate value (1.462) and the Al_2O_3 film value (1.6). The refractive index value for 50 cycles appears to be an anomaly. This small value (1.28) may come from an inherent

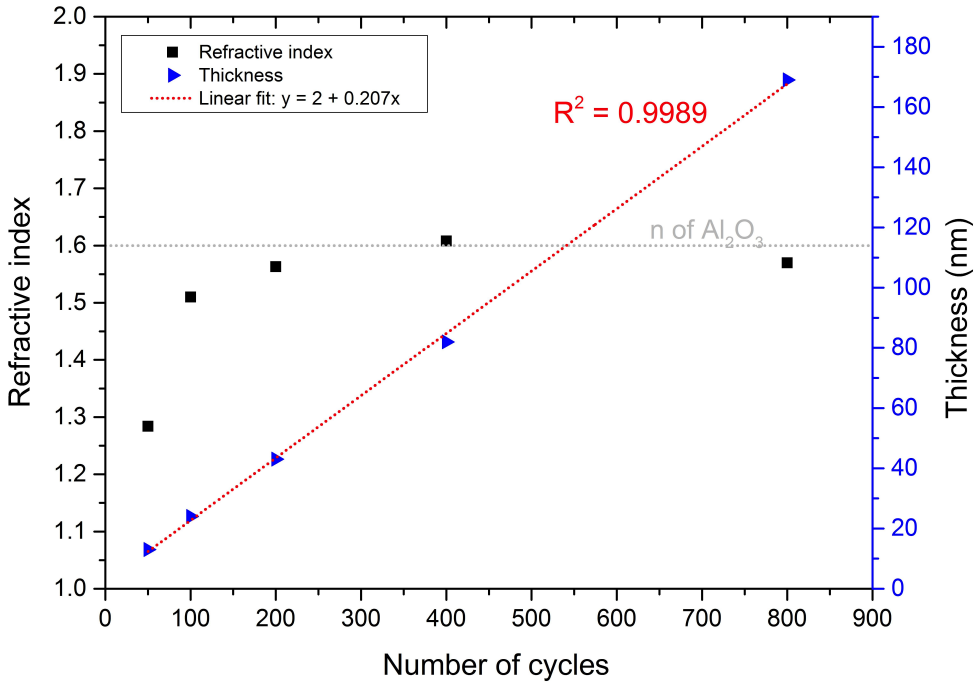

Figure 7.3: Blue triangles represent the thickness in nm of deposition on the silicon wafer. The red line is the linear fit of the thickness values. Black squares are the refractive index measured using ellipsometry, the grey line represents the refractive index of pure alumina with the ellipsometer used.

error on the ellipsometer due to the very small thickness of the film. Tests have been made with similar PEALD conditions without the introduction of the TMA as represented by the green hollow symbols in figure 7.4 and the value stayed similar to the untreated sample (1.462). This value is thus either caused by a small thickness of Al_2O_3 or due to impurities on the sample being mixed with the pure Al_2O_3 film.

Variation of the oxidation step duration

The second study of the PEALD of aluminium oxide involved varying the duration of the oxidation step i.e. the plasma duration. Depositions were made using 200 cycles and 2, 3, 4, 8, and 16 seconds of plasma exposure for each cycle. The respective duration of the depositions can be given by $200(n+6.02)$ s where n is the plasma step duration in s.

The goal was to observe a saturation curve, for that the thickness needs to

logarithmically increase as a function of the oxidation step duration. However, the result shown in figure 7.4 does not have the desired trend. Where the refractive index is concerned (represented by squares), it can be seen that even for a 2 s duration of the oxidation plasma step, the refractive index has the same value as that of Al_2O_3. This proves that even for a small plasma oxidation step of 2 s the deposited film is probably made of a homogeneous Al_2O_3.

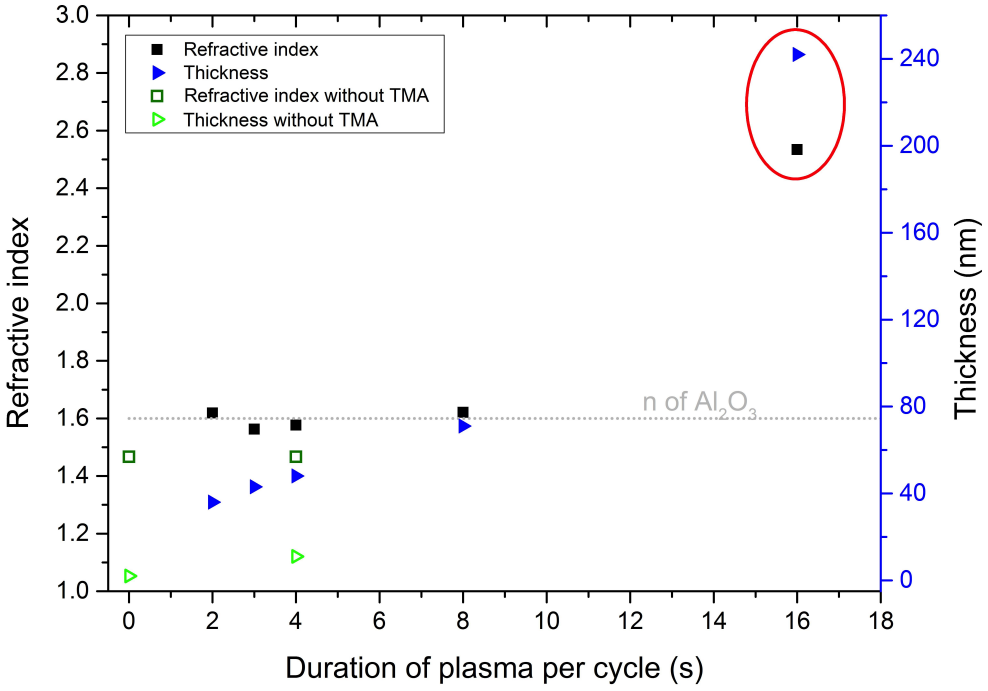

Figure 7.4: Blue triangles represent the thickness in nm of deposition on the silicon wafer. Black squares are the refractive index measured using ellipsometry, grey line represents the refractive index of pure alumina with the ellipsometer used. Green squares and triangles at 0 s are non-treated data, and at 4 s have been made without TMA injection.

The two green hollow squares are samples made to show the effect of the plasma only without the precursor TMA. The first one with no plasma exposure is an untreated sample showing the refractive index of silicon and a thickness of 2 nm (green hollow triangle). The second green hollow square and triangle shows the thickness and refractive index of a sample which was put in the ALD chamber for 200 cycles, however, no TMA was flowed into the chamber. The refractive index shows that 200 cycles of 4 s of plasma did not modify the surface of the sample. The thickness is slightly higher than the untreated sample, ∼10 nm. One

explanation is the low sensitivity of the ellipsometer for thicknesses below 20 nm.

The thickness as a function of the duration of plasma per cycle is almost linear. To have a typical ALD growth, the trend should be logarithmic. This could mean that the saturation is not reached even with 8 s of plasma exposure per cycle. This could also imply that CVD appears on the oxidation steps. As the chamber is used to deposit other material such as gallium nitride, one explanation is that for a long duration of the plasma step, the plasma etched the wall of the chamber, these sputtered particles could then be deposited on the substrate. It would be interesting to redo the experiment on a clean ALD chamber.

The data at 16 s are very surprising and are put on this chart to not hide all the measurements made on this PEALD reactor. The thickness is far much higher than expected and the refractive index value does not correspond to any expected material such as silicon or Al_2O_3. This is most likely an anomaly, and unfortunately due to time constraint, no duplication of these results were made and thus it is not known if the value (200 nm and refractive index of 2.5) are reproducible or not.

7.4 Conclusions

Using a custom-built surface discharge reactor, PEALD at room temperature of Al_2O_3 on a silicon wafer has been performed. Producing ALD at this temperature is only possible due to the plasma assisted oxidation step. Two analyses have been made using this PEALD device.

The first analysis was made by keeping the cycle constant and varying the number of cycles from 50 to 800. The result of this first study shows that the thickness trend is a linear progression allowing the calculation of the deposition rate in nm per cycle. A deposition rate of just over 2 Å per cycle was calculated using a plasma oxidation step of 3 s. It also corresponds to a deposition of $\sim$13.3 nm per minute.

Then the number of cycles was kept at 200 and the oxidation step was varied from 2 to 16 s. A logarithmic saturation curve was not observed. A saturation curve shows the shortest time needed for the oxidation step and proves that the deposition mechanism is one from ALD and not from CVD. The results of the second analysis produces a curve which was linear and a thickness and refractive

index for the 16 s duration which was abnormal. Further deposition should be made for different durations of plasma steps to confirm or refute the measurement of the 16 s.

It has been seen by calculating the deposition rate per cycle and the refractive index of the silicon sample that the system is depositing Al_2O_3 most likely via the ALD mechanism. It has been noted that the plasma duration should be kept short, preferably under 8 s to avoid undesirable deposition. Additionally more depositions should be performed using different oxidation steps in order to verify if the linearity of curve of thickness as a function of plasma step is due to an artefact or not.

Chapter 8

Conclusions

In this thesis the design, the building, the operation, and the analysis of different plasma deposition techniques, polymerisation using atmospheric-pressure plasma jets, and plasma-enhanced atomic layer deposition using a surface discharge reactor, have been performed. This research has allowed an additional step in the understanding of atmospheric-pressure plasma polymerisation, and shown that an existing ALD system can easily be upgraded to a plasma-enhanced ALD system with a simple setup.

8.1 Summary

8.1.1 Polymerisation using Atmospheric-Pressure Plasma Jet

Time-resolved and time-averaged measurements of polymerisation of heptylamine and acrylic acid have been detected using a mass spectrometer. Results show good polymerisation in terms of quantity and quality with variation of intensity as a function of duty cycle and frequency. Heavy polymer ions up to $[6M+H]^+$ have been detected. By-product ions are also present which are a combination of molecules in the surrounding air and polymer fragments. Time-resolved measurements have shown the importance of the duty cycle and the frequency especially for the negative ions. The polymers ions are formed after the plasma bullet, i.e. in the bullet tail where the energy of the molecules is lower. The measurements have also reinforce the step-growth formation theory of plasma polymers.

Although protonoted oligomers as complex as $[6M+H]^+$ have been detected,

deposition analyses did not show very good retention of polymers. There are several possible explanations for this which could explain the reason for the poor quality of deposition. Firstly, the plasma jet alters the deposition by fragmenting the deposited polymers. Secondly, as explained in section 6.4.2 the XPS analysis might have been performed on an area which did not contain the maximum amount of polymers. Another explanation is that the duration between the deposition and the analyses was not optimal which left time for the coating to deteriorate, the transport could also have affected the samples. Finally, as cited in [87], ions seem to contain a high percentage of heavy polymers, however, neutrals mainly contain monomers. As a non-thermal plasma is mainly composed of neutrals, this can lead to a low total number of oligomers which can be reflected by the deposition composition.

8.1.2 Plasma-Enhanced Atomic Layer Deposition

The goal of PEALD deposition at room temperature has been achieved showing promising results. Atomic layer deposition of Al_2O_3 has been performed using a mixture of argon and air plasma created by a simple surface discharge reactor and TMA. Conventional ALD deposition using TMA and water vapour are normally performed at 300 °C, in this thesis the temperature of the chamber was 50 °C.

The results are promising and could lead to the development of an add-on for an existing ALD machine. More experiments and tests must be performed to be able to prove the reliability of the system. The cheap material of the reactor (acrylic and aluminium tape) is a good advantage allowing the users to purchase several similar lids and using them successively. In this way, it would be possible to perform cleaning of a used plasma lid whilst continuing operation with a different one. The plasma parameters can be varied slightly to optimise the deposition for different gases and materials.

8.2 Scope for Future Work

This section presents the domains which require further development in atmospheric-pressure plasma polymerisation using a DBD jet and on PEALD.

8.2.1 Atmospheric-Pressure Plasma Polymerisation

Using the same apparatus as in this thesis further measurements can be performed. First of all, different frequencies and duty cycles could be used to investigate their effect on the polymerisation of acrylic acid. Furthermore, new polymers could be studied such as allylamine or styrene which are common molecules used in low-pressure plasma polymerisation. Deposition using different plasma parameters and different substrate materials could be performed and analysed. Varying the size of the inner diameter of the glass tube could also help to understand the effect of gas velocity on the polymerisation. Other properties of deposited samples should be also analysed, such as adhesion, gas barrier, or hydrophobicity.

Atmospheric-pressure plasma polymerisation is a novel technique which has a lot to prove before being used commonly in industry. The advantages of the technology, such as the absence of an expensive vacuum system, have to compensate the lower deposition quality actually encountered. The small deposition area and the small size of the setup can also be an advantage for some applications.

To be able to mitigate some of the effects of the low retention of poly(acrylic) acid some solutions are proposed to improve future depositions of samples.

- The plasma jet should be operated with lower power.
- XPS should be performed on different points on the samples.
- Deposition should be made on different materials to see the effect of the substrate on the deposition.
- Surface analysis should be performed as soon as possible after the deposition is made or on samples made at different times, to see if this has an effect.

8.2.2 PEALD

The PEALD system design could be improved. First of all, a larger substrate could be used to see how homogeneous the deposition is. Then different electrode configurations could be tested to see the effect on a larger sample. Oxygen gas mixed with argon should also be used instead of air to avoid nitrogen and other contaminants in the deposition.

Initial results are promising and the device is ideal to perform lab experiment of PEALD. It could be conceivable that with further development a similar system could be transformed into a market product. A new system, inspired by the one used in this thesis, has recently been constructed. The electronics have been miniaturised and an LCD display added to make it more user-friendly. This prototype is being tested in Liverpool and is a collaboration between the department of EEE and the Centre for Materials and Structures.

Appendix A

A.1 Debye Shielding

This section is mostly taken from [1] and [195]. The edge of the screening cloud is situated at the region where the potential energy of the particles is approximately equal to the thermal energy of the particles. In order to find the size of this charge screening cloud, let a fixed particle of positive charge q be placed in the middle of a plasma. Before the perturbation, the plasma is globally neutral such that $n_e \approx n_I \approx n_0$. This new charge attracts electrons and repels positive ions. The potential ϕ is calculated for this case. The electron and ion distribution functions are

$$f(u) = \mathrm{A} \exp\left(-\frac{\frac{1}{2}mu^2 + q\phi}{kT}\right) \tag{A.1}$$

where A is a constant, m and q the mass and the charge of the particle, respectively, $\frac{1}{2}mu^2$ is the kinetic energy, and $q\phi$ is the electric potential energy. The electron and ion densities are given by

$$n_{e,i} = \int f(u)\mathrm{du} \tag{A.2}$$

Therefore, the density is $n_{e,i} = \mathrm{C}\exp(-q\phi/kT)$. When ϕ is zero, meaning their is no additional charge, then the density is n_0, thus $n_{e,i} = \mathrm{n}_0 \exp(\pm e\phi/kT)$.

Gauss's Law can be written as

$$\nabla \cdot \mathbf{E} = \frac{\rho}{\varepsilon_0} \tag{A.3}$$

where ρ is the charge density and ε_0 the electric constant. Because there is no magnetic field $\mathbf{E} = -\nabla\phi$, thus (A.3) becomes

$$-\nabla^2\phi = \frac{\rho}{\varepsilon_0} \tag{A.4}$$

which is Poisson's equation. The charge density is

$$\begin{aligned}\rho &= e(n_i - n_e) \\ &= e\mathrm{n}_0 \left(\exp(-e\phi/kT) - \exp(e\phi/kT)\right).\end{aligned}$$

It is assumed that $e\phi << kT$, thus the exponential can be developed using the Taylor series. The charge density becomes

$$\begin{aligned}\rho &= e\mathrm{n}_0 \left(1 - \frac{e\phi}{kT} - 1 - \frac{e\phi}{kT} + O\left(\left[\frac{e\phi}{kT}\right]^3\right)\right) \\ &\cong -e\mathrm{n}_0 \frac{2e\phi}{kT}\end{aligned} \tag{A.5}$$

Finally equation (A.4) becomes

$$-\nabla^2\phi = \frac{-2\mathrm{n}_0 e^2\phi}{\varepsilon_0 kT} \tag{A.6}$$

Using the spherical coordinates assuming spherical symmetry equation (A.6) can be written as follows

$$-\frac{1}{r^2}\frac{\mathrm{d}}{\mathrm{d}r}\left(r^2\frac{\mathrm{d}\phi}{\mathrm{d}r}\right) = \frac{-2\mathrm{n}_0 e^2\phi}{\varepsilon_0 kT} \tag{A.7}$$

The solution is

$$\phi = \phi_0 \exp\left(-\frac{\sqrt{2}r}{\lambda_D}\right) \quad \text{where} \quad \lambda_D = \sqrt{\frac{\varepsilon_0 kT}{e^2\mathrm{n}_0}} \tag{A.8}$$

where $\phi_0 = q/(4\pi\varepsilon_0 r)$ which is the potential created by the charge q. Thus beyond a few Debye lengths, shielding by the plasma is quite effective and the potential due to the charge q is negligible.

A.2 Transit Time

Calculation of transit time made by Yolanda Aranda-Gonzalvo from HIDEN.

For positive ions SIMS

$$t_1 = \mathrm{L}_1 \cdot \frac{\sqrt{2\mathrm{M}m_\mathrm{p}}}{\sqrt{e(\mathrm{Energy} + |\mathrm{Extractor}|)} + \sqrt{e|\mathrm{Axis}|}} \tag{A.9}$$

$$t_2 = \mathrm{L}_2 \cdot \frac{\sqrt{\mathrm{M}m_\mathrm{p}}}{\sqrt{2e|\mathrm{Axis}|}} \tag{A.10}$$

$$t_3 = \mathrm{L}_3 \cdot \frac{\sqrt{\mathrm{M}m_\mathrm{p}}}{\sqrt{2e|\mathrm{Transit\text{-}energy}|}} \tag{A.11}$$

$$t_4 = \mathrm{L}_4 \cdot \frac{\sqrt{2\mathrm{M}m_\mathrm{p}}}{\sqrt{e|\mathrm{First\text{-}dynode}|}} \tag{A.12}$$

$$\mathrm{Transit\ time} = t_1 + t_2 + t_3 + t_4 \tag{A.13}$$

where e is the electric charge, m_p the proton mass, M the molecule mass, and Energy, Extractor, Axis, Transit-energy, and First-dynode, are values from mass spectrometer and L_1, L_2, L_3, and L_4 are dimensions of mass spectrometer parts. Transit time is given in μs.

A.3 SIMS Values on the Mass Spectrometer

The pages 116 to 120 show examples of mass spectrometer values for negative, positive SIMS, and RGA (neutral), for time-averaged and time-resolved measurements.

Example of negative SIMS values on the mass spectrometer:										
4488	scans	53	DataLength							
header	45	lines								
Date	29/05/2014	Time	10:29:26							
ID	HAL 7 EQP LOW ENERGY #13860	Version	3							
Scans	1									
Scan ID	Mode	Input	Scanned	Start	Stop	Increment	Dwell	Settle	RS	RelSEM
Scan 1	-ion SIMS	SEM	mass	1	300	0.2	100	100 %	1	1
Environment										
Global	-ion SIMS									
1st-dynode	2000	V								
CRV_range	7	c/s								
CRV_resolution	6	bits								
D.C.quad	-94	%								
F1	0	(1 = on, 0 = off)								
F2	0	(1 = on, 0 = off)								
axis	40	V								
background_delay	0.1	uS								
background_invert	0	(0 = normal, 1 = invert)								
cage	0	V								
cone1	0	V								
cone2	14	V								
cone3	390	V								
delta-m	0	%								
discriminator	-10	%								
electron-energy	70	V								
emission	0.2	uA								
energy	13.4	V								
extractor	59	V								
flight-focus	78	V								
focus2	306	V								
foreground_delay	0.5	uS								
foreground_invert	0	(0 = normal, 1 = invert)								
gate_width	3	uS								
gating	0	(1 = on, 0 = off)								
horiz	-51	%								
lens1	292	V								
lens2	133	V								
mass	32	amu								
mode-change-delay	1000	ms								
multiplier	2200	V								
plates	-7.27	V								
resolution	0	%								
source-focus	200	V								
transit-energy	-3	V								
vert	-67	%								
Data	1									

Example of positive SIMS values on the mass spectrometer:										
7488	scans	53	DataLength							
header	45	lines								
Date	22/05/2014	Time	11:07:31							
ID	HAL 7 EQP LOW ENERGY #13860	Version	3							
Scans	1									
Scan ID	Mode	Input	Scanned	Start	Stop	Increment	Dwell	Settle	RS	RelSEM
Scan 1	+ion SIMS	SEM	mass	1	500	0.2	100	100 %	1	1
Environment										
Global	+ion SIMS									
1st-dynode	-1'200	V								
CRV_range	7	c/s								
CRV_resolution	6	bits								
D.C.quad	13	%								
F1	0	(1 = on, 0 = off)								
F2	0	(1 = on, 0 = off)								
axis	-40	V								
background_delay	0.1	uS								
background_invert	0	(0 = normal, 1 = invert)								
cage	0	V								
cone1	0	V								
cone2	1	V								
cone3	-678	V								
delta-m	0	%								
discriminator	-15	%								
electron-energy	0	V								
emission	0.2	uA								
energy	2	V								
extractor	-87	V								
flight-focus	-173	V								
focus2	-305	V								
foreground_delay	0.1	uS								
foreground_invert	0	(0 = normal, 1 = invert)								
gate_width	1	uS								
gating	0	(1 = on, 0 = off)								
horiz	-10	%								
lens1	-269	V								
lens2	-181	V								
mass	28	amu								
mode-change-delay	1000	ms								
multiplier	2000	V								
plates	7.27	V								
resolution	0	%								
source-focus	0	V								
transit-energy	3	V								
vert	34	%								
Data	1									

Example of RGA values on the mass spectrometer:										
5988	scans	53	DataLength							
header	45	lines								
Date	05/09/2014	Time	10:14:58							
ID	HAL 7 EQP LOW ENERGY #13860	Version	3							
Scans	1									
Scan ID	Mode	Input	Scanned	Start	Stop	Increment	Dwell	Settle	RS	RelSEM
Scan 1	RGA	SEM	mass	1	400	0.2	100	100 %	1	1
Environment										
Global	RGA									
1st-dynode	-1'200	V								
CRV_range	7	c/s								
CRV_resolution	6	bits								
D.C.quad	22	%								
F1	1	(1 = on, 0 = off)								
F2	0	(1 = on, 0 = off)								
axis	-40	V								
background_delay	0.1	uS								
background_invert	0	(0 = normal, 1 = invert)								
cage	3	V								
cone1	0	V								
cone2	-59	V								
cone3	166	V								
delta-m	0	%								
discriminator	-15	%								
electron-energy	70	V								
emission	20	uA								
energy	0	V								
extractor	-190	V								
flight-focus	-155	V								
focus2	-288	V								
foreground_delay	0.1	uS								
foreground_invert	0	(0 = normal, 1 = invert)								
gate_width	2	uS								
gating	0	(1 = on, 0 = off)								
horiz	0	%								
lens1	159	V								
lens2	-107	V								
mass	28	amu								
mode-change-delay	1000	ms								
multiplier	2000	V								
plates	7.27	V								
resolution	0	%								
source-focus	-238	V								
transit-energy	3	V								
vert	-1	%								
Data	1									

Example of negative SIMS values on the mass spectrometer: (time-resolved)										
81	scans	70	DataLength							
header	48	lines								
Date		Time								
ID	HAL 7 EQP LOW ENERGY #13860	Version	3							
Scans	4									
Scan ID	Mode	Input	Scanned	Start	Stop	Increment	Dwell	Settle	RS	RelSEM
Scan 1	-ion SIMS	SEM	mass	71	71	0.02	50	100 %	1	1
Scan 2	-ion SIMS	SEM	mass	143	143	0.02	50	100 %	1	1
Scan 3	-ion SIMS	SEM	mass	215	215	0.02	50	100 %	1	1
Scan 4	-ion SIMS	SEM	mass	287	287	0.02	50	100 %	1	1
Environment										
Global	-ion SIMS									
1st-dynode	2000	V								
CRV_range	7	c/s								
CRV_resolution	6	bits								
D.C.quad	-94	%								
F1	0	(1 = on, 0 = off)								
F2	0	(1 = on, 0 = off)								
axis	40	V								
background_delay	0.1	uS								
background_invert	0	(0 = normal, 1 = invert)								
cage	0	V								
cone1	0	V								
cone2	14	V								
cone3	390	V								
delta-m	0	%								
discriminator	-10	%								
electron-energy	70	V								
emission	0.2	uA								
energy	13.4	V								
extractor	59	V								
flight-focus	78	V								
focus2	306	V								
foreground_delay	0.5	uS								
foreground_invert	0	(0 = normal, 1 = invert)								
gate_width	5	uS								
gating	1	(1 = on, 0 = off)								
horiz	-51	%								
lens1	292	V								
lens2	133	V								
mass	32	amu								
mode-change-delay	1000	ms								
multiplier	2200	V								
plates	-7.27	V								
resolution	0	%								
source-focus	200	V								
transit-energy	-3	V								
vert	-67	%								
Data	4									

Example of positive SIMS values on the mass spectrometer: (time-resolved)										
26	scans	58	DataLength							
header	47	lines								
Date		Time								
ID	HAL 7 EQP LOW ENERGY #13860	Version	3							
Scans	3									
Scan ID	Mode	Input	Scanned	Start	Stop	Increment	Dwell	Settle	RS	RelSEM
Scan 1	+ion SIMS	SEM	mass	73	73	0.02	60	100 %	1	1
Scan 2	+ion SIMS	SEM	mass	145	145	0.02	60	100 %	1	1
Scan 3	+ion SIMS	SEM	mass	217	217	0.02	60	100 %	1	1
Environment										
Global	+ion SIMS									
1st-dynode	-1'200	V								
CRV_range	7	c/s								
CRV_resolution	6	bits								
D.C.quad	13	%								
F1	0	(1 = on, 0 = off)								
F2	0	(1 = on, 0 = off)								
axis	-40	V								
background_delay	0.1	uS								
background_invert	0	(0 = normal, 1 = invert)								
cage	0	V								
cone1	0	V								
cone2	1	V								
cone3	-678	V								
delta-m	0	%								
discriminator	-15	%								
electron-energy	0	V								
emission	0.2	uA								
energy	2	V								
extractor	-87	V								
flight-focus	-173	V								
focus2	-305	V								
foreground_delay	0.1	uS								
foreground_invert	0	(0 = normal, 1 = invert)								
gate_width	5	uS								
gating	1	(1 = on, 0 = off)								
horiz	-10	%								
lens1	-269	V								
lens2	-181	V								
mass	28	amu								
mode-change-delay	1000	ms								
multiplier	1800	V								
plates	7.27	V								
resolution	0	%								
source-focus	0	V								
transit-energy	3	V								
vert	34	%								
Data	3									

A.4 Resolution of the Contacless Electrostatic Probe

Figure A.1 shows the resolution of the contactless electrostatic probe of the model 347, 6000B-5C. The graph gives either the area of collection with a good resolution or the resolution for a certain spot size. These values are given as function of the distance between the tip of the probe and the surface.

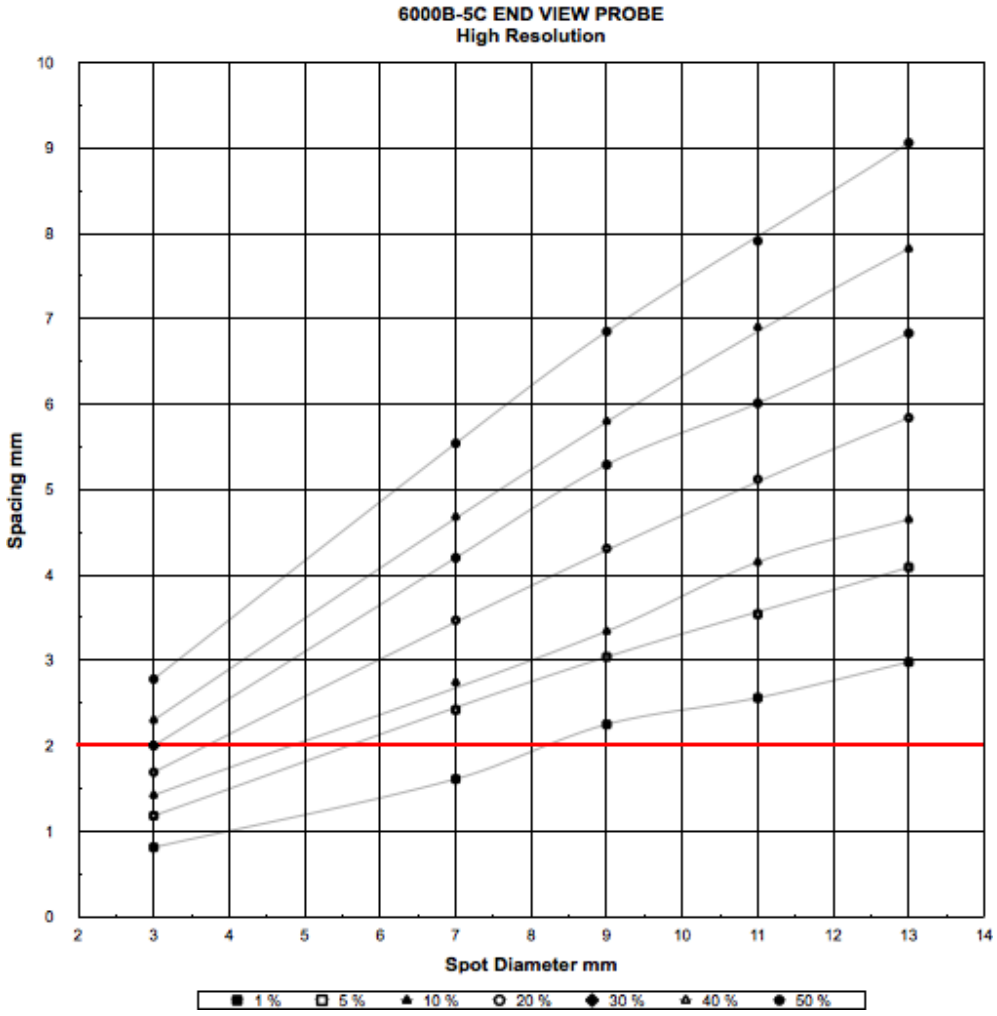

Figure A.1: Resolution of the contacless electrostatic probe. Information provided by TREK INC.

A.5 RGA Spectrum of Acrylic Acid Plasma Jet

Figure A.2 shows an RGA spectrum of acrylic acid plasma jet.

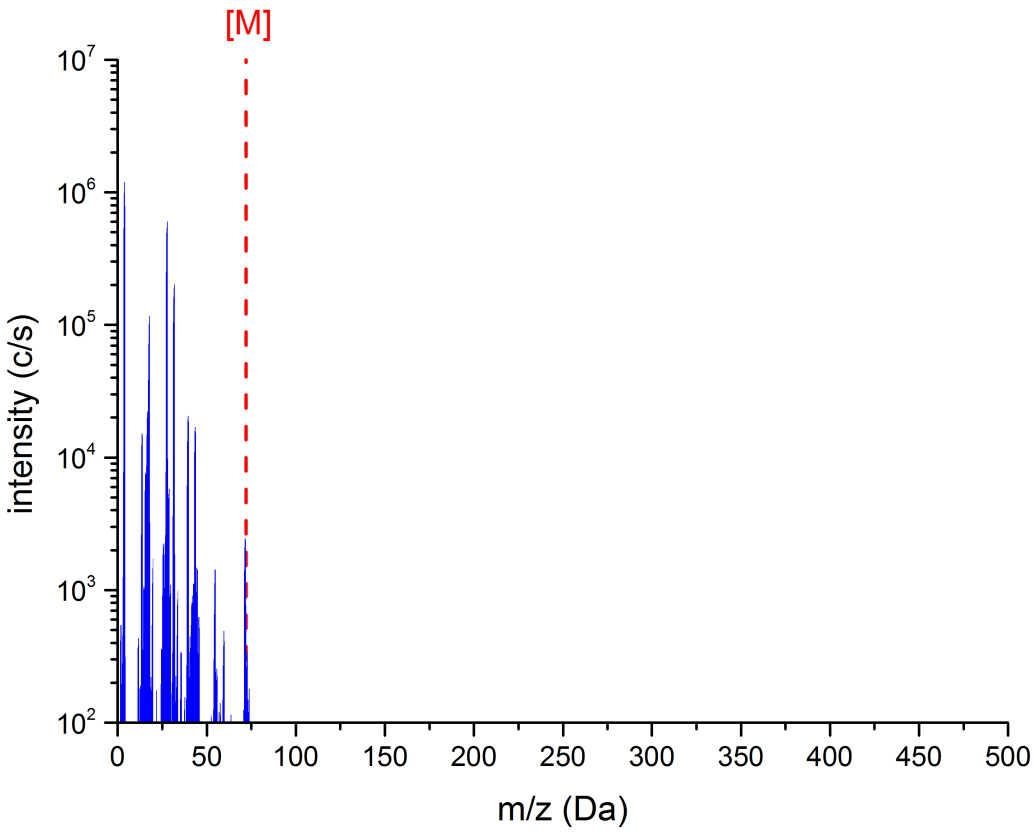

Figure A.2: RGA spectrum of acrylic acid using a pulsed DC signal of 5 kHz, and 4 kV

A.6 Voltage as a Function of the Duty Cycle

Figure A.3 shows the voltage using different duty cycles. The power supply was showing the same value for each of the lines shown in the figure.

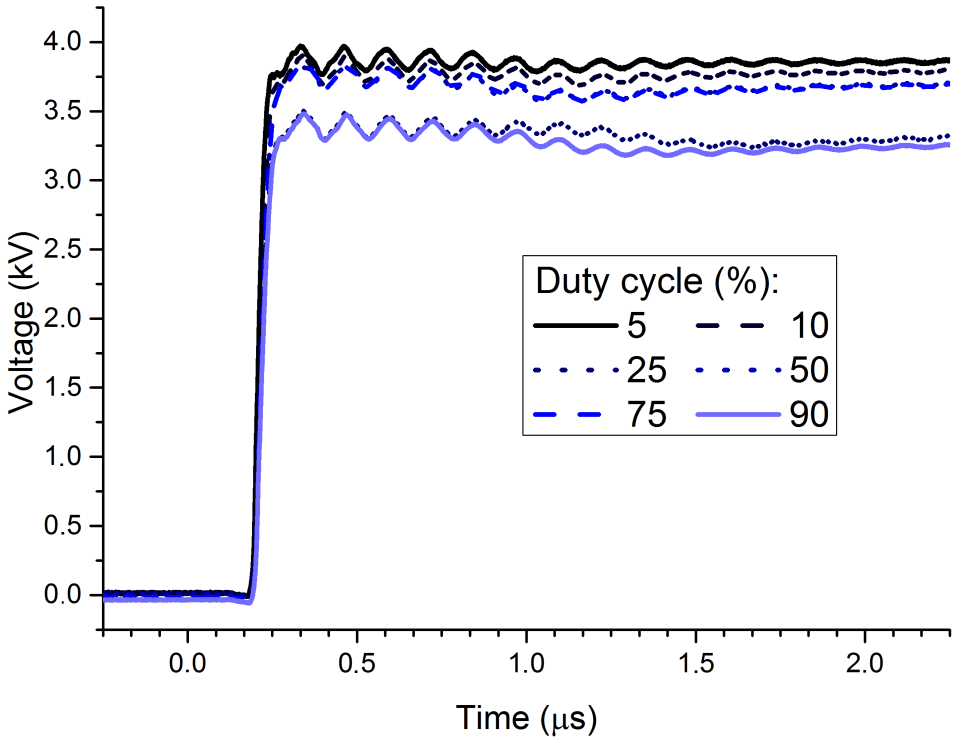

Figure A.3: A plot of the rising edge of the voltage for different duty cycles for a positive pulsed DC signal of 5 kHz.

A.7 By-products from Plasma Polymerisation of Acrylic Acid

Figure A.4 in the next page shows a few possible by-product molecules formed by the atmospheric-pressure plasma polymerisation of acrylic acid.

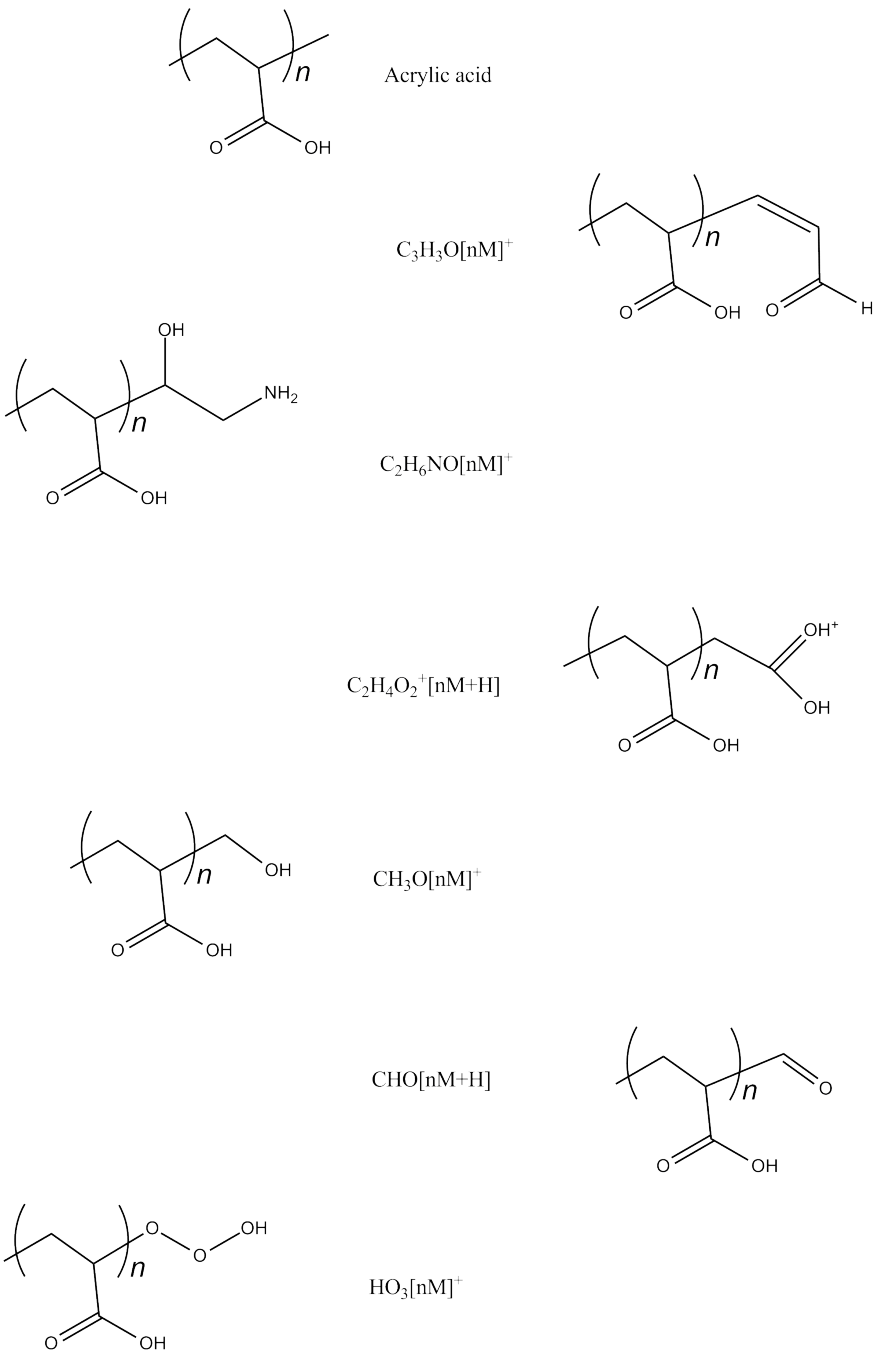

Figure A.4: Possible by-product molecules coming from plasma polymerisation of acrylic acid (M = acrylic acid).

A.8 TOF-SIMS Spectra

The pages 127 to 131 show positive ions TOF-SIMS spectra. There are printed in alphabetic order from A to E with the letter corresponding to the image in figure 6.8

File: LIV_C1_0.ita	Date: Mon Oct 06 15:25:16 2014	Polarity: **Positive**
Sample Info: **Sample:** Comment: Origin:		Primary Beam: Species: Bi3 Area: 500 x 500 µm² Dose:

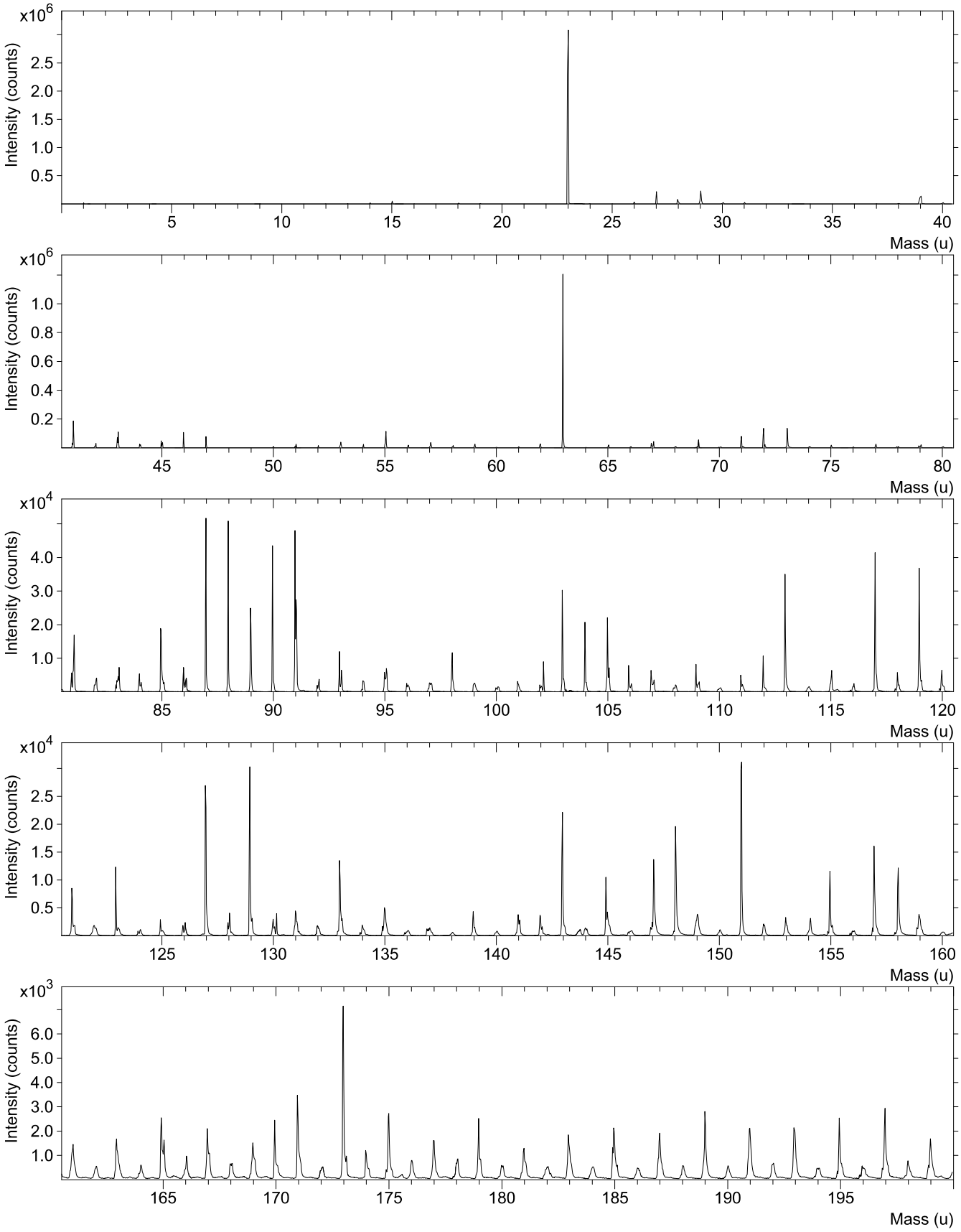

File: LIV_A1_0.ita	Date: Mon Oct 06 14:31:08 2014	Polarity: **Positive**
Sample Info: **Sample:** Comment: Origin:		Primary Beam: Species: Bi3 Area: 500 x 500 µm² Dose:

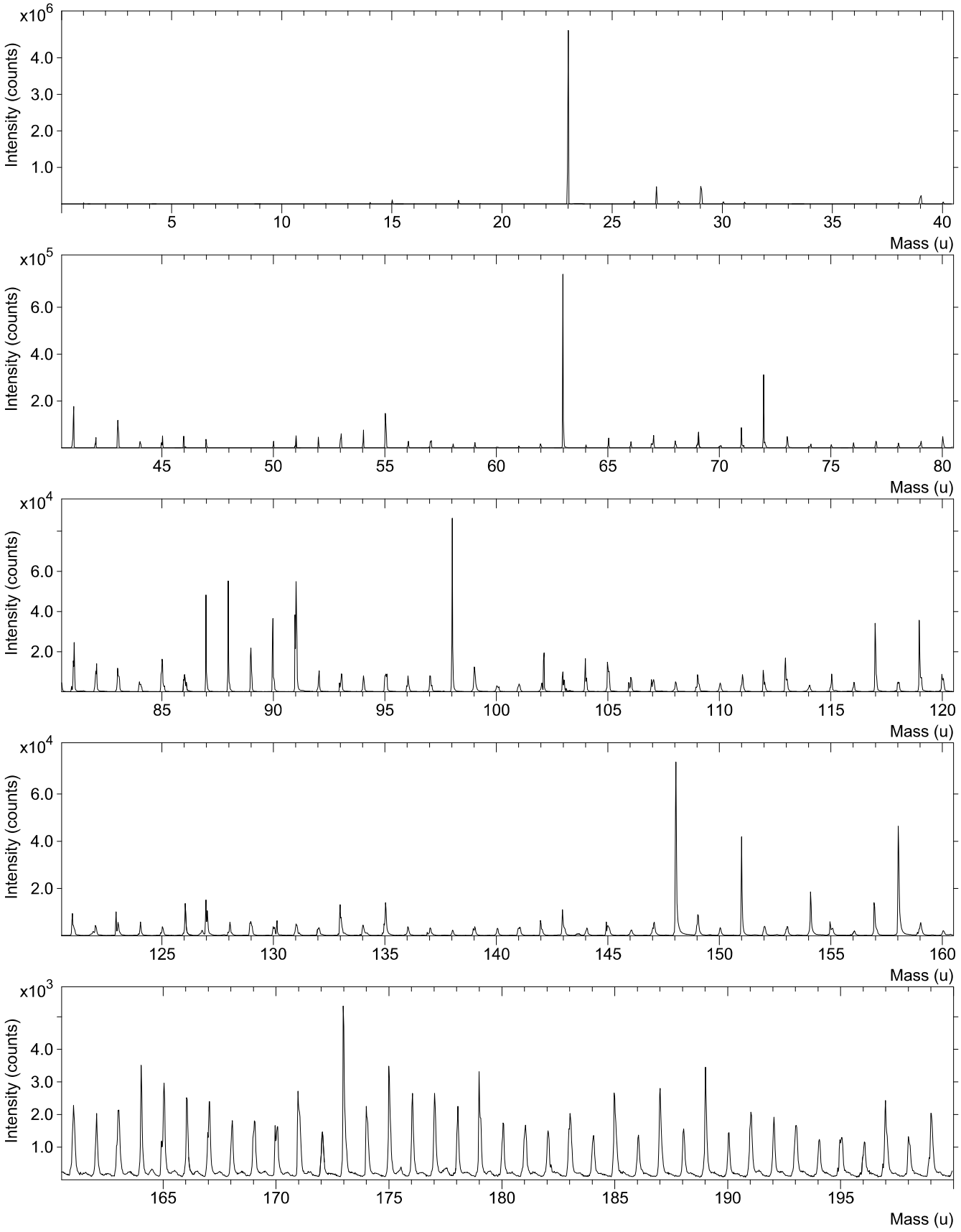

File: LIV_E_0.ita	Date: Mon Oct 06 15:38:30 2014	Polarity: **Positive**
Sample Info: **Sample:** Comment: Origin:		Primary Beam: Species: Bi3 Area: 500 x 500 µm² Dose:

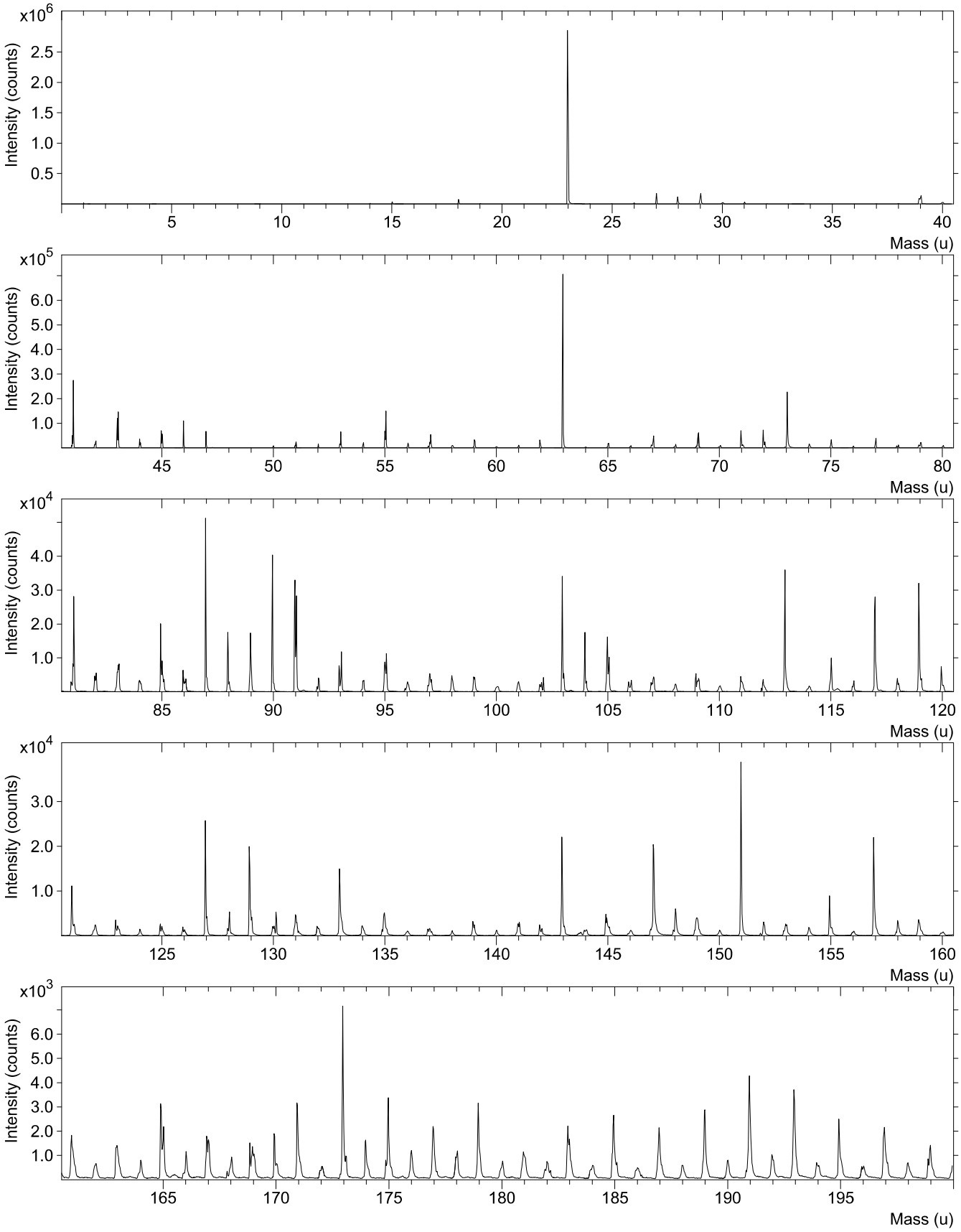

File: LIV_B1_0.ita	Date: Mon Oct 06 14:48:25 2014	Polarity: **Positive**
Sample Info: **Sample:** Comment: Origin:		Primary Beam: Species: Bi3 Area: 500 x 500 µm² Dose:

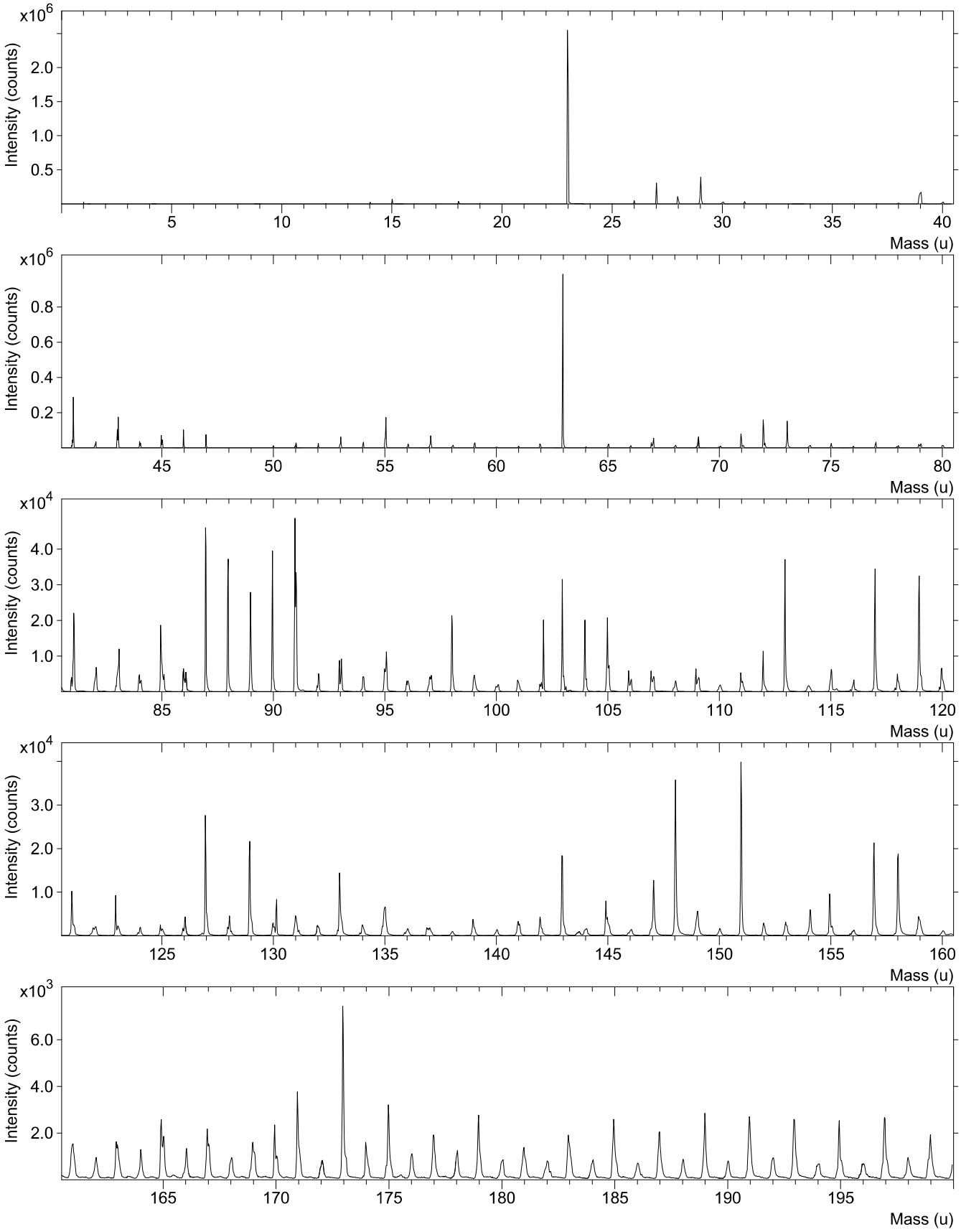

File: LIV_D1_0.ita	Date: Mon Oct 06 15:01:39 2014	Polarity: **Positive**
Sample Info: **Sample:** Comment: Origin:		Primary Beam: Species: Bi3 Area: 500 x 500 µm² Dose:

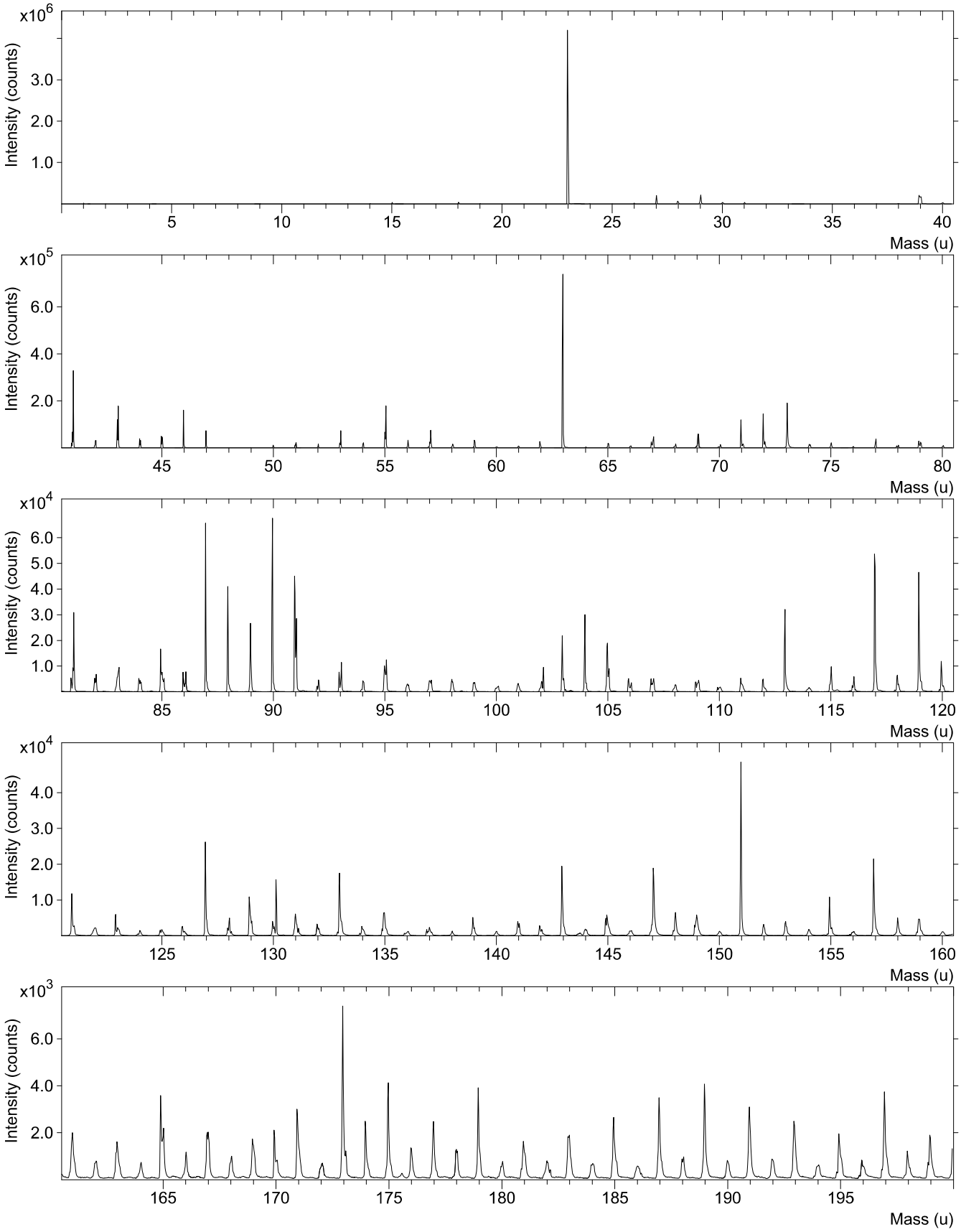

Bibliography

[1] F. F. Chen, *Introduction to Plasma Physics and Controlled Fusion*. Boston, MA: Springer US, 2 ed., 1984.

[2] J. Meek and J. Craggs, *Electrical breakdown of gases*. Oxford University Press, 1953.

[3] E. H. R. Gaxiola, *Dielectric Breakdown in Insulating Gases: Space Charge Effects and Non-Uniform Fields*. Eindhoven: Eindhoven University Press, 1999.

[4] P. Bellan, *Fundamentals of Plasma Physics*. Cambridge University Press, 2006.

[5] D. Korzec, E. G. Finantu-Dinu, M. Teschke, J. Engemann, M. Miclea, K. Kunze, J. Franzke, and K. Niemax, "Characterization of a surface barrier discharge in helium," *Plasma Sources Science and Technology*, vol. 15, no. 3, pp. 345–359, 2006.

[6] F. F. Chen and M. D. Smith, *Plasma*. John Wiley and Sons, Inc., 2005.

[7] T. Martens, *Numerical simulations of dielectric barrier discharges*. Universiteit Antwerpen, 2010.

[8] P. Diamond, S. Itoh, and K. Itoh, *Modern Plasma Physics: Volume 1, Physical Kinetics of Turbulent Plasmas*. Cambridge University Press, 2010.

[9] R. Cairns, *Plasma Physics*. Springer Netherlands, 2012.

[10] Y. Wu, J. Jiang, M. Wang, and M. Jin, "A fusion-driven subcritical system concept based on viable technologies," *Nuclear Fusion*, vol. 51, p. 103036, Oct. 2011.

[11] A. V. Melnikov, C. Hidalgo, T. Ido, A. Shimizu, A. Fujisawa, K. S. Dyabilin, and S. E. Lysenko, "Plasma Potential in Toroidal Devices: T-10, TJ-II, CHS and LHD," *Plasma and Fusion Research*, vol. 7, p. 2402114, 2012.

[12] W. Stacey, *Fusion Plasma Physics*. Physics textbook, Wiley, 2012.

[13] P. Poolcharuansin, M. Bowes, T. J. Petty, and J. W. Bradley, "Ionized metal flux fraction measurements in HiPIMS discharges," *Journal of Physics D: Applied Physics*, vol. 45, p. 322001, Aug. 2012.

[14] M. Bowes, P. Poolcharuansin, and J. W. Bradley, "Negative ion energy distributions in reactive HiPIMS," *Journal of Physics D: Applied Physics*, vol. 46, p. 045204, Jan. 2013.

[15] M. Bowes and J. W. Bradley, "The behaviour of negative oxygen ions in the afterglow of a reactive HiPIMS discharge," *Journal of Physics D: Applied Physics*, vol. 47, p. 265202, July 2014.

[16] M. Bowes and J. W. Bradley, "Inert gas effects on the deposition rate of TiO2 during reactive HiPIMS," *Surface and Coatings Technology*, vol. 250, pp. 2–6, July 2014.

[17] S. Rauf and M. J. Kushner, "Dynamics of a coplanar-electrode plasma display panel cell. I. Basic operation," *Journal of Applied Physics*, vol. 85, no. 7, pp. 3460–3469, 1999.

[18] S. Rauf and M. J. Kushner, "Dynamics of a coplanar-electrode plasma display panel. II. Cell optimization," *Journal of Applied Physics*, vol. 85, no. 7, pp. 3470–3476, 1999.

[19] S. Rauf and M. J. Kushner, "Operation of a coplanar-electrode plasma display panel cell," *IEEE Transactions on Plasma Science*, vol. 27, no. 1, pp. 10–11, 1999.

[20] R. Ganter, J. Ouyang, T. Callegari, and J. P. Boeuf, "Physical phenomena in a coplanar macroscopic plasma display cell I. Infrared and visible emission," *Journal of Applied Physics*, vol. 91, no. 3, p. 992, 2002.

[21] V. I. Gibalov and G. J. Pietsch, "Properties of dielectric barrier discharges in extended coplanar electrode systems," *Journal of Physics D-Applied Physics*, vol. 37, no. 15, pp. 2093–2100, 2004.

[22] S. B. Shim, I. C. Song, and H. J. Lee, "The effect of electrode tilt angle on the characteristics of coplanar dielectric barrier discharges with Xe-Ne mixtures," *Journal of Applied Physics*, vol. 110, no. 2, 2011.

[23] K. Fricke, I. Koban, H. Tresp, L. Jablonowski, K. Schröder, A. Kramer, K.-D. Weltmann, T. von Woedtke, and T. Kocher, "Atmospheric pressure plasma: a high-performance tool for the efficient removal of biofilms.," *PloS one*, vol. 7, p. e42539, Jan. 2012.

[24] S. MacNeil, "Progress and opportunities for tissue-engineered skin.," *Nature*, vol. 445, pp. 874–80, Feb. 2007.

[25] A. Sarani, N. De Geyter, A. Y. Nikiforov, R. Morent, C. Leys, J. Hubert, and F. Reniers, "Surface modification of PTFE using an atmospheric pressure plasma jet in argon and argon+CO2," *Surface and Coatings Technology*, vol. 206, no. 8-9, pp. 2226–2232, 2012.

[26] D. Puleo and A. Nanci, "Understanding and controlling the bone-implant interface," *Biomaterials*, vol. 20, 1999.

[27] "Low-pressure plasma polymer deposition (plasmatreat)." `http://www.plasmatreat.com/company/partners_references/research-development/success-story-protect-select.html`. Accessed: 2016-01-9.

[28] A. Harsch, J. Calderon, R. Timmons, and G. Gross, "Pulsed plasma deposition of allylamine on polysiloxane: a stable surface for neuronal cell adhesion," *Journal of Neuroscience Methods*, vol. 98, pp. 135–144, June 2000.

[29] R. Morent, N. De Geyter, F. Axisa, N. De Smet, L. Gengembre, E. De Leersnyder, C. Leys, J. Vanfleteren, M. Rymarczyk-Machal, E. Schacht, and E. Payen, "Adhesion enhancement by a dielectric barrier discharge of

PDMS used for flexible and stretchable electronics," *Journal of Physics D: Applied Physics*, vol. 40, pp. 7392–7401, Dec. 2007.

[30] M. Donegan and D. P. Dowling, "Protein adhesion on water stable atmospheric plasma deposited acrylic acid coatings," *Surface and Coatings Technology*, vol. 234, pp. 53–59, Mar. 2013.

[31] R. F. Bunshah, *Handbook of deposition technologies for films and coatings : science, application and technology (3rd Edition)*. Park Ridge, N.J.: Noyes Publications, 2nd ed., 2010.

[32] P. Poodt, B. Kniknie, A. Branca, H. Winands, and F. Roozeboom, "Patterned deposition by plasma enhanced spatial atomic layer deposition," *Physica Status Solidi-Rapid Research Letters*, vol. 5, no. 4, pp. 165–167, 2011.

[33] F. Moix, K. McKay, J. L. Walsh, and J. W. Bradley, "Atmospheric-Pressure Plasma Polymerization of Acrylic Acid: Gas-Phase Ion Chemistry," *Plasma Processes and Polymers*, July 2015.

[34] M. Lieberman and A. Lichtenberg, *Principles of Plasma Discharges and Materials Processing*. Wiley, 2005.

[35] F. S. Denes and S. Manolache, "Macromolecular plasma-chemistry: an emerging field of polymer science," *Progress in Polymer Science*, vol. 29, no. 8, pp. 815–885, 2004.

[36] D. M. Mattox, *Handbook of Physical Vapor Deposition (PVD) Processing*. William Andrew Publishing/Noyes, 1998.

[37] J. D. Whittle, D. A. Steele, and R. D. Short, "Reconciling the Physical and Chemical Environments of Plasma: A Commentary on Mechanisms of Plasma Polymerisation - Reviewed from a Chemical Point of View," *Plasma Processes and Polymers*, vol. 9, pp. 840–843, Sept. 2012.

[38] F. Paschen, "Ueber die zum funkenbergang in luft, wasserstoff und kohlensure bei verschiedenen drucken erforderliche potentialdifferenz," *Annalen der Physik*, vol. 273, no. 5, pp. 69–96, 1889.

[39] A. Fridman, *Plasma Chemistry*. Cambridge University Press, 2008.

[40] V. I. Gibalov and G. J. Pietsch, "The development of dielectric barrier discharges in gas gaps and on surfaces," *Journal of Physics D-Applied Physics*, vol. 33, no. 20, pp. 2618–2636, 2000.

[41] M. Simor, J. Rahel, P. Vojtek, M. Cernak, A. Brablec, M. Simor, J. Rahel, and M. Cernak, "Atmospheric-pressure diffuse coplanar surface discharge for surface treatments," *Applied Physics Letters*, vol. 81, no. 15, pp. 2716–2718, 2002.

[42] D. Korzec, E. G. Finantu-Dinu, A. Schwabedissen, J. Engemann, J. Rahel, M. Tefecka, Y. Imahori, and M. Kando, "Insulated surface discharge for metastables driven processing at atmospheric pressure," *Surface and Coatings Technology*, vol. 169-170, pp. 228–232, 2003.

[43] G. I. Font, C. L. Enloe, J. Y. Newcomb, A. L. Teague, A. R. Vasso, and T. E. McLaughlin, "Effects of Oxygen Content on Dielectric Barrier Discharge Plasma Actuator Behavior," *American Institue of Aeronautics and Astronautics Journal*, vol. 49, no. 7, pp. 1366–1373, 2011.

[44] L. Hulka and G. J. Pietsch, "Influence of dimensions and materials of coplanar arrangements on ozone production," *Plasma Processes and Polymers*, vol. 2, no. 3, pp. 222–226, 2005.

[45] V. I. Gibalov and G. J. Pietsch, "Dynamics of dielectric barrier discharges in coplanar arrangements," *Journal of Physics D-Applied Physics*, vol. 37, no. 15, pp. 2082–2092, 2004.

[46] D. Korzec, E. G. Finan, G. L. Dinu, J. Engemann, M. Tefecka, and M. Kando, "Comparison of coplanar and surface barrier discharges operated in oxygen-nitrogen gas mixtures," *Surface and Coatings Technology*, vol. 174-175, pp. 503–508, 2003.

[47] M. Tefecka, M. Kando, M. Cernak, D. Korzec, E. G. Finantu-Dinu, G. L. Dinu, and J. Engemann, "Spatial distribution of surface treatment efficiency in coplanar barrier discharge operated with oxygen-nitrogen gas mixtures," *Surface and Coatings Technology*, vol. 174-175, pp. 553–558, 2003.

[48] E. G. Finantu-Dinu, D. Korzec, M. Teschke, and J. Engemann, "Influence of the electrode layout on performance of insulated surface discharge: Electrical characterization," *Surface and Coatings Technology*, vol. 174-175, pp. 524–529, 2003.

[49] R. Spielman, A. Hill, and S. Wilson, "Apparatus for highly efficient cold-plasma ozone production," June 30 2015. US Patent 9,067,788.

[50] R. Gu, J. Yu, C. Hu, L. Chen, J. Zhu, and Z. Hu, "Surface treatment of para-aramid fiber by argon dielectric barrier discharge plasma at atmospheric pressure," *Applied Surface Science*, vol. 258, no. 24, pp. 10168–10174, 2012.

[51] U. Kogelschatz, B. Eliasson, and W. Egli, "Dielectric-barrier discharges. Principle and applications," *Journal de Physique IV*, vol. 7, no. C4, pp. C4–47–C4–66, 1997.

[52] U. Kogelschatz, "Dielectric-barrier discharges: their history, discharge physics, and industrial applications," *Plasma chemistry and plasma processing*, vol. 23, no. 1, pp. 1–46, 2003.

[53] X. C. Bian, Q. Chen, Y. F. Zhang, L. J. Sang, and W. J. Tang, "Deposition of nano-diamond-like carbon films by an atmospheric pressure plasma gun and diagnostic by optical emission spectrum on the process," *Surface & Coatings Technology*, vol. 202, no. 22-23, pp. 5383–5385, 2008.

[54] I. Vinogradov and A. Lunk, "Film Deposition in the Dielectric Barrier Discharge at Atmospheric Pressure in He/O(2)/HMDSO and He/N(2)O/HMDSO mixtures," *Plasma Processes and Polymers*, vol. 6, pp. S514–S518, 2009.

[55] H. E. Wagner, R. Brandenburg, K. V. Kozlov, A. Sonnenfeld, P. Michel, and J. F. Behnke, "The barrier discharge: basic properties and applications to surface treatment," *Vacuum*, vol. 71, no. 3, pp. 417–436, 2003.

[56] T. Murata, Y. Okita, M. Noguchi, and I. Takase, "Basic parameters of coplanar discharge ozone generator," *Ozone-Science & Engineering*, vol. 26, no. 5, pp. 429–442, 2004.

[57] A.-M. Zhu, L.-H. Nie, Q.-H. Wu, X.-L. Zhang, X.-F. Yang, Y. Xu, and C. Shi, "Crystalline, uniform-sized TiO2 nanosphere films by a novel plasma CVD process at atmospheric pressure and room temperature," *Chemical Vapor Deposition*, vol. 13, no. 4, pp. 141–144, 2007.

[58] H. Nishida and T. Abe, "Numerical analysis of plasma evolution on dielectric barrier discharge plasma actuator," *Journal of Applied Physics*, vol. 110, no. 1, 2011.

[59] J. Cech, P. Stahel, and Z. Navratil, "The influence of electrode gap width on plasma properties of diffuse coplanar surface barrier discharge in nitrogen," *European Physical Journal D*, vol. 54, no. 2, pp. 259–264, 2009.

[60] S.-Z. Li, Q. Wu, W. Yan, D. Wang, and H. S. Uhm, "Influence of oxygen traces on an atmospheric-pressure radio-frequency capacitive argon plasma discharge," *Physics of Plasmas*, vol. 18, no. 10, 2011.

[61] C. Tendero, C. Tixier, P. Tristant, J. Desmaison, and P. Leprince, "Atmospheric pressure plasmas: A review," *Spectrochimica Acta Part B: Atomic Spectroscopy*, vol. 61, pp. 2–30, Jan. 2006.

[62] T. Hoder, R. Brandenburg, R. Basner, K. D. Weltmann, K. V. Kozlov, and H. E. Wagner, "A comparative study of three different types of barrier discharges in air at atmospheric pressure by cross-correlation spectroscopy," *Journal of Physics D: Applied Physics*, vol. 43, no. 12, 2010.

[63] F. Massines, A. Rabehi, P. Decomps, R. B. Gadri, P. Segur, and C. Mayoux, "Experimental and theoretical study of a glow discharge at atmospheric pressure controlled by dielectric barrier," *Journal of Applied Physics*, vol. 83, no. 6, p. 2950, 1998.

[64] R. B. Tyata, D. P. Subedi, A. Shrestha, and D. Baral, "Development of atmospheric pressure plasma jet in air," *Kathmandu University Journal of Science, Engineering and Technology*, vol. 8, no. I, pp. 15–22, 2012.

[65] J. L. Walsh, P. Olszewski, and J. W. Bradley, "The manipulation of atmospheric pressure dielectric barrier plasma jets," *Plasma Sources Science and Technology*, vol. 21, p. 034007, June 2012.

[66] Z. Cao, J. L. Walsh, and M. G. Kong, "Atmospheric plasma jet array in parallel electric and gas flow fields for three-dimensional surface treatment," *Applied Physics Letters*, vol. 94, no. 2, p. 021501, 2009.

[67] J. Y. Jeong, S. E. Babayan, V. J. Tu, J. Park, I. Henins, R. F. Hicks, and G. S. Selwyn, "Etching materials with an atmospheric-pressure plasma jet," *Plasma Sources Science and Technology*, vol. 7, pp. 282–285, Aug. 1998.

[68] S. Förster, C. Mohr, and W. Viöl, "Investigations of an atmospheric pressure plasma jet by optical emission spectroscopy," *Surface and Coatings Technology*, vol. 200, pp. 827–830, Oct. 2005.

[69] M. Noeske, J. Degenhardt, S. Strudthoff, and U. Lommatzsch, "Plasma jet treatment of five polymers at atmospheric pressure: surface modifications and the relevance for adhesion," *International Journal of Adhesion and Adhesives*, vol. 24, pp. 171–177, Apr. 2004.

[70] H. W. Herrmann, I. Henins, J. Park, and G. S. Selwyn, "Decontamination of chemical and biological warfare (CBW) agents using an atmospheric pressure plasma jet (APPJ)," *Physics of Plasmas*, vol. 6, no. 5, p. 2284, 1999.

[71] M. Laroussi and X. Lu, "Room-temperature atmospheric pressure plasma plume for biomedical applications," *Applied Physics Letters*, vol. 87, no. 11, p. 113902, 2005.

[72] K.-D. Weltmann, E. Kindel, R. Brandenburg, C. Meyer, R. Bussiahn, C. Wilke, and T. von Woedtke, "Atmospheric Pressure Plasma Jet for Medical Therapy: Plasma Parameters and Risk Estimation," *Contributions to Plasma Physics*, vol. 49, pp. 631–640, Nov. 2009.

[73] K.-D. Weltmann, R. Brandenburg, T. von Woedtke, J. Ehlbeck, R. Foest, M. Stieber, and E. Kindel, "Antimicrobial treatment of heat sensitive products by miniaturized atmospheric pressure plasma jets (APPJs)," *Journal of Physics D: Applied Physics*, vol. 41, p. 194008, Oct. 2008.

[74] X.-J. Shao, N. Jiang, G.-J. Zhang, and Z.-X. Cao, "Comparative study on the atmospheric pressure plasma jets of helium and argon," *Applied Physics Letters*, vol. 101, no. 25, 2012.

[75] X. Lu, M. Laroussi, and V. Puech, "On atmospheric-pressure non-equilibrium plasma jets and plasma bullets," *Plasma Sources Science and Technology*, vol. 21, p. 034005, June 2012.

[76] J. L. Walsh and M. G. M. Kong, "Contrasting characteristics of linear-field and cross-field atmospheric plasma jets," *Applied Physics Letters*, vol. 93, no. 11, p. 111501, 2008.

[77] J. L. Walsh, F. Iza, N. B. Janson, V. J. Law, and M. G. Kong, "Three distinct modes in a cold atmospheric pressure plasma jet," *Journal of Physics D: Applied Physics*, vol. 43, p. 075201, Feb. 2010.

[78] J.-S. Oh, J. L. Walsh, and J. W. Bradley, "Plasma bullet current measurements in a free-stream helium capillary jet," *Plasma Sources Science and Technology*, vol. 21, p. 034020, June 2012.

[79] Q. Xiong, A. Y. Nikiforov, M. A. González, C. Leys, and X. P. Lu, "Characterization of an atmospheric helium plasma jet by relative and absolute optical emission spectroscopy," *Plasma Sources Science and Technology*, vol. 22, p. 015011, Feb. 2013.

[80] J.-S. Oh, Y. Aranda-Gonzalvo, and J. W. Bradley, "Time-resolved mass spectroscopic studies of an atmospheric-pressure helium microplasma jet," *Journal of Physics D: Applied Physics*, vol. 44, p. 365202, Sept. 2011.

[81] J.-S. Oh, P. M. Bryant, and J. W. Bradley, "Discharge and Plasma Bullet Formation in a Capillary DBD Atmospheric-Pressure Microplasma Jet," *IEEE Transactions on Plasma Science*, vol. 39, pp. 2352–2353, 2011.

[82] J. Walsh and M. Kong, "Frequency effects of plasma bullets in atmospheric glow discharges," *Plasma Science, IEEE Transactions on*, vol. 36, no. 4, pp. 954–955, 2008.

[83] K. McKay, D. X. Liu, M. Z. Rong, F. Iza, and M. G. Kong, "Dynamics and particle fluxes in atmospheric-pressure electronegative radio frequency microplasmas," *Applied Physics Letters*, vol. 99, no. 9, p. 091501, 2011.

[84] K. McKay, D. X. Liu, M. Z. Rong, F. Iza, and M. G. Kong, "Generation and loss of reactive oxygen species in low-temperature atmospheric-pressure RF He+O2+H2O plasmas," *Journal of Physics D: Applied Physics*, vol. 45, p. 172001, May 2012.

[85] K. McKay, J. L. Walsh, and J. W. Bradley, "Observations of ionic species produced in an atmospheric pressure pulse-modulated RF plasma needle," *Plasma Sources Science and Technology*, vol. 22, p. 035005, June 2013.

[86] D. Maletić, N. Puač, N. Selaković, S. Lazović, G. Malović, A. orević, and Z. L. Petrović, "Time-resolved optical emission imaging of an atmospheric plasma jet for different electrode positions with a constant electrode gap," *Plasma Sources Science and Technology*, vol. 24, p. 025006, Apr. 2015.

[87] A. Michelmore, D. A. Steele, J. D. Whittle, J. W. Bradley, and R. D. Short, "Nanoscale deposition of chemically functionalised films via plasma polymerisation," *RSC Advances*, vol. 3, no. 33, p. 13540, 2013.

[88] H. Biederman, "Properties of films prepared by RF sputtering PTFE and plasma polymerization in some freons," *Annual Proceedings - Reliability Physics (Symposium)*, vol. 1, pp. 42–45, 1980.

[89] H. Biederman and Y. Osada, "Plasma chemistry of polymers," *Advances in Polymer Science*, vol. 95, pp. 56–109, 1990.

[90] P. Favia, F. Palumbo, and R. D'Agostino, "Immobilization of heparin and highly-sulphated hyaluronic acid onto plasma-treated polyethylene," *Plasmas and Polymers*, vol. 3, no. 2, pp. 77–96, 1998.

[91] H. Yasuda, *Plasma Polymerisation*. Academic Press Inc., 1985.

[92] A. Choukourov, H. Biederman, D. Slavinska, L. Hanley, A. Grinevich, H. Boldyryeva, and A. Mackova, "Mechanistic studies of plasma polymerization of allylamine.," *The journal of physical chemistry. B*, vol. 109, pp. 23086–95, Dec. 2005.

[93] H. Biederman, *Plasma Polymer Films*. Imperial College Press, 2004.

[94] A. Brooks and S. Woollard, "Plasma polymerization: a versatile and attractive process for conformal coating," *Proceedings of the SMT: Surface Mount Technology*, vol. 28, p. 38, Feb. 2012.

[95] I. Topala, N. Dumitrascu, and G. Popa, "Properties of the acrylic acid polymers obtained by atmospheric pressure plasma polymerization," *Nuclear Instruments and Methods in Physics Research Section B: Beam Interactions with Materials and Atoms*, vol. 267, pp. 442–445, Jan. 2009.

[96] M. Zelzer, *Plasma Polymer Gradients, Developing A Tool For The Screening Of Biological Responses To Surfaces*. PhD thesis, University of Nottingham, 2009.

[97] H. Yasuda, "Plasma for Modification of Polymers," *Journal of Macromolecular Science: Part A - Chemistry*, vol. 10, pp. 383–420, Mar. 1976.

[98] N. Inagaki, *Plasma Surface Modification and Plasma Polymerization*. Taylor & Francis, 1996.

[99] F. F. Shi, "Recent advances in polymer thin films prepared by plasma polymerization Synthesis, structural characterization, properties and applications," *Surface and Coatings Technology*, vol. 82, pp. 1–15, July 1996.

[100] J. D. Whittle, R. D. Short, D. A. Steele, J. W. Bradley, P. M. Bryant, F. Jan, H. Biederman, A. A. Serov, A. Choukurov, A. L. Hook, W. A. Ciridon, G. Ceccone, D. Hegemann, E. Körner, and A. Michelmore, "Variability in Plasma Polymerization Processes - An International Round-Robin Study," *Plasma Processes and Polymers*, vol. 10, pp. 767–778, Sept. 2013.

[101] V. Sciarratta, D. Hegemann, M. Mller, U. Vohrer, and C. Oehr, *Upscaling of Plasma Processes for Carboxyl Functionalization*. Wiley, 2005.

[102] L. J. Ward, W. C. E. Schofield, J. P. S. Badyal, a. J. Goodwin, and P. J. Merlin, "Atmospheric Pressure Plasma Deposition of Structurally Well-Defined Polyacrylic Acid Films," *Chemistry of Materials*, vol. 15, pp. 1466–1469, Apr. 2003.

[103] O. Carton, D. Ben Salem, S. Bhatt, J. Pulpytel, and F. Arefi-Khonsari, "Plasma Polymerization of Acrylic Acid by Atmospheric Pressure Nitrogen Plasma Jet for Biomedical Applications," *Plasma Processes and Polymers*, vol. 9, pp. 984–993, Oct. 2012.

[104] C. Amorosi, T. Fouquet, V. Toniazzo, D. Ruch, L. Averous, V. Ball, and M. Michel, "Growth rate, morphology, chemical composition and oligomerization state of plasma polymer films made from acrylic and methacrylic acid under dielectric barrier discharge," *Reactive and Functional Polymers*, vol. 72, pp. 341–348, May 2012.

[105] J.-S. Oh and J. W. Bradley, "Heavy Ion Formation in Plasma Jet Polymerization of Heptylamine at Atmospheric Pressure," *Plasma Processes and Polymers*, vol. 10, pp. 839–842, Aug. 2013.

[106] A. Vogelsang, A. Ohl, R. Foest, K. Schröder, and K.-D. Weltmann, "Deposition of Thin Films from Amino Group Containing Precursors with an Atmospheric Pressure Microplasma Jet," *Plasma Processes and Polymers*, vol. 8, pp. 77–84, Jan. 2011.

[107] E. Finot, S. Roualdes, and M. Kirchner, "Surface investigation of plasma HMDSO membranes post-treated by CF 4/Ar plasma," *Applied Surface Science*, vol. 187, no. 3-4, pp. 326–338, 2002.

[108] W. Lertwimolnun and B. Vergnes, "Influence of compatibilizer and processing conditions on the dispersion of nanoclay in a polypropylene matrix," *Polymer*, vol. 46, pp. 3462–3471, Apr. 2005.

[109] M. Bauer, T. Schwarz-Selinger, H. Kang, and A. V. Keudell, "Control of the plasma chemistry of a pulsed inductively coupled methane plasma," *Plasma Sources Science and Technology*, vol. 14, pp. 543–548, Aug. 2005.

[110] S. A. Voronin, M. Zelzer, C. Fotea, M. R. Alexander, and J. W. Bradley, "Pulsed and continuous wave acrylic acid radio frequency plasma deposits: plasma and surface chemistry," *The Journal of Physical Chemistry. B*, vol. 111, pp. 3419–29, Apr. 2007.

[111] E. Twite-Kabamba, A. Mechraoui, and D. Rodrigue, "Rheological properties of polypropylene/hemp fiber composites," *Polymer Composites*, vol. 30, pp. 1401–1407, Oct. 2009.

[112] A. von Keudell and J. Benedikt, "A Physicist's Perspective on Views on Macroscopic Kinetics of Plasma Polymerisation," *Plasma Processes and Polymers*, vol. 7, pp. 376–379, May 2010.

[113] B. Nisol, A. Batan, F. Dabeux, A. Kakaroglou, I. De Graeve, G. Van Assche, B. Van Mele, H. Terryn, and F. Reniers, "Surface Characterization of Atmospheric Pressure Plasma-Deposited Allyl Methacrylate and Acrylic Acid Based Coatings," *Plasma Processes and Polymers*, vol. 10, pp. 564–571, June 2013.

[114] A. Kakaroglou, B. Nisol, K. Baert, I. De Graeve, F. Reniers, G. Van Assche, and H. Terryn, "Evaluation of the Yasuda parameter for the atmospheric plasma deposition of allyl methacrylate," *RSC Adv.*, vol. 5, no. 35, pp. 27449–27457, 2015.

[115] P. Hamerli, "Surface properties of and cell adhesion onto allylamine-plasma-coated polyethylenterephtalat membranes," *Biomaterials*, vol. 24, pp. 3989–3999, Oct. 2003.

[116] L. Lopez, R. Gristina, G. Ceccone, F. Rossi, P. Favia, and R. D'Agostino, "Immobilization of RGD peptides on stable plasma-deposited acrylic acid coatings for biomedical devices," *Surface and Coatings Technology*, vol. 200, pp. 1000–1004, Oct. 2005.

[117] X. Wang, J. Wang, Z. Yang, Y. Leng, H. Sun, and N. Huang, "Structural characterization and mechanical properties of functionalized pulsed-plasma polymerized allylamine film," *Surface and Coatings Technology*, vol. 204, pp. 3047–3052, June 2010.

[118] A. Fahmy, R. Mix, A. Schönhals, and J. F. Friedrich, "Structure of Plasma-Deposited Poly(acrylic acid) Films," *Plasma Processes and Polymers*, vol. 9, pp. 273–284, Jan. 2011.

[119] M. Golub, T. Wydeven, and A. Johnson, "Similarity of plasma-polymerized tetrafluoroethylene and fluoropolymer films deposited by rf sputtering of poly (tetrafluoroethylene)," *Langmuir*, vol. 7463, no. 25, pp. 2217–2220, 1998.

[120] G. Chen, M. Zhou, Z. Zhang, G. Lv, S. Massey, W. Smith, and M. Tatoulian, "Acrylic Acid Polymer Coatings on Silk Fibers by Room-temperature APGD Plasma Jets," *Plasma Processes and Polymers*, vol. 8, pp. 701–708, Aug. 2011.

[121] S. Candan, A. Beck, L. O'Tool, and R. D. Short, "Effects of processing parameters in plasma deposition: Acrylic acid revisited," *Journal of Vacuum Science & Technology A: Vacuum, Surfaces, and Films*, vol. 16, p. 1702, May 1998.

[122] S. Candan, A. Beck, L. O'Tool, R. Short, and N. J. Braithwaite, "The role of ions in the continuous-wave plasma polymerisation of acrylic acid," *Physical Chemistry Chemical ...*, vol. 1, pp. 3117–3121, 1999.

[123] D. Barton, A. G. Shard, R. D. Short, and J. W. Bradley, "The effect of positive ion energy on plasma polymerization: a comparison between acrylic and propionic acids.," *The Journal of Physical Chemistry. B*, vol. 109, pp. 3207–11, Mar. 2005.

[124] S. A. Voronin, J. W. Bradley, C. Fotea, M. Zelzer, and M. R. Alexander, "Characterization of thin-film deposition in a pulsed acrylic acid polymerizing discharge," *Journal of Vacuum Science & Technology A: Vacuum, Surfaces, and Films*, vol. 25, no. 4, p. 1093, 2007.

[125] S. Voronin, M. Alexander, and J. Bradley, "Time-resolved mass and energy spectral investigation of a pulsed polymerising plasma struck in acrylic acid," *Surface and Coatings Technology*, vol. 201, pp. 768–775, Oct. 2006.

[126] M. Tatoulian, F. Arefi-Khonsari, and J.-P. Borra, "Deposition of Organic Coatings at Atmospheric Pressure from Liquid Precursors," *Plasma Processes and Polymers*, vol. 4, pp. 360–369, May 2007.

[127] J. Wan, S. Wang, M. Song, X. Jia, and J. Yang, "Plasma-Induced Direct-Grafting on Polytetrafluoroethylene Films by Quasi-Glow Discharge at Atmospheric Pressure," *Plasma Processes and Polymers*, vol. 6, pp. 825–830, Nov. 2009.

[128] X. Zheng, G. Chen, Z. Zhang, G. Lv, J. Beem, S. Massey, and M. Tatoulian, "Different Polymerizing Characteristics of Ar/He Atmospheric Pressure Plasma Jets at Room Temperature," *Plasma Processes and Polymers*, vol. 10, pp. 379–387, Apr. 2013.

[129] G. N. Parsons, S. M. George, and M. Knez, "Progress and future directions for atomic layer deposition and ALD-based chemistry," *MRS Bulletin*, vol. 36, no. 11, pp. 865–871, 2011.

[130] R. L. Puurunen, "A Short History of Atomic Layer Deposition: Tuomo Suntola's Atomic Layer Epitaxy," *Chemical Vapor Deposition*, vol. 20, pp. 332–344, Oct. 2014.

[131] T. Suntola and J. Antson, "Method for producing compound thin films," Nov. 15 1977. US Patent 4,058,430.

[132] S. M. George, "Atomic layer deposition: An overview," *Chemical Reviews*, vol. 110, no. 1, pp. 111–131, 2010.

[133] M. Leskela and M. Ritala, "Atomic layer deposition (ALD): from precursors to thin film structures," *Thin Solid Films*, vol. 409, no. 1, pp. 138–146, 2002.

[134] K. E. Elers, T. Blomberg, M. Peussa, B. Aitchison, S. Haukka, and S. Marcus, "Film uniformity in atomic layer deposition," *Chemical Vapor Deposition*, vol. 12, no. 1, pp. 13–24, 2006.

[135] H. Kim, "Characteristics and applications of plasma enhanced-atomic layer deposition," *Thin Solid Films*, vol. 519, pp. 6639–6644, Aug. 2011.

[136] H. Kim, "Atomic layer deposition of metal and nitride thin films: Current research efforts and applications for semiconductor device processing," *Journal of Vacuum Science & Technology B: Microelectronics and Nanometer Structures*, vol. 21, no. 6, p. 2231, 2003.

[137] J. Skarp, "Combination film, in particular for thin film electroluminescent structures," Dec. 4 1984. US Patent 4,486,487.

[138] I. Park, Y. Kim, S. Lee, B. Kim, S. Lee, and C. Park, "Capacitor which comprise a first dielectric layer, an electrically insulating layer on the firsst dielectric layer, and an aluminum oxide buffer layer formed by atomic layer deposition and stabilized by heat treatment," Nov. 7 2000. US Patent 6,144,060.

[139] T. Yamaguchi, S. Masubuchi, K. Iguchi, R. Moriya, and T. Machida, "Tunnel spin injection into graphene using Al2O3 barrier grown by atomic layer deposition on functionalized graphene surface," *Journal of Magnetism and Magnetic Materials*, vol. 324, pp. 849–852, Mar. 2012.

[140] J. Aarik, A. Aidla, T. Uustare, K. Kukli, V. Sammelselg, M. Ritala, and M. Leskela, "Atomic layer deposition of TiO2 thin films from TiI4 and H2O," *Applied Surface Science*, vol. 193, no. 1-4, pp. 277–286, 2002.

[141] D. H. Levy, D. Freeman, S. F. Nelson, P. J. Cowdery-Corvan, and L. M. Irving, "Stable ZnO thin film transistors by fast open air atomic layer deposition," *Applied Physics Letters*, vol. 92, no. 19, 2008.

[142] W. M. M. E. Kessels and M. Putkonen, "Advanced process technologies: Plasma, direct-write, atmospheric pressure, and roll-to-roll ALD," *MRS Bulletin*, vol. 36, no. 11, pp. 907–913, 2011.

[143] B. Inc., "Website of the company beneq." www.beneq.com/wcs-600.html, Dec. 2014.

[144] H. Kim and S. M. Rossnagel, "Plasma-enhanced atomic layer deposition of tantalum thin films: the growth and film properties," *Thin Solid Films*, vol. 441, no. 1-2, pp. 311–316, 2003.

[145] S. M. Rossnagel, A. Sherman, and F. Turner, "Plasma-enhanced atomic layer deposition of Ta and Ti for interconnect diffusion barriers," *Journal of Vacuum Science & Technology B*, vol. 18, no. 4, pp. 2016–2020, 2000.

[146] S. B. S. Heil, P. Kudlacek, E. Langereis, R. Engeln, M. C. M. van de Sanden, and W. M. M. Kessels, "In situ reaction mechanism studies of plasma-assisted atomic layer deposition of Al2O3," *Applied Physics Letters*, vol. 89, no. 13, p. 131505, 2006.

[147] M. de Keijser and C. van Opdorp, "Atomic layer epitaxy of gallium arsenide with the use of atomic hydrogen," *Applied Physics Letters*, vol. 58, no. 11, p. 1187, 1991.

[148] H. B. Profijt, S. E. Potts, M. C. M. van de Sanden, and W. M. M. Kessels, "Plasma-Assisted Atomic Layer Deposition: Basics, Opportunities, and Challenges," *Journal of Vacuum Science & Technology A*, vol. 29, no. 5, 2011.

[149] J. J. Thomson, "XIX. Further experiments on positive rays," *Philosophical Magazine Series 6*, vol. 24, pp. 209–253, Aug. 1912.

[150] F. W. Aston, "LXXIV. A positive ray spectrograph," *Philosophical Magazine Series 6*, vol. 38, pp. 707–714, Dec. 1919.

[151] F. W. Aston, "LIX. The mass-spectra of chemical elements," *Philosophical Magazine Series 6*, vol. 39, pp. 611–625, May 1920.

[152] W. Paul and H. Steinwedel, "Ein neues Massenspektrometer ohne Magnetfeld," *Z. Naturforschg*, vol. 8a, p. 448, 1953.

[153] D. P. Gates, "Bristol university - gas chromatography mass spectrometry (gc/ms)." http://www.bris.ac.uk/nerclsmsf/techniques/gcms.html, Apr. 2015.

[154] M. M. Wolff and W. E. Stephens, "A Pulsed Mass Spectrometer with Time Dispersion," *Review of Scientific Instruments*, vol. 24, no. 8, p. 616, 1953.

[155] D. P. Paul, "Mass spectrometry facility — tof." http://www.chm.bris.ac.uk/ms/tof.xhtml, Apr. 2015.

[156] B. A. Mamyrin, V. I. Karataev, D. V. Shmikk, and V. A. Zagulin, "spectrometer with high resolution," *Sov. Phys. JETP*, vol. 37, no. 1, pp. 45–48, 1973.

[157] G. J. O'Halloran, A. S. D. (U.S.)., L. W. Walker, R. A. Fluegge, J. F. Belts, and W. L. Everett, *Determination of Chemical Species Prevalent in a Plasma Jet*. Technical Documentary Report, Air Force Materials Laboratories, Research and Technology Division, Air Force Systems Command, United States Air Force, 1964.

[158] J. H. J. Dawson and M. Guilhaus, "Orthogonal-acceleration time-of-flight mass spectrometer," *Rapid Communications in Mass Spectrometry*, vol. 3, pp. 155–159, May 1989.

[159] J. Coles and M. Guilhause, "Orthogonal acceleration : a new direction for time-of-flight mass spectrometry : fast, sensitive mass analysis for continuous ion sources," *Trends in Analytical Chemistry*, vol. 12, no. 5, pp. 203–213, 1993.

[160] P. Vacuum, "6.3 quadrupole mass spectrometers (qms)." http://www.pfeiffer-vacuum.com/en/know-how/mass-spectrometers-and-residual-gas-analysis/quadrupole-mass-spectrometers-qms/detectors/, Apr. 2015.

[161] J. Watts and J. Wolstenholme, *An introduction to surface analysis by XPS and AES*. John Wiley and Sons Inc., 2003.

[162] D. Briggs, *Surface Analysis of Polymers by XPS and Static SIMS*. Cambridge University Press, 1998.

[163] C. Yaws and H. L. U. Yang, "To estimate vapor pressure easily," *Hydrocarbon Processing; (USA)*, vol. 68:10, Oct 1989.

[164] J. Benedikt, A. Hecimovic, D. Ellerweg, and A. von Keudell, "Quadrupole mass spectrometry of reactive plasmas," *Journal of Physics D: Applied Physics*, vol. 45, p. 403001, Oct. 2012.

[165] "Ellipsometer model AutoEL IV (Rudolph Research)." `http://i.ebayimg.com/00/s/NjUwWDkwMA==/z/3tEAAOxyj4hTGiNs/$_35.JPG`. Accessed: 2015-08-28.

[166] M. Alexander, P. Wright, and B. Ratner, "Trifluoroethanol Derivatization of Carboxylic Analysis," *Surface and interface analysis*, vol. 24, pp. 217–220, Nov. 1996.

[167] A. Chilkoti, B. D. Ratner, and D. Briggst, "Plasma-Deposited Polymeric Films Prepared from Carbonyl-Containing Volatile Precursors : XPS Chemical Derivatization and Static SIMS Surface Characterization," *Chemistry of Materials*, no. 21, pp. 51–61, 1991.

[168] M. A. Noras, *Non-contact surface charge/voltage measurements Fieldmeter and voltmeter methods*. TREK INC., 11601 Maple Ridge Road, Medina, NY 14103, 2002.

[169] D. B. Haddow, A. J. Beck, R. M. France, S. Fraser, J. D. Whittle, and R. D. Short, "Mass spectral investigation of the plasma phase of a pulsed plasma of acrylic acid," *Journal of Vacuum Science & Technology A: Vacuum, Surfaces, and Films*, vol. 18, no. 6, p. 3008, 2000.

[170] D. Haddow, R. France, and R. Short, "A mass spectrometric and ion energy study of the continuous wave plasma polymerization of acrylic acid," *Langmuir*, no. 12, pp. 5654–5660, 2000.

[171] I. Swindells, S. A. Voronin, C. Fotea, M. R. Alexander, and J. W. Bradley, "Detection of negative molecular ions in acrylic acid plasma: some implications for polymerization mechanisms.," *The journal of physical chemistry. B*, vol. 111, pp. 8720–2, Aug. 2007.

[172] S. A. Al-Bataineh, E. J. Szili, G. Desmet, P. Ruschitzka, P. J. Gruner, C. Priest, N. H. Voelcker, D. A. Steele, R. D. Short, and H. J. Griesser, "Chemical and biomolecule patterning on 2D surfaces using atmospheric pressure microcavity plasma array devices," in *Smart Nano-Micro Materials and Devices, December 5, 2011 - December 7, 2011*, vol. 8204, (Hawthorn, VIC, Australia), SPIE, 2011.

[173] J. Benedikt, D. Ellerweg, S. Schneider, K. Rügner, R. R, H. Kersten, and T. Benter, "Mass spectrometry of positive ions and neutral species in the effluent of an atmospheric pressure plasma with hexamethyldisiloxane and

oxygen," *Journal of Physics D: Applied Physics*, vol. 46, p. 464017, Nov. 2013.

[174] J. Koprio, P. Muralt, G. Rettinghaus, and G. Strasser, "Mass spectrometric detection of low-ppm contaminants in sputter process systems at 102 mbar, using a directly exposed ion source," *Vacuum*, vol. 41, pp. 2106–2108, 1990.

[175] M. Alexander and T. Duc, "The chemistry of deposits formed from acrylic acid plasmas," *Journal of Materials Chemistry*, vol. 8, no. 4, pp. 937–943, 1998.

[176] R. Prat, Y. Koh, Y. Babukutty, M. Kogoma, S. Okazaki, and M. Kodama, "Polymer deposition using atmospheric pressure plasma glow (APG) discharge," *Polymer*, vol. 41, pp. 7355–7360, Sept. 2000.

[177] M. J. Shenton and G. C. Stevens, "Surface modification of polymer surfaces: atmospheric plasma versus vacuum plasma treatments," *Journal of Physics D: Applied Physics*, vol. 2761, no. 18, pp. 2761–2768, 2001.

[178] P. Rossini, P. Colpo, G. Ceccone, K. Jandt, and F. Rossi, "Surfaces engineering of polymeric films for biomedical applications," *Materials Science and Engineering: C*, vol. 23, pp. 353–358, Mar. 2003.

[179] M. R. Alexander, J. D. Whittle, D. Barton, and R. D. Short, "Plasma polymer chemical gradients for evaluation of surface reactivity: epoxide reaction with carboxylic acid surface groups," *Journal of Materials Chemistry*, vol. 14, no. 3, p. 408, 2004.

[180] R. Jafari, M. Tatoulian, W. Morscheidt, and F. Arefi-Khonsari, "Stable plasma polymerized acrylic acid coating deposited on polyethylene (PE) films in a low frequency discharge (70kHz)," *Reactive and Functional Polymers*, vol. 66, pp. 1757–1765, Dec. 2006.

[181] K. Parry, A. Shard, and R. Short, "ARXPS characterisation of plasma polymerised surface chemical gradients," *Surface and Interface Analysis*, pp. 1497–1504, 2006.

[182] R. Morent, N. Geyter, S. Vlierberghe, E. Vanderleyden, P. Dubruel, C. Leys, and E. Schacht, "Deposition of Polyacrylic Acid Films by Means of an Atmospheric Pressure Dielectric Barrier Discharge," *Plasma Chemistry and Plasma Processing*, vol. 29, pp. 103–117, Feb. 2009.

[183] Y. Pan, E. Barrios, and D. Denton, "In situ FTIR investigation of MMA plasmas, plasmapolymerized films, and reaction mechanisms," *Journal of Polymer Science, A*, pp. 587–602, 1998.

[184] H. K. Yasuda, "Some Important Aspects of Plasma Polymerization," *Plasma Processes and Polymers*, vol. 2, pp. 293–304, May 2005.

[185] T. P. Kasih, S.-I. Kuroda, and H. Kubota, "Poly(methyl methacrylate) Films Deposited via Non-Equilibrium Atmospheric Pressure Plasma Polymerization Using Argon as Working Gas," *Plasma Processes and Polymers*, vol. 4, pp. 648–653, Aug. 2007.

[186] R. W. Dreyfus, J. M. Jasinski, R. E. Walkup, and G. S. Selwyn, "Optical diagnostics of low pressure plasmas," *Pure and Applied Chemistry*, vol. 57, no. 9, pp. 1265–1276, 1985.

[187] B. Smith, *Fundamentals of Fourier Transform Infrared Spectroscopy, Second Edition*. CRC Press, 2011.

[188] R. Giordanengo, S. Viel, B. Allard-Breton, A. Thévand, and L. Charles, "Tandem mass spectrometry of poly(methacrylic Acid) oligomers produced by negative mode electrospray ionization.," *Journal of the American Society for Mass Spectrometry*, vol. 20, pp. 25–33, Jan. 2009.

[189] R. Wild, T. Gerling, R. Bussiahn, K.-D. Weltmann, and L. Stollenwerk, "Phase-resolved measurement of electric charge deposited by an atmospheric pressure plasma jet on a dielectric surface," *Journal of Physics D: Applied Physics*, vol. 47, p. 042001, Jan. 2014.

[190] A. Kumada, S. Okabe, and K. Hidaka, "Residual charge distribution of positive surface streamer," *Journal of Physics D: Applied Physics*, vol. 42, p. 095209, May 2009.

[191] N. G. Kubala, P. C. Rowlette, and C. A. Wolden, "Plasma-Enhanced Atomic Layer Deposition of Anatase TiO(2) Using TiCl(4)," *Journal of Physical Chemistry C*, vol. 113, no. 37, pp. 16307–16310, 2009.

[192] R. L. Puurunen, "Surface chemistry of atomic layer deposition: A case study for the trimethylaluminum/water process," *Journal of Applied Physics*, vol. 97, no. 12, p. 121301, 2005.

[193] E. R. Cleveland, L. Henn-Lecordier, and G. W. Rubloff, "Role of surface intermediates in enhanced, uniform growth rates of TiO 2 atomic layer deposition thin films using titanium tetraisopropoxide and ozone," *Journal of Vacuum Science and Technology A: Vacuum, Surfaces and Films*, vol. 30, no. 1, 2012.

[194] V. R. Rai, V. Vandalon, and S. Agarwal, "Influence of surface temperature on the mechanism of atomic layer deposition of aluminum oxide using an oxygen plasma and ozone," *Langmuir*, vol. 28, no. 1, pp. 350–357, 2012.

[195] F. Brand and M. Bilek, "Applied and plasma physics: lecture notes," February 2003.